Thermal Modelling and Thermal Control Optimisation of the mN-μHEMPT

MSc. Thesis

I. Granero Moneva

Technische Universiteit Delft

Delft University of Technology

Challenge the future

Thermal Modelling and Thermal Control Optimisation of the mN-μHEMPT

MSc. Thesis

by

I. Granero Moneva

to obtain the degree of Master of Science
at the Delft University of Technology,
to be defended publicly on Tuesday August 29, 2017 at 9:30 AM.

Student number:	4432118	
Project duration:	February 1, 2017 – August 29, 2017	
Thesis committee:	Dr. A. Cervone,	TU Delft, supervisor
	Ir. B. T. Z. Zandbergen,	TU Delft
	Dr. G. C. H. E. de Croon,	TU Delft

This Master Thesis was performed entirely at Airbus Friedrichshafen, under the supervision of Dr. F. G. Hey.

Acknowledgements

After two years of hard work and unforgettable experiences, living in two different countries and making friends in all of them, I have finally reached the end of my Masters. This thesis is my greatest academic achievement, and I would like to thank everyone on who I have relied during these past seven months.

I would like to express my gratitude to my Airbus supervisors Franz and Max for their daily help during my thesis. They never despaired with my questions and believed in me when the odds were against. I am in debt with Tobias, who taught me from scratch how to use Systema, and who was always available for a doubt-solving meeting.

My special thanks to Angelo, in whom I found a role-model and a counsellor, already since he supervised my Bachelor thesis.

On a personal level, I am deeply grateful to Yeray, who always found time to hear out my problems, to my family, for their unconditional encouragement, and to Sarah, with whom sharing the office has been a pleasure.

Thanking you all,

I. Granero Moneva
Friedrichshafen, July 2017

Abstract

Airbus Friedrichshafen is working on the development of a milliNewton HEMPT (High Efficiency Multistage Plasma Thruster): an electrostatic thruster concept suitable for small satellite propulsion. An engineering model, the mN-µHEMPT, has been built and tested in vacuum, generating thrust levels in the range of 1 to 5 mN. Although the working principle is understood, there is still uncertainty in the loss process, in particular the heat transfer in the plasma-wall interaction. An efficient heat management is crucial for the operation of the thruster, as the performance of the magnets is severely hindered after reaching 250ºC. With this in mind, the present thesis aims to produce the first thermal model of the mN-µHEMPT, with which a detailed thermal analysis can be carried out. The model validation strategy, based on correlation to testing results, makes it possible to overcome the uncertainty regarding the thermal losses. By simulating the operation of the thruster in extreme load cases in a Low Earth Orbit, its thermal performance is assessed, resulting in a detailed understanding of the temperature evolution and heat propagation through the different components. This information is then used to improve the performance by implementing design modifications. The result of the thesis is a thermal model validated to within 1.65ºC as mean deviation, predicting a maximum temperature of 180ºC at the magnet stack during operation. The application of a boron nitride coating to the radiator and the decoupling of the heat losses at the magnet stack and at the anode thanks to a second radiator, results in a maximum temperature of the magnet stack of 85ºC. In conclusion, the thermal performance of the mN-µHEMPT is analysed for the first time, and the design modifications proposed become a successful improvement.

Contents

1

Introduction

A small satellite is in general seen as a spacecraft with a mass lower than 100 kg, and includes the picosatellites (up to 1 kg), nanosatellites (up to 10 kg), the microsatellites (up to 100 kg) and the minisatellites (up to 1000 kg) [1]. The use of small satellites has increased in the last decades, managing to carry out technology demonstration, enable communications, science missions and educational projects [2]. In particular, Earth observation is more and more relying on this type of spacecraft [3]. Miniaturization and mass optimization of the different subsystems has made it possible for small satellites to have a competitive performance with respect to traditional satellites [4]. Furthermore, their reduced cost allows their use in constellations, using several satellites to increase the total performance or to achieve a greater coverage, such as the OneWeb mission, meant to bring data connectivity to the world [5]. This has raised interest in standardisation, which further reduces costs and time of development [6].

Due to the constant increase in performance, the small satellites are facing new technological challenges. NASA identified mobility and propulsion as one of the three most needed technical areas for small satellites, investing accordingly in its development [7]. An onboard propulsion system is necessary for station-keeping, orbit corrections and end-of-life disposal of the satellite. In addition, the sophistication of the optical instruments carried as payload in the small satellites restricts the requirements in thermal stability [8].

In the Earth orbit, the space environment is harsh for the spacecraft. The eclipse cycles make the temperatures of the satellite vary from +100ºC to -130ºC in the outer surface, while the electronics and instruments from the payloads have allowable temperature in the range of -10ºC to +25ºC [9]. The thermal control subsystem of the spacecraft ensures that all components are within their allowable temperature range, and that the extreme temperature changes in the outside panels of the satellite are not propagated into the inner components. Given the low available power on a small satellite, the thermal control is mostly based on passive solutions, such as coatings, radiators and conductive materials, or simple and low-power active control methods, such as heaters [8].

Thrusters represent another source of power consumption and heat that has to be dissipated. The available propulsion options are limited [10], with the thrust required for these applications ranging from micro-Newtons to Newtons, depending on the satellite mass and application, and all the systems have thermal losses, which represent a heat load into the thruster [11].

With the increase of standardisation in the field of small satellites, the plug-and-play approach is taking over, i.e. the use of subsystems or components with clearly defined interfaces and specifications that can be bought commercially-off-the-shelf, ready to use and space-qualified [12–14]. Although the current plug-and-play state-of-the-art is focused on avionics and software rather than on hardware [15], thruster developers are moving towards this trend, putting effort on creating straight-forward interfaces so that the thrusters can be easily integrated in the spacecraft [16]. In this way, isolating the thruster from the spacecraft is crucial, and thermally decoupling them in particular. This means that the propulsion system has to be autonomous and evacuate the heat generated during its operation by itself, without relying on the spacecraft.

Regarding the space propulsion options available, the main three technologies used currently are cold gas generators, chemical thrusters and electric thrusters. The working principle of cold gas generators is to discharge a tank full of pressurised fluid. Chemical propulsion releases the energy stored in the propellant through chemical reactions in order to accelerate the fluid that produces the thrust force [17, 18]. Electric thrusters rely on an external power source to accelerate the fluid by heating it (electrothermal propulsion), through potential differences (electrostatic propulsion) or using the Lorentz force (electromagnetic propulsion) [19]. The main advantage of electric propulsion over the other three is the efficient use of propellant. If the power source is correctly designed, it is possible to reduce the total mass with respect to other propulsion systems, as less propellant is required.

At Airbus in Friedrichshafen, particularly in the Laboratory for Enabling Technologies (LET), an electric thruster is being developed since 2009 [20]. It is a High Efficiency Multi-stage Plasma Thruster (HEMPT) aimed for providing main propulsion in small satellite missions, specifically minisatellites (100 to 1000 kg), with thrust levels in the order of a couple of milli-Newtons [21].

The latest development of this thruster at Airbus is an Engineering Model, named mN-µHEMPT, which has been built and tested successfully [20]. The thruster is a High Efficiency Multistage Plasma Thruster (HEMPT) is an electrostatic thruster concept, patented by Günter Kornfeld, Jürgen Wegener and Harald Seidel from Thales Electronic Devices (TED) in 1998 [22]. The working principle was derived from a Travelling-Wave-Tube (TWT), confining a plasma to the axis of a discharge chamber through magnetic fields and accelerating the ions through several potential difference stages [23]. The development resulted in the thrusters HEMPT 3050 and HEMPT 30250, with thrust levels of 50 mN and 250 mN, respectively [24].

At Airbus, the thruster being developed is intended for lower thrust levels, between 1 and 5 mN [25], with application to smaller spacecraft than the Thales thrusters. The objective is to have a propulsion system as independent as possible from the spacecraft, which is why the thruster is designed to effectively manage its heat generation and losses. However, the thermal losses in the HEMPT are still not well understood, due to the complex plasma-wall interaction taking place inside the discharge chamber [26]. This complicates the design of the thermal control, as the actual losses cannot be computed.

In this way, the objective of this thesis is to contribute to the thermal control design of the mN-µHEMPT by creating a thermal model that effectively avoids the thermal losses uncertainty. This thermal model, the first one of this particular thruster, will allow to understand its thermal performance when operating in orbit. From the results obtained, a design optimization will take place, improving the performance of the thruster.

The impact of this thesis will be twofold. On the one side, it will contribute to the development of the mN-μHEMPT system, performing the first thermal analysis and re-designing the thruster with the obtained results. On the other side, the thermal model will be correlated to testing data, challenging the assumptions done on the thermal losses, which will result in a better knowledge of the values and spatial distribution along the chamber.

In this way, the main motivation of the Thesis will be to:

- Increase the knowledge and understanding on the thermal losses of this thruster concept and its thermal performance. It will be possible to establish effective assumptions regarding the thermal losses and generate the first thermal model of the mN-μHEMPT.
- Characterise and optimise the current thruster design, contributing to its development. It will be the first thermal control system design optimisation: a critical part of the system due to the high thermal sensitivity of the rare earth magnets.

In view of the motives exposed, the research objectives of the Thesis will be:

1. to set up and validate a thermal model with effective assumptions on the thermal losses by correlating its simulation results to experimental hardware thermal testing,
2. to assess the current thermal behaviour of the thruster by simulating its thermal performance under three extreme load cases: hot, nominal and cold,
3. to improve the thermal performance of the thruster by optimising the thermal control system.

In order to address these research objectives, the Thesis will answer three research questions, one for each research objective:

1. Which assumptions on the thermal losses inside the thruster can effectively describe its thermal performance?
    - 1.1. Which physical processes or parameter values regarding the thermal losses are unknown and have to be assumed?
    - 1.2. How does the thermal modelling of the thruster correlate to experimental measurements on the Engineering Model?
2. What is the expected thermal behaviour of the thruster during operation?
    - 2.1. What is the thermal performance when simulating the hot case (thruster on and direct sunlight)?
    - 2.2. What is the thermal performance when simulating the nominal case (thruster on and indirect sunlight)?
    - 2.3. What is the thermal performance when simulating the cold case (thruster off and no direct sunlight)?
3. Which thermal control system design modifications improve the thermal performance of the thruster?
    - 3.1. What are the objectives of the design modifications with respect to the thermal performance?
    - 3.2. Which design modifications effectively address the objectives?
    - 3.3. What is the increase in performance achieved with the design modifications?

2

Fundamentals

The purpose of this chapter is to provide a brief theoretical background of the topics that will be discussed throughout the thesis. The first section defines electric propulsion and its types, as well as derives common thruster parameters that will be needed to estimate the thermal losses inside the thruster. Subsequently, the HEMPT system is presented, together with its thermally-sensitive elements. The developments being done at the Laboratory of Enabling Technologies are introduced. Finally, the theory of thermal modelling is presented, including how the mathematical models are generated and the assumptions that are commmonly used.

2.1. Electric Propulsion

One definition of electric propulsion is *"the acceleration of gases for propulsion by electrical heating and/or by electric and magnetic body forces"* [17]. Technologically, it is different from chemical propulsion, which uses chemical reactions as energy source to produce the acceleration of the fluid, or cold gas propulsion, which is based on the simple release of pressurised gas into the vacuum [18]. Electric propulsion relies on an external power source to produce the thrust instead of releasing the chemical energy stored on the propellant.

The main advantage of electric propulsion is the efficient use of propellant. This characteristic allows a reduction in the total mass of propellant carried on board of the spacecraft. The power source needed for electric thrusters, however, normally has a higher mass than in other propulsion systems and may counteract the effect of carrying less propellant. If correclty designed, a reduction of the total mass to be launched is possible with respect to other systems. Reducing the mass of the spacecraft can significantly decrease the cost of the launch, as the launch is a main contribution to the total mission cost [9]. For this reason, the use of electric propulsion has increased over the last decades, with application to station-keeping and orbit transfer in Earth orbits, and main propulsion for deep-space missions.

The reason for which electric thrusters have an efficient use of propellant is that they deliver higher exhaust velocities than chemical thrusters (from two to three orders of magnitude depending on the weight of the propellant), which increases the achievable Δv, and thus the specific impulse.

Electric propulsion systems can be classified into three different categories, based on the process by which the propellant is accelerated [19]:

- **Electrothermal propulsion:** uses the electric input power to heat up the propellant, which is then expanded on a nozzle. Arcjets and resistojets are common electrothermal thrusters. Their difference lies in the way they increase the temperature of the propellant. The former is based on a high current arc, while the latter makes use of hot resistors. Electrothermal thrusters have been flown extensively, in spacecraft such as all the 95 Iridium or the Lockheed Martin A2100 satellites [27]. However, their performance is limited by their heating capacity (specific impulse is lower than 700 s) [19].
- **Electrostatic propulsion:** ionized particles are accelerated by an electric field via the Coulomb force. Within this category, numerous system concepts have been developed. Examples of electrostatic thrusters are the grided ion thrusters, the electrospray thrusters and the field emission electric propulsion. Counting with flight heritage, in missions such as NSTAR [28], their specific impulse can reach 10,000 s [19].
- **Electromagnetic propulsion:** relies on the Lorentz force generated by an electromagnetic field to accelerate the ionized propellant. The magnetoplasmadynamic thruster, together with the pulsed plasma thruster, are the greatest exponents of this technology. As an example, the latter has already been flown in missions such as EO-1 [29], achieving specific impulses of around 1,000 s [19].

Given the fact that electric propulsion uses energetic charged particles to generate the thrust, the thruster parameters have to be modified with respect to other thrusters, in order to have a more accurate performance analysis. This is done by redefining the parameters so that they depend on measurable variables characteristic from the electric thrusters.[1]

The achievable thrust is the maximum force that can be delivered by the thruster to the spacecraft. Thrust, T, is defined as the temporal change of momentum (in N):

$$T = \frac{d}{dt}\left(m_p v_p\right) = \dot{m}_p v_p \tag{2.1}$$

where $\dot{m}_p$ is the propellant mass flow rate (in kg/s) and v_p is the exit velocity of the propellant (in m/s). On the case of the electrostatic thrusters, the ions achieve much higher speeds than non-ionized particles. It is then possible to assumme that the exit velocity of the propellant, v_p, is actually the exit velocity of the ions, v_i:

$$v_p \approx v_i = \sqrt{\frac{2qV_b}{M}} \tag{2.2}$$

q being the particle charge (in C), V_b is the voltage of the beam (in V) and M is the ion mass (in kg). In the same way, the mass flow rate of propellant is equivalent to the mass flow rate of ions, $\dot{m}_i$:

---

[1] Derivation following reference [19]

$$\dot{m}_p \approx \dot{m}_i = \frac{I_b M}{q} \tag{2.3}$$

where I_b is the current of the beam (in A) and q is the electron charge (in C). Introducing equations 2.2 and 2.3 into equation 2.1, it is possible to rewrite the thrust in terms of the beam characteristics:

$$T = \sqrt{\frac{2M}{e}} \cdot I_b \sqrt{V_b} \tag{2.4}$$

When using Xenon as propellant, the value of the first term of equation 2.4 can already be computed with the values $M_{Xe} = 131.293\,amu$ and $e = 1.602 \cdot 10^{-19}\,C$. In this way, equation 2.5 shows the relationship between thrust, beam current and beam voltage:

$$T = 1.65 \cdot I_b \sqrt{V_b} \qquad mN \tag{2.5}$$

Once the thrust has been derived, it is possible to establish a power balance of the electric thruster. In this way, the power fed into the thruster, P_{in}, has to be equivalent to the power leaving the thruster, P_{out} (all power variables in W):

$$P_{in} = P_{out} = P_b + P_i + P_{exc} + P_{loss} \tag{2.6}$$

where P_b is the power of the beam, P_i is the power used for ionization, P_{exc} is the power used in excitation of the propellant (without reaching ionization) and P_{loss} is the power lost through heating of the thruster. The input power is known, as it is the electric power that is fed into the thruster. It can be computed as:

$$P_{in} = V_a \cdot I_a \tag{2.7}$$

V_a being the voltage at the anode and I_a being the current at the anode. As far as the beam power is concerned, it is defined in terms of thrust and propellant mass flow rate:

$$P_b = \frac{T^2}{2\dot{m}_p} = I_b \cdot V_b \tag{2.8}$$

Lastly, it is possible to estimate the ionization power (considering only the singly charged particles) through the following equation:

$$P_i \approx I_b \cdot IE \tag{2.9}$$

where IE is the ionization energy of the propellant (in W/A). When the energy that enters the Xenon atoms is not sufficient to cause ionization, it provokes excitation. This is another power loss that is normally considered together with the ionization power. In order to do this, instead of using the ionization energy, the discharge loss, L_{dis}, is used. The value of the discharge loss is normally 7.5 times higher than the ionization energy for ideal Xenon thrusters with low mass utilization efficiency (below 90%) [19].

$$P_i + P_{exc} = I_b \cdot L_{dis} = I_b \cdot 7.5 \cdot IE \tag{2.10}$$

By introducing equations 2.5, 2.7, 2.8 and 2.10 into equation 2.6 it is possible to obtain an estimation of the thermal losses (power lost through heat).

$$P_{loss} \approx V_a \cdot I_a - I_b \cdot 7.5 \cdot IE - I_b \cdot V_b \tag{2.11}$$

Equation 2.11 makes it possible to estimate the power losses on an electric propulsion system using Xenon as propellant.

2.2. HEMPT

The High Efficiency Multistage Plasma Thruster (HEMPT) is an electrostatic thruster concept, patented by Günter Kornfeld, Jürgen Wegener and Harald Seidel from Thales Electronic Devices (TED) in 1998 [22]. The working principle was derived from a Travelling-Wave-Tube (TWT), confining a plasma to the axis of a discharge chamber through magnetic fields and accelerating the ions through several potential difference stages [23]. The development resulted in the thrusters HEMPT 3050 and HEMPT 30250, with thrust levels of 50 mN and 250 mN, respectively [24]. The former is expected to be flown onboard the Heinrich Hertz Mission [30]. The reason for the development of this thruster concept is its multiple advantages: high thermal efficiency, no erosion of grids or walls due to plasma confinement and wide operating range in terms of mass flow and voltage [23].

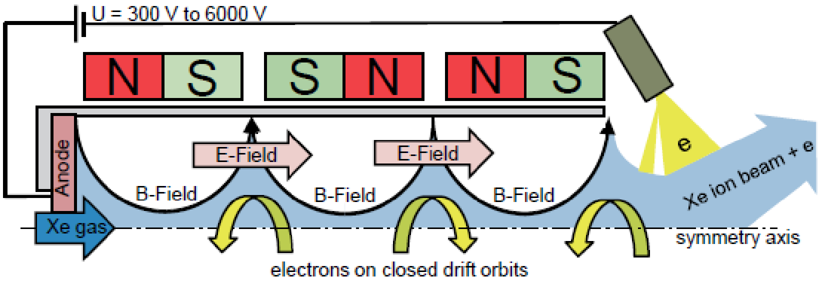

Figure 2.1: Illustration of the HEMPT working principle, showing the magnet stack (top-middle), anode (bottom-left) and neutralizer (top-right), as well as the B-fields and E-fields generated [25].

Figure 2.1 shows the HEMPT concept. It shows a section of the cylindrical discharge chamber. Between the anode and the neutralizer (also referred to as cathode) there is a voltage difference. Electrons flow from the neutralizer (outside the discharge chamber), into the discharge chamber and towards the anode. This flow is stopped by the magnetic field, which is designed in a way that creates magnetic mirrors. This phenomenon confines the electrons in the exit of the chamber and in the locations where the magnetic field drops, called cusp regions. The result is a series of potential differences which are used to accelerate the plasma propellant. This propellant (usually Xenon) enters the chamber through the anode inlet and becomes ionized. It is then accelerated by the potential differences and escapes the chamber generating a thrust force [25].

Even if the general functioning of the thruster is well known, the plasma physics inside the chamber are still not fully understood. Ion and electron tracing simulations have been done with particle-in-cell simulations, but only limited results have been obtained [17, 31]. One of the remaining uncertainties is the process that results in thermal losses. For the HEMPT 3050, the distribution and values of the thermal losses were computed experimentally, by measuring the temperature of the thruster during operation on several locations and correlating it to the temperatures obtained with the thruster off but with heater elements. Combining it all in a thermal model, it was observed that the thermal losses were 15% of the input power, and the heat loss took place in the anode and the cusp regions [24]. Figure 2.2 shows the estimated heat losses for an input power of 1800 W.

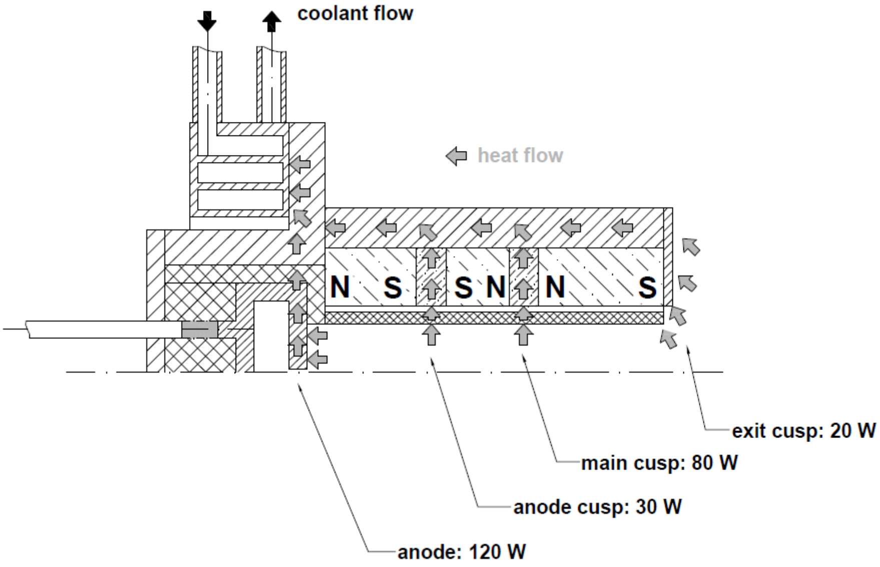

Figure 2.2: Thermal losses distribution in the HEMPT3050 [24]

At Airbus, in the Laboratory for Enabling Technologies (LET), a feasibility study for a down-scaled HEMPT was carried out in 2009 [21]. Since then, the LET is developing a µHEMPT, which would have application in small satellite missions [32]. The current status is an Engineering Model (mN-µHEMPT), which has been tested in a vacuum chamber at Airbus, equipped with a micro-Newton thrust balance and plasma diagnostics set-up [20, 25]. Figure 2.3 shows the expected locations of the thermal losses in the thruster on a sketch of the thruster geometry, where the anode, magnet stack (dummy model) and neutraliser can be identified. The locations of the thermal losses are: A (downstream cusp), B (middle-downstream cusp), C (middle-upstream cusp) and D (anode).

The only thermal analysis that has been carried out on the mN-µHEMPT consisted in dividing the thruster into three thermal nodes: anode, magnet stack and radiator. By solving the heat network equations iteratively, it was possible to find the transitory solution of the three temperatures. The result obtained was that after 45 minutes the magnets reached their maximum allowable temperature of 200°C, meaning that continuous operation of the thruster is not possible with that design [20]. This result was obtained under the assumption of 70 W of

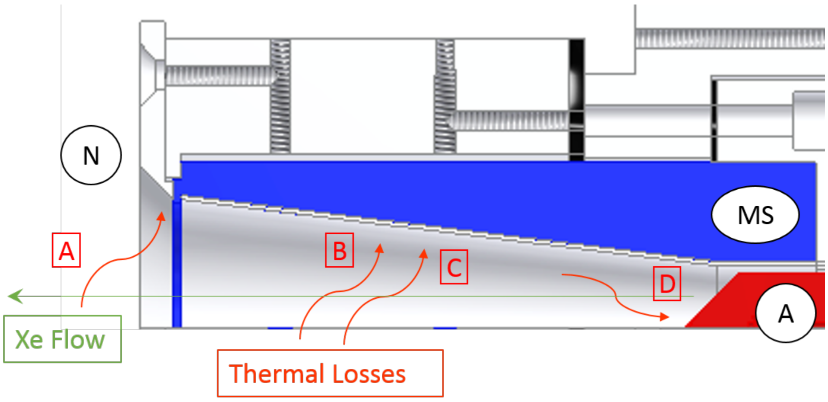

Figure 2.3: Thermal losses in the mN-μHEMPT (locations A, B, C and D). The magnet stack (MS), anode (A) and neutraliser (N) are also visible, as well as the discharge flow direction.

thermal losses from a 100 W input power. The conclusion obtained from the simulation was that a thermal design and optimisation is needed for the mN-μHEMPT to be operated, but assuming 70% losses is not accurate, as it will be shown during the thesis.

As a summary, there is currently no analytical way of computing the heat load coming from the plasma into the thruster wall and anode. Thermal losses can be estimated with the help of assumptions for the beam properties and the power balance (equation 2.8), but accurate values have only been achieved experimentally. Even though thermal models have been developed for the HEMPT 3050, the detailed explanation of such models as well as the assumptions used have not been published. Moreover, all the knowledge obtained from the TED developments can be used as a baseline for the mN-μHEMPT, but the significant difference in thrust level may impact the thermal design in unexpected ways.

2.3. Thermal Modelling

The thermal behaviour of any system operating in space is of critical importance, due to the extreme temperatures reached. In the case of an Earth orbit, the thin atmosphere does not protect the spacecraft from the radiation, as it does on the surface. Direct sunlight raises the temperature of the satellite, and on the eclipse all surfaces radiate the heat out into space, which is at a background temperature of 3 Kelvin. This results in abrupt changes in the temperature of the spacecraft outer surface, shifting from +100ºC to -130ºC in a matter of hours [9]. This temperature changes can be extensively reduced with well-thought thermal control, so that the interior of the satellite stays within the desired temperature ranges.

Each component of the spacecraft has a requirement on the range of temperature in which it can perform its function correctly. The purpose of thermal control is to design the spacecraft in a way that meets all thermal-related requirements. How to verify the thermal design of a component or system is, however, a complicated task, given the complexity of reproducing the space environment in a testing facility. Even if vacuum chambers and solar simulators exist [33], their use is expensive and time-consuming. Thermal modelling is a solution to this. By creating a mathematical model of the spacecraft, it is possible to simulate the space environment and analyse the thermal behaviour of the components as if they were in orbit. This results in an approximation to the real thermal response of each element that allows to verify whether its design meets the thermal requirements or not.

A thermal model for a spacecraft system/subsystem/component is in general divided into two parts: Geometrical Mathematical Model (GMM) and Thermal Mathematical Model (TMM). The GMM is a representation of the geometry of the system to be modelled, while the TMM is the set of characteristics that define a closed thermal problem and allow to formulate the energy balance equation [34].

As far as the modelling approach is concerned, there are two methods that are extensively used [35]. Both are based on the same idea of geometry discretization, transforming the continuous medium into a finite number of elements. In this way, it is possible to solve the heat balance equation on each element, approximating the real solution by an iteratively-obtained one. The two main approaches are i) finite elements and ii) lumped parameters [36].

On the one hand, finite element analysis is a common modelling technique in disciplines such as structural analysis, and provides an approximate solution to boundary problems in systems of partial differential equations. Its use by thermal engineers has increased lately [37]. Computationally intensive, it can however make use of symmetries to reduce the size of the model. It can achieve accurate results, but it requires in-depth knowledge of the material properties of the different components of the model.

On the other hand, the lumped parameters method considers each node as an isothermal element, meaning that the temperature is uniform throughout the node. This temperature changes in relation to its heat capacity and the heat flux coming in and out of the node, as it can be seen in equation 2.12, which shows the heat balance equation applied to a node i:

$$C_i \frac{dT_i}{dt} = \dot{Q}_{Dis,i} + \dot{Q}_{Sun,i} + \dot{Q}_{IR,i} + \dot{Q}_{Alb,i} + \sum_{j=1}^{n} GL_{ij}(T_i - T_j) + \sum_{j=0}^{n} GR_{ij}\sigma(T_i^4 - T_j^4) \tag{2.12}$$

where C_i is the heat capacity of the node (in J/K), T_i is the temperature of the node (in K), $\dot{Q}_{Dis,i}$ is the internal heat flux dissipated at node i (in W), and σ is the Stefan-Boltzmann constant (in W/m^2/K^4). $\dot{Q}_{Sun,i}$, $\dot{Q}_{IR,i}$ and $\dot{Q}_{Alb,i}$ are the heat fluxes in the node i due to the Sun, Earth infrared and albedo radiations (in W), respectively. These values only considered the heat flux absorbed by the node (part of the heat is reflected and part transmitted). GL_{ij} and GR_{ij} are the conductive and radiative couplings between the nodes i and j (in W/K and m^2, respectively). The summation terms run through all the nodes of the model (1 to n), and the radiative couplings also include the node 0, indicating outer space.

The conductive couplings depend on the thermal conductivity of the material, the distance between nodes and the area of the node perpendicular to the heat transfer direction. The radiative couplings depend on the emissivities and radiating areas of the nodes involved, as well as their respective view factors. In spacecraft thermal control, heat transfer normally takes place through the mechanisms of conduction and radiation, which is why equation 2.12 does not consider convection in the first instance. However, this heat transfer method should be taken into account if necessary [34].

In a model with n nodes, the equation 2.12 of heat balance is formulated for each node, which results in a system of n differential equations. This system of equations is solved via numerical integration, creating a time discretization (i.e. dividing the continuous time into a set of time steps) that allows to calculate the temperatures of each node at each time step. The temperature of every node at each time step is known as the transient solution. When the system achieves a thermal equilibrium, meaning that the temperatures of the nodes do not vary with time, it is known as steady-state.

The steady-state solution of the system of differential equations is easier to obtain, as it corresponds to solving the equation 2.12 when the left side is equal to zero. This is due to the fact that on the steady-state, the temperatures of the nodes do not depend on the time anymore, and the derivative is zero.

Given the lower computational effort of obtaining the steady state solution, as well as the fact that it represents the limit temperature achieved, it is common practice in thermal engineering to use this result to size the thermal control systems. The reason behind this is that the component will not reach a higher temperature than the steady-state when receiving heat (or a lower temperature when emitting heat). Therefore, the steady-state is a worst case scenario that may not be achieved during operation, as the thermal conditions in orbit are constantly changing.

Thermal requirements on the spacecraft components, however, may constrain not only the temperature itself, but also the temperature gradients and thermal stability. Moreover, it is possible that the high heat capacities make it impossible to achieve a steady-state during operation. For these reasons, the transient solution is also computed and used during the design of the thermal control system.

A summary of the process followed in order to define a thermal model is:

1. Set up the Geometrical Mathematical Model with all the radiative surfaces
2. Discretize the GMM into nodes, assigning the corresponding optical properties to each one
3. Compute both the external thermal loads on the model (due to the Sun radiation, Albedo, Earth infrared, etc.) and the internal radiative couplings (between the different model surfaces as well as with space)
4. Define the conductive couplings, heat capacities and temperature boundary conditions in order to have a complete TMM
5. Solve the system of differential equations to obtain the transient and steady-state solutions

In order to be able to use a thermal model, it has to be validated. Model validation is usually done through correlation to testing results [38–41]. During the test, the temperature is measured at different locations. The test conditions are simulated, and if the model manages to reproduce the results of the testing with sufficient accuracy, then the model is validated.

3

Thermal Model

The purpose of this chapter is to present the thermal model of the mN-µHEMPT. Firstly, the latest thruster design developed at the LET of Airbus is discussed (Engineering Model), introducing the characteristics of the system, as well as the thermal control requirements. From these, it will follow that a thermal model is necessary for the validation of the requirements. Once the need for a thermal model has been justified, a set of objectives is defined, and shall be achieved with the help of the model. These objectives concern the thruster design, mainly in terms of thermal performance. Afterwards, the thermal model of the thruster is explained and the validation of the thermal model via correlation to test data is presented. On a final point, the results of simulating the thruster operation in orbit are discussed, drawing a set of conclusions regarding the thermal performance that will call for design modifications, to be exposed on the following chapter.

3.1. Current Status: Engineering Model

The Engineering Model is made up by three functional parts: the magnet stack, the anode and the housing. The magnet stack (MS) is formed by a series of magnet rings separated from each other by ferro-magnetic and conductive rings called poleshoes. The anode (A) holds the propellant inlet, and is located at the upstream side the discharge chamber. Housing comprises the other components that do not have a direct influence on the thruster performance. The purpose of the housing is twofold: structural and thermal. From a structural point of view, the different components of the housing fix the position of the magnet stack and the anode, and create an interface between the thruster and the rest of the propulsion system. From a thermal point of view, the housing is designed to evacuate the heat generated during thruster operation. The heat is transported via conduction to the outer surfaces of the thruster, which then release it out of the system via radiation.

During the design of the Engineering Model, the thermal aspect was taken into account for the first time. This was a driver for the design, based on assumptions regarding the heat

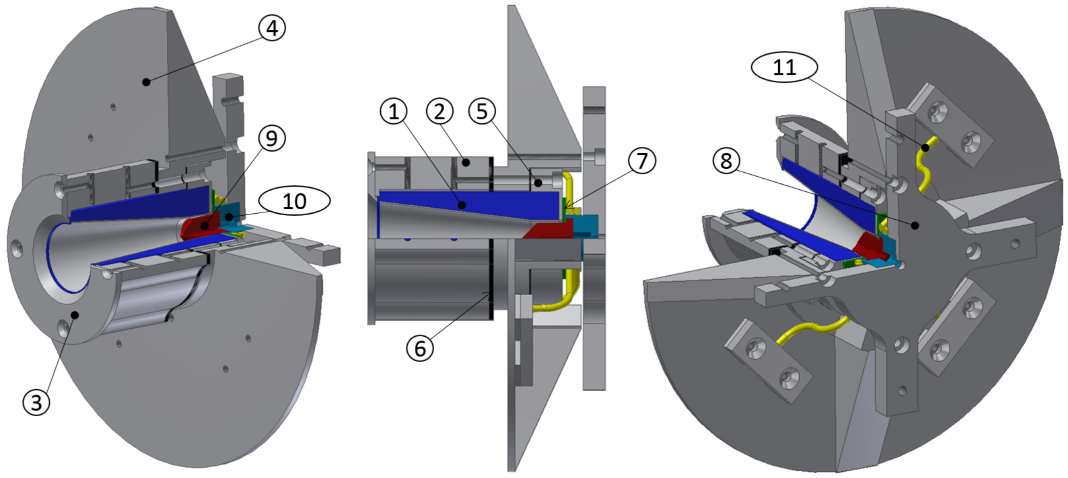

Figure 3.1: Front, side and back views of the mN-µHEMPT Engineering Model with quarter cut-out. Blue: magnet stack (dummy), yellow: heat pipes, red: anode, cyan: anode holder, grey: housing. For the part numbering, refer to table 3.1.

losses inside the discharge chamber and the heat flow through the thruster components. The assumption was that the heat losses occurred at the anode and at the poleshoes, mostly on the middle ones [24]. As it can be seen in figure 3.1, the Engineering Model intends to connect all heat losses to a circular radiator of 20 cm diameter. On the one hand, the poleshoes and magnets lead the heat through conduction to the front housing and into the radiator. On the other hand, the anode is connected to the anode holder, and thermally isolated from the magnet stack thanks to the macor ring. Then the heat flows through heat pipes connecting the anode holder to the radiator. A comprehensive part list can be found in table 3.1.

Table 3.1: Part list of the mN-µHEMPT Engineering Model, following numbering on figure 3.1.

Part nº	Part Name	Material	Envelope [mm]
1	Magnet Stack - MS	Sm2Co17 (Magnets - MG) Steel St37 (Poleshoes - PS)	R20x75
2	Front Housing - H	Aluminium 7075	R30x48
3	Front Radiator - FR	Aluminium 7075	R37x3
4	Radiator - R	Aluminium 7075	R100x37.5
5	Magnet Press - MP	Aluminium 7075	R30x13.5
6	Spacer - S	Sigraflex	R30x0.8
7	Macor Ring - MR	Macor	R17.5x1.5
8	Mount - M	Aluminium 7075	57x57x9.5
9	Anode - A	Brass	R8.5x22
10	Anode Holder - AH	Boron Nitride	R10x30
11	Heat Pipes - HP	Copper	R1.5x10

Even if the design has the heat dissipation in mind, no in-depth thermal analysis of the thruster was performed. The design was tuned experimentally, achieving a configuration that did not overheat during testing. Hence, the thermal performance of the Engineering Model is only known in the testing environment. This is an issue, as there is no information on how the thruster would perform in space. Moreover, the temperature is measured at only 5 different locations on the thruster. Five measurement points is not sufficient to determine the value and location of the maximum temperatures reached, and none of the measurements are at the anode or at the discharge chamber, which are the expected hottest locations. Conclusively, two problems of the Engineering Model have been identified:

A - The highest temperatures achieved by the thruster are unknown.

B - The thermal performance of the thruster outside the testing environment is unknown.

3.2. Requirements and Load Cases

The impact on the design of the two problems identified in the previous section is clear when analyzing the thermal requirements. Requirements always refer to the maximum/minimum achieved temperatures, but as problem A showed these temperatures are not known. Furthermore, the load cases defined for the thruster consider the operation of the thruster in orbit. As problem B states, it is not possible to obtain information about the performance of the thruster in orbit with the available models.

The load cases represent scenarios that the thruster may encounter during operation. Each of these situations is defined by: the orbit followed by the spacecraft, its attitude and the location of the thruster on the spacecraft. At this point of the design, the mission characteristics for the thruster have not yet been defined. With this uncertainty, it is necessary to consider the possible missions and obtain the load cases from them. The only constraint imposed is that the thruster shall fly in a LEO (Low Earth Orbit), as the objective is to use the mN-μHEMPT as main propulsion system for small satellite missions, mostly found in these Earth orbtis [42].

With this information, three load cases are defined: hot case, cold case and nominal case. The hot case represents the scenario in which the thruster reaches the highest temperatures. Similarly, the thruster reaches the coldest temperatures during the cold case. Finally, a nominal case is defined as a mid-point situation between the hot and cold cases, which will describe the normal operation of the thruster.

In order to determine the hot and cold cases, different missions were considered, taking into account the orbit and the attitude of the thruster. Figure 3.2 shows the Design Option Trees defined to determine the extreme cases. As far as the orbit is concerned, only Sun Synchronous (SS) and circular orbits were considered, given their popularity amongst LEO satellites and constellations [43]. The difference between these orbits lies in the eclipse time. The extreme cases (maximum eclipse and no eclipse) are given by the SS 12:00h and SS 6:00h, respectively.

The remaining parameter that defines the Earth orbit is altitude, and even if LEO extends up to 2000 km, most of the satellites fly in the 400-1200 km range [44]. The effect of altitude on the thruster temperature is linked to the Albedo and Earth IR radiation: the closer to Earth, the higher the heat flux into the thruster.

The attitude is provided with respect to the pointing direction of the ion beam centre axis. Different cases, such as continuous Sun pointing, velocity pointing or Nadir pointing were considered. Pointing is crucial for the radiating surfaces. When pointed towards the Sun or the Earth, their performance decreases, as they radiate heat out at a lower rate and also receive higher heat flux from these celestial bodies.

Bearing this in mind, and based on the effect of changing each parameter of the mission, the hottest and coldest cases are assumed, considering the most extreme values for each parameter. Furthermore, it is clear that the hottest case requires the thruster to be switched

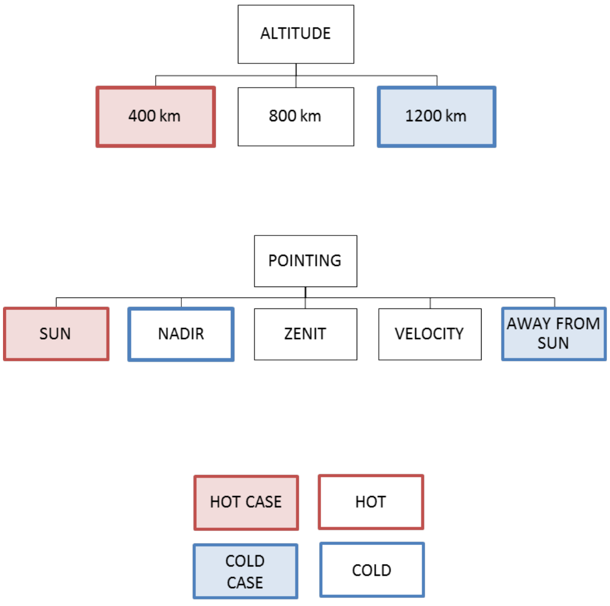

Figure 3.2: Design Option Trees for the hot and cold case selection

on, while the coldest case will be achieved with the thruster turned off. Table 3.2 summarizes the characteristics of each case, including also a nominal case with mid-point values for all mission parameters.

Table 3.2: Description of load cases

Case	Orbit	Altitude	Pointing Direction	Thruster
Hot	SS 6:00h	400 km	Sun	On
Nominal	Circular 60°	800 km	Velocity	On
Cold	SS 12:00h	1200 km	Away from Sun	Off

Apart from the load cases, a complete set of thermal requirements for the mN-μHEMPT was elaborated. Requirements are classified with respect to their content, and numbered accordingly, as it can be seen in table 3.3. All identifiers use the acronyms THR for thruster and TC for thermal control. The requirements have been defined following the Thermal Control General Requirements ECSS-E-ST-31C [45]. All requirements are shown in this section with their corresponding rationales. Furthermore, a complete list can be found in appendix F.

Table 3.3: Requirement numbering

ID	Classification
THR-TC-1XX	Mission requirements
THR-TC-2XX	Performance requirements
THR-TC-3XX	Design requirements
THR-TC-4XX	Material requirements
THR-TC-5XX	Interface requirements
THR-TC-6XX	Assembly, integration and testing requirements
THR-TC-7XX	Analysis and validation requirements

Table 3.4: Mission requirements

ID	**Requirement**
THR-TC-100	The thermal control of the mN-μHEMPT shall enable the nominal operation of the thruster during all mission scenarios in LEO.
THR-TC-101	The thermal control of the mN-μHEMPT shall enable the nominal operation of the thruster on a 400km 06:00h sun-syncrhonous orbit with the thruster always pointing the Sun (hottest mission scenario).
Rationale	*The hottest mission scenario defines the maximum temperature reached by the thruster during operation.*
THR-TC-102	The thermal control of the mN-μHEMPT shall enable the nominal operation of the thruster on a 1200km 12:00h sun-syncrhonous orbit with the thruster always pointing away from the Sun (coldest mission scenario).
Rationale	*The coldest mission scenario defines the minimum temperature reached by the thruster during operation.*

Mission requirements (THR-TC-100 to THR-TC-102) restrict to LEO the missions applicable to the thruster. Moreover, they introduce the hot and cold cases in a formal way. It is important to include the extreme cases in the requirements to ensure that the thruster is designed taking them into consideration.

Table 3.5: Performance requirements

ID	**Requirement**
THR-TC-200	The maximum temperature reached by each component of the thruster shall remain inside the allowable temperature range.
Rationale	*The allowable temperature is calculated as the maximum and minimum temperatures allowed by the material times a safety factor. These can be found in table 3.6.*
THR-TC-201	The thermal control of the mN-μHEMPT shall be able to dissipate at least 35 W of thermal losses generated by the thruster operation in hot case without exceeding the allowable temperatures of the components.
Rationale	*Value initially calculated analytically as the expected thermal losses for operation at 100 W input power, then updated with model results as double of the thermal losses.*

The performance requirement THR-TC-200 ensures that the maximum temperature of each component is not reached. The allowable temperature is calculated applying a safety margin of around 20%. The most restrictive one is for the Sm2Co17 magnets, which are close to the heat source and have a low allowable temperature (200ºC). Requirement THR-TC-201 establishes a minimum heat dissipation for the thermal control. For a given input power, a percentage of it is lost through heating of the thruster. However, and as it was mentioned in chapter 2, the actual percentage of heat losses is not well known.

Table 3.6: Allowable temperatures for all thruster materials. When ”no data” is indicated, no reference was found for the maximum or minimum temperature.

Material	Ref.	Max./Min. Temp. [°C]	Allowable Temp. [°C]
Sm2Co17	[46]	+250 / -273	+200 / -200
Al 7075	[47]	+477 / no data	+400 / no data
Steel St37	[48]	+300 / no data	+250 / no data
Macor	[49]	+800 / no data	+700 / no data
Boron Nitride	[50]	+1400 / no data	+1200 / no data
Sigraflex	[51]	+3000 / no data	+2600 / no data
Copper	[52]	+260 / no data	+200 / no data
Brass	[53]	+900 / no data	+750 / no data

Table 3.7: Design requirements

ID	Requirement
THR-TC-300	The mass of the thermal control hardware shall be less than 1.55 kg.
Rationale	*The value is the current mass of the Engineering Model. On a later stage of the development, this value should be reconsidered. The mass does not consider the contribution of the Mount (part 8), as it is a MGSE (Mechanical Ground Support Equipment).*
THR-TC-301	The envelope of the thermal control hardware shall be smaller than R0.1x0.865 m.
Rationale	*The value is the current volume envelope of the Engineering Model. On a later stage of the development, this value should be reconsidered. The envelope does not consider the Mount (part 8), as it is a MGSE (Mechanical Ground Support Equipment).*

In space applications, mass is always optimized, but at this point of the development, the mass is not yet a crucial parameter. Consequently, requirement THR-TC-300 establishes the current mass of the Engineering Model as the limit. This requirement will have to be revised in a later stage of the thruster development, ensuring that the resulting propulsion system has an allowable mass. The same reasoning has been applied to the envelope of the thruster.

The design approach taken with the mN-μHEMPT is to ultimately create a stand-alone system that can be used in small satellite missions in a “plug-and-play” manner. This means that the thruster must have a well-defined interface with the rest of the s/c. From the thermal point of view, the thruster shall dissipate its own heat, and be thermally isolated from the spacecraft. Requirements THR-TC-500 and THR-TC-501 define the maximum allowable heat transfer at the interface with the spacecraft. Similarly, the performance of the thruster must not be affected by the thermal control techniques, as described in THR-TC-503.

In the light of requirements THR-TC-100, 101, 102 and 200, the need of a thermal model becomes clear. The reason for this is that the aforementioned requirements cannot be verified via testing in the Airbus premises. The Laboratory of Enabling Technologies counts with a vacuum chamber, and it is possible to perform thermal testing with temperature sensors, but this is not sufficient to recreate the performance of the thruster in orbit. Table 3.11 further describes the reasons, which can be linked to the problems A and B previously identified.

Table 3.8: Material requirements

ID	Requirement
THR-TC-400	All materials used for the thermal control of the thruster shall be suitable for space applications.
Rationale	*Follows from the Space Product Assurance standard ECSS-Q-ST-70-71C [54]*
THR-TC-401	The thermal performance of the system shall be ensured after material degradation at End Of Life (EOL) properties.
Rationale	*Follows from Thermal Control General Requirements ECSS-E-ST-31C [45]*

Table 3.9: Interface requirements

ID	Requirement
THR-TC-500	The thermal control of the thruster shall allow a maximum heat flow of 1 W into the other s/c subsystems through conduction.
Rationale	*The value is an assumption that will be reassessed at a later stage.*
THR-TC-501	The thermal control of the thruster shall allow a maximum heat flow of 1 W into the other s/c subsystems through radiation.
Rationale	*The value is an assumption that will be reassessed at a later stage.*
THR-TC-502	The thermal control of the thruster shall not interfere with the performance of the propulsion system.
Rationale	*This includes the magnetic field generation, plasma acceleration and plume.*

Table 3.10: Assembly, integration and testing requirements

ID	Requirement
THR-TC-600	The thermal control hardware shall be possible to assemble onto the thruster and the rest of the propulsion system.
THR-TC-610	The thermal testing of the thruster shall be done in a vacuum environment in the 10^{-6} mbar regime.
Rationale	*Follows from reference [25]*
THR-TC-611	The thermal testing of the thruster shall be done in a controlled environment of less than +/-3K variation.
Rationale	*Follows from ECSS-Q-ST-70-01C [55]*

Table 3.11: Requirements that cannot be verified through testing of the Engineering Model

Requirement	Comment	Problem
THR-TC-100	Not possible to simulate the Sun, Albedo and Earth IR radiation.	B
THR-TC-101	Not possible to simulate the Sun, Albedo and Earth IR radiation.	B
THR-TC-102	Not possible to simulate the Sun, Albedo and Earth IR radiation.	B
THR-TC-200	No physical space to attach sufficient temperature sensors so as to measure max. and min. temperatures with enough certainty.	A

A thermal model of the thruster would solve this issue, and create a way for verifying the requirements from table 3.11. Firstly, it is possible to accurately simulate the space environment with a thermal model, reproducing the orbit and attitude of the spacecraft and calculating the heat fluxes incoming from the celestial bodies. Secondly, the thermal model is able to compute the temperatures of the thruster components in all locations. By creating a mesh of nodes as fine as necessary, it is possible to assure with enough confidence the location of maximum and minimum temperatures. Finally, the major advantage of setting up a thermal model is its cost-benefit ratio with respect to tests: in addition to being cheaper than testing, it also enables the fast modification of the design.

Table 3.12: Analysis and validation requirements

ID	Requirement
THR-TC-700	The thermal performance of the thruster shall be assessed by thermal analysis only when representative testing is not possible.
THR-TC-701	The thermal analysis shall be performed on space-verified software.
Rationale	*An example of such software is Systema Thermica.*
THR-TC-702	The thermal analysis shall be carried out on a representative thermal model (GMM and TMM) of the thruster.
Rationale	*Following the Thermal Analysis Handbook ECSS-E-HB-31-03A [37].*
THR-TC-710	The model used for thermal analysis shall be validated via testing.
THR-TC-711	The thermal model shall be correlated to testing with a maximum deviation of less than 3°C on the temperatures at the reference points.
Rationale	*The deviation is the absolute difference between the temperature measured in the test and the temperature calculated by the model.*
THR-TC-712	The thermal model shall be correlated to testing with a mean deviation of less than 2.5°C on the temperatures at the reference points.
Rationale	*The mean deviation is the mean value of all deviations in absolute value.*
THR-TC-713	The thermal model shall be correlated to testing with a standard deviation of less than 3°C on the temperatures at the reference points.
Rationale	*The standard deviation is the square root of the sum of the square of the deviations for all data points divided by the number of data points.*

The decision is thus to create a thermal model of the mN-μHEMPT thruster, in order to perform an in-depth thermal analysis of the thruster, as well as assess the performance of the Engineering Model design in orbit. Consequently, a set of requirements for analysis and model validation are elaborated (table 3.12).

At this point, the problems encountered with the Engineering Model, and which did not allow the verification of all thermal control requirements, can be solved by defining a thermal model of the thruster. However, the use of the model is not limited to requirement verification. It can also support the design of the thruster: the conclusions obtained from the thermal analysis may be used to propose design modifications that improve the thermal performance. In order to define the purpose of the thermal model, a set of objectives has been defined:

1. Obtain the temperature distribution of the thruster under the load cases.
2. Demonstrate thermal feasibility of in-orbit thruster operation.
3. Reduce the temperature of the magnet stack during operation with design modifications.

The two first objectives are met by simulating a validated thermal model of the thruster. The third objective calls for a design iteration. Mass reduction and volume envelope reduction are not considered as objectives at this point, given the fact that no structural analysis is considered. The solution is to consider mass and volume envelope as restrictions, so that design modifications do not increase the size of the thruster with respect to the Engineering Model. This has already been considered in the design requirements for the thermal control. Similarly, the simplicity of the design will be considered at all points, but not prioritized over the three main objectives.

3.3. Thermal Model of the Thruster

As it was shown in chapter 2, a thermal model is a mathematical representation of a system that solves the heat balance equation in order to calculate the temperatures of the parts. It consists of a GMM and a TMM, which are defined with a thermal analysis software. In the case of the mN-μHEMPT thermal model, the tool used is Systema Thermica, available at Airbus, and is up to space standards [37].

Geometrical Mathematical Model

To begin with, the geometry of the thruster is defined. This geometry is then used for calculating the radiative couplings, both external and internal. Hence, only the radiating surfaces of the thruster have to be included in the model. All the geometries are modelled as simple shapes (cylinders, rectangles, circles, triangles, cones, discs...) so that Systema can easily compute the view factors for the radiative couplings.

As it can be seen in figures 3.3 and 3.4, the thermal model for in-orbit simulation of the thruster considers the Engineering Model as well as a spacecraft panel, on which the thruster would be mounted. The dimensions of the thruster were measured directly from the Engineering Model, and the s/c panel wall is a 30x30 cm rectangle. The choice of these dimensions is motivated by the fact that this wall size covers completely the thruster in the cold load case, blocking all Sun radiation. As there is no selected spacecraft for this thruster, as well as no defined location and orientation, the worst case scenarios have to be considered. In this case,

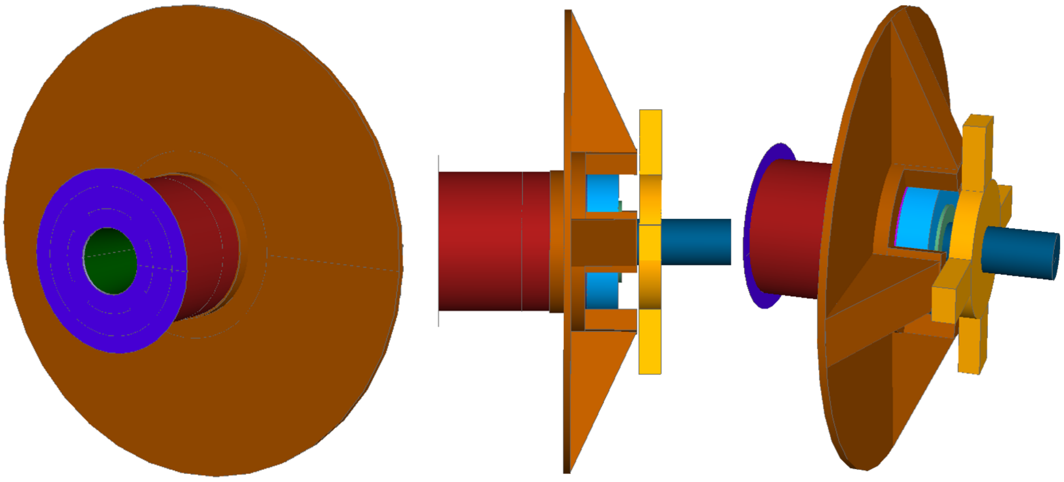

Figure 3.3: Front, side and back views of the mN-μHEMPT Thermal Model. The visible components are the radiator (orange), the front housing (red), the front radiator (purple), the mount (yellow), the magnet press (light blue) and the anode holder (dark blue). The exit of the discharge chamber is always shown on the left.

the 30x30 cm rectangle is sufficient to reach the coldest temperatures. The spacecraft panel is assumed to be covered by MLI (Multi-Layer Insulation).

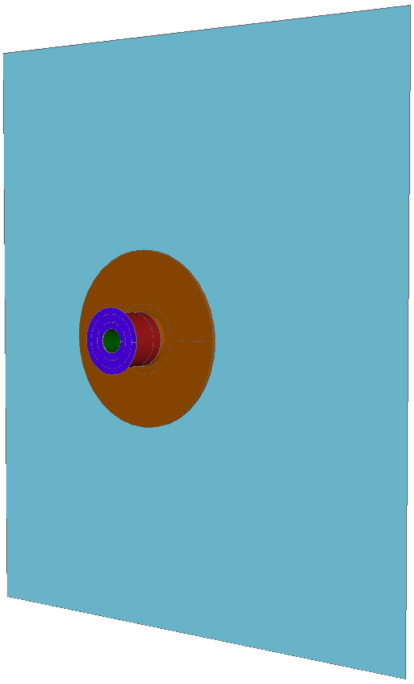

Figure 3.4: Thermal Model for in-orbit simulation (thruster + s/c panel). It is not necessary to model other sides of the spacecraft because the thruster only has radiative heat exchange with the shown panel.

Each surface is assigned optical properties: absorptivity (α) and emissivity (ε). A list of the materials used can be found in table 3.13.

The last step for finishing the GMM is to create the spatial discretization. This is done by meshing each surface (i.e. dividing it into nodes). The mesh must be fine enough to capture the temperature changes between different parts of an element. As a rule of thumb, the temperature change between two adjacent nodes from a same element should not be

Table 3.13: Optical properties used on the Thermal Model. (*) Absorptivities selected based on color of the material.

Material	Part	Emissivity		Absorptivity	
Aluminium 7075	H, FR, R (back), MP, M	0.1	[56]	0.14	[57]
Brass	A	0.2	[56]	0.4	[58]
Boron Nitride	AH, MS (in)	0.9	[59]	0.1	[60]
Black Kapton	R (front)	0.85	[61]	0.93	[61]
Macor	MR	0.87	[59]	0.2*	[61]
MLI	S/C	0.6	[62]	0.3	[62]
Sigraflex	S	0.47	[51]	0.7*	[61]
Sm2Co17 (Ni plating)	MG (out)	0.11	[63]	0.38	[61]
Steel St37	PS (out)	0.38	[61]	0.58	[61]

higher than 10%. In components where higher accuracy is required, the mesh can be refined, while elements of low interest can be modelled more roughly. The nodes defined during the GMM are called geometrical nodes. Each one has an assigned area, in such way that adding all the nodal areas would result in the total area of the model. Apart from the geometrical nodes, it is possible to define auxiliary nodes in the TMM, which do not have an assigned area. These nodes are used for defining the conductive couplings, or for computing the temperature at precise locations.

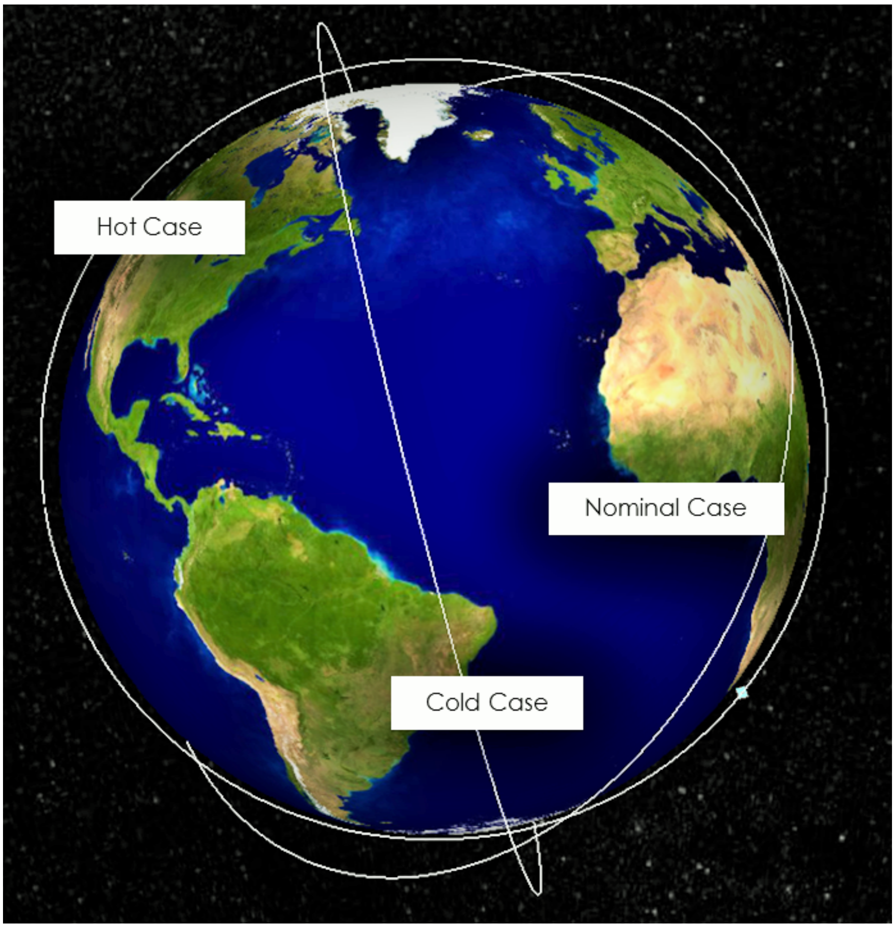

Figure 3.5: Illustration of the orbits for the three load cases, as viewed from the direction of the Sun

Given the radial symmetry of the model, the circumferential discretization is done with only four nodes, as if divided into quarters. When using finite elements instead of the lumped parameter method, it would have been enough to model a quarter of the thruster, and apply the symmetry boundary conditions on the edges, but this is not the case.

Once the GMM has been set up, it is necessary to define the mission. The mission is defined by a trajectory (orbit) and kinematics (attitude). Given that there are three load cases (hot, cold and nominal), the mission is divided into three phases, each one corresponding to one of the load cases. The duration of each phase shall be sufficient to ensure that a steady-state solution is achieved. Notice that due to eclipse periods the temperatures of the thruster will change during the orbit. Hence, a steady-state solution does not mean that the temperatures are maintained constant, but rather that they are bounded by maximum and minimum values. The characteristics of each orbit were presented in table 3.2. Figure 3.5 shows the three orbits as seen from the direction of the Sun. It is possible to appreciate that the hot case has no eclipse, while the cold and nominal orbits have segments covered by the Earth.

With the GMM and the mission, it is finally possible to calculate the radiative couplings of the model and the external heat fluxes coming from the celestial bodies. The Systema Thermica tool computes the view factors of all surfaces through ray-tracing algorithms based on Monte Carlo simulations.

Thermal Mathematical Model

Continuing with the model elaboration, the next step is to define the conductive couplings. This is done node by node, connecting adjacent nodes while following the heat flow path. The equation 3.1 shows the conductive coupling, GL, between two nodes is as follows:

$$GL = \lambda \frac{A}{L} \qquad W/K \tag{3.1}$$

where λ is the thermal conductivity of the material, A is the area normal to the heat flow direction and L is the distance between nodes. The conductive couplings can be added in a similar way to capacitors in electric circuits. Conductive couplings in parallel are added, while the conductive couplings in series are summed inversely. When defining the conductivity between two parts, a new term has to be considered: the contact conductivity (CC). Equation 3.2 shows an example of conductive coupling between nodes on different parts.

$$GL = \frac{1}{\sum \frac{1}{\lambda \frac{A}{L}} + \sum \frac{1}{CC \cdot A}} \tag{3.2}$$

While the thermal conductivities of the materials are fixed values and can be obtained from the literature, the contact conductivities have a high dependency on the surface roughness and the pressure between the parts, which is why sometimes experiments are carried out to find out the contact conductivities of the set-up [64]. The literature presents high dispersion in the values for the contact conductivities. Considering only an aluminium-aluminium interface, the values found in the literature are: 1,600-14,000 W/m^2/K [65]; 10,000-120,000 W/m^2/K [66];

2,000-12,000 W/m^2/K [67]. As another example, ceramic-metal interfaces have values in the range of 1,500-8,500 W/m^2/K [67]. This is a source of uncertainty that will be dealt with in a later stage of the model. In addition, the heat capacities, C of the nodes are defined, following equation 3.3:

$$C = \rho \cdot V \cdot c_p \qquad J/K \tag{3.3}$$

where ρ is the density, V is the volume and c_p is the specific heat capacity at constant pressure. Table 3.14 shows the values of thermal conductivity, density and specific heat capacity for all the materials in the thermal model.

Table 3.14: Material properties: thermal conductivity, density and specific heat capacity. (*) Values for parallel to plane and perpendicular to plane heat transfer, respectively.

Material	**Ref.**	**Part**	**Thermal Cond. [W/m/K]**	**Density [kg/m^3]**	**Specif. Heat Cap. [J/K/kg]**
Al. 7075	[68]	H, FR, R, MP, M	130	2800	915
Brass	[69]	A	60.6	8714	385
Boron Nitride	[70]	AH	30	2000	600
Macor	[49]	MR	1.46	2520	790
Sigraflex	[51]	S	190/5*	1121	700
Sm2Co17	[46]	MS	11.63	8400	376.8
St37	[71]	PS	42.7	7900	477

The final step on setting up the TMM is to define the boundary conditions. In this case, the spacecraft panel is modelled as a boundary node with constant temperature of 223 K (-50ºC), calculated as the equilibrium temperature for a cubic spacecraft of 900 cm^2 area (from dimensions 30x30 cm) in Earth orbit and covered in MLI. There are both radiative and conductive couplings between this node and the thruster. As there is no interest in the change in temperature of the spacecraft, considering it as a boundary node is a simplification of the model. Moreover, having a spacecraft wall at 248 K (-25ºC) has a negligible effect on the temperatures of the thruster (around 1 K variation). Having a spacecraft with a wall temperature of -25ºC would be the extreme hot case, as the thruster would radiate less heat into the wall. The negligible change in temperature justifies the use of the boundary node. Appendix A shows the results of the simulations that assess the impact of the s/c all temperature on the thruster temperature.

Thruster Thermal Losses

The mN-μHEMPT, as any other propulsion system, does not have a perfect efficiency. This means that from the input power to the thruster, part is transformed into thrust (the desired outcome), but another part is lost (undesired outcome). One of the power losses is the heating of the thruster. As it was explained in chapter 2, the location of these losses is at the poleshoes and anode, but the physical process of the plasma-wall interaction is not well understood. The way of including the process in the thermal model is to define an input power at each thermal loss location. Although no modelling of the plasma is necessary, the value of the input power at each location has to be calculated.

Table 3.15: Variables from thruster firing test for preliminary calculations of thermal losses

Test Variable	Units	Value
Anode Voltage	[V]	700
Anode Current	[A]	0.1429
Mass Flow	[mg/s]	0.2929

As a first estimation of the order of magnitude, an analytical calculation of the thermal losses is possible. Recalling equations 2.1 to 2.11 from chapter 2, as well as the experimental values obtained from a thruster firing test (see table 3.15), it is possible to compute the losses. Firstly, the beam characteristics are estimated. In particular, the beam current is 60-70% of the anode current [72], and the beam voltage is usually 80% of the anode voltage. With these values, it is possible to compute the beam power:

$$\begin{aligned} V_b &= V_A \cdot 0.8 = 560\,V \\ I_b &= I_A \cdot 0.7 = 0.10003\,A \\ P_b &= V_b \cdot I_b = 56.02\,W \end{aligned}$$

With the beam current, the ionization power can be computed. The ionization power is calculated multiplying the beam current times the ionization energy. For Xenon, IE is 12.1298 eV or 1170.4 kJ/mol.

$$P_i = I_b \cdot IE = \frac{0.10003}{e \cdot N_A} \cdot 1.1704 \cdot 10^6 = 1.21\,W$$

However, in order to also consider the excitation losses, a correction of the ionization energy can be applied, depending on the discharge performance and the propellant utilization efficiency. Instead of ionization energy, the modified variable is referred to as discharge loss, L_{dis}. A normal assumption with the low propellant utilization efficiency of the thruster considered (i.e. below 90%) is a discharge loss of 7.5 times the ionization energy: 90.97 eV, or 8777.3 kJ/mol [19].

$$P_i + P_{exc} = I_b \cdot L_{dis} = I_b \cdot 7.5 \cdot IE = \frac{0.10003}{e \cdot N_A} \cdot 7.5 \cdot 1.1704 \cdot 10^6 = 9.10\,W$$

Notice that, in order to have the appropriate units, the beam current is divided by Avogadro's number, N_A and the electron charge, e. Ultimately, the input power to the thruster is obtained from multiplying anode voltage times anode current:

$$P_{in} = V_a \cdot I_a = 700 \cdot 0.1429 = 100.03\,W$$

Finally, it is possible to introduce all the values in equation 2.6 in order to obtain the thermal losses (P_{loss}):

$$\begin{aligned} P_{in} = P_{out} = P_b + P_i + P_{exc} + P_{loss} \quad &\rightarrow \\ P_{loss} = 100.03 - 56.02 - 9.10 = 34.91\,W & \end{aligned}$$

With this calculation, the obtained result is that around 35% of the input power becomes thermal losses. This is an analytical approximation used only to obtain the order of magnitude. This number represents the total amount of thermal loss, but it does not give any information on the location of these thermal losses. As it was seen in chapter 2, the thermal loss distribution for the HEMPT development at TED were computed as percentage of the total thermal losses:

8% at the downstream poleshoe, 44% at the middle poleshoes and 48% at the anode. This distribution will be used as baseline for the Thermal Model, although the differences in size and design between the TED HEMPT and the mN-μHEMPT will undoubtedly have an impact on this heat loss distribution.

Summary of Assumptions and Uncertainties

As a recapitulation, this section includes a list of the assumptions (see table 3.16) and uncertainties (see table 3.17) of the model, as well as their impact on the thermal model.

Table 3.16: List of assumptions used on the thermal model. The impact on the thermal model is calculated with the sensitivity analysis, which can be seen in appendix A.

Assumption	Justification	Impact on the Thermal Model
Geometry modelled with simple shapes	Normal procedure (Systema)	+/-1.6ºC
Spacecraft panel modelled as a 30x30 cm rectangle	Sufficient size to cover thruster in cold case	Not assessed
Spacecraft covered in MLI at -50°C	Computed as equilibrium temperature	+/-1ºC
Neutralizer omitted from thermal model	Complicated modelling	+1ºC
Heat pipes modelled as a conductive coupling	Complicated modelling	-
Heat flows evenly through all cross-sectional area	Normal procedure [34]	-

The impact on the model of these assumptions are calculated through estimation. First the assumptions were done, and then the impact was estimated with the sensitivity analysis of the model.

Modelling the geometry with simple shapes is required by Systema. Given that the thruster does not have complex shapes, it is expected that the error introduced in the model will be small, and have a limited impact on the thermal model. During the sensitivity analysis, it was calculated that the effect on the temperature is in the order of +/-1.6ºC. The calculation of this value is further described in section 3.4 when computing the errors of the validation model set up.

The spacecraft panel, as mentioned before, is modelled as a 30x30 cm rectangle. This is a valid assumption because the objective is to cover the thruster during the cold load case, so that it does not receive any Sun radiation. Clearly, having a smaller panel wall would have an impact on the temperatures of the thermal model, reducing them (the thruster would radiate more into space). However, there is no information on the spacecraft in which the thruster will be used, as well as the thruster location. Given that this is the first thermal model developed, and that the assumption is conservative in the hot case, the impact of having a smaller side wall is not further investigated, and left for further developments, as the temperature would only be reduced. Regarding the temperature of the side wall, the assumption of -50ºC for the spacecraft outer temperature could have an impact of +/-1º variation, as deduced from the sensitivity analysis in appendix A, where temperature was augmented and reduced further 25ºC.

In the case of the neutralizer, it is not included in the model due to the fact that the complexity of modelling it trumps its impact on the model results. The impact is calculated in section 3.4, again when computing the errors of the validation model set up.

In the case of the heat pipes, their temperature distribution is not an interesting information for the thruster design. Given that they are COTS components, the specification data is reliable. Using their dimensions and the thermal resistance of 0.7 K/W [73], the conductive coupling between anode holder and radiator is accurate, so there is no impact on the thermal model.

Finally, the way of calculating conductive couplings would be perfect if the heat flowed evenly through the complete cross-sectional area between nodes, filling up every corner of each part. However, this is not what happens in reality, as heat flows with the thermal gradient and the effective cross-sectional area between different nodes may be reduced. The heat does not have to fill up every corner of the part. In the case of the thruster, the parts are so small (between milimeters and centimeters) that a sufficiently refined node mesh will avoid this problem. A rule of thumb for ensuring that the mesh does not require further refinement is that the temperature difference between two adjacent nodes should not be higher than 10 %. This assumption, once again, has no impact on the thermal model.

Table 3.17: List of uncertainties of the thermal model

Uncertainty	**Initial Assumption**
Thermal losses	35% of input power considered losses (analytical estimation)
Spatial distribution of losses	Used Thales HEMPT3050 thermal losses distribution as reference
Contact conductivities	Values from literature between 500 and 1,000,000 W/m^2/K

All these uncertainties have to be eliminated in order to obtain a consistent model. The model validation strategy has been designed in a way that all these three uncertainties are avoided, as it will be described in the following section.

3.4. Model Validation

In order to ensure that the results obtained from the thermal model are correct, the model has to be validated. The model validation of the mN-µHEMPT will consist in correlating the temperatures obtained with the model simulation to the temperatures measured during testing of the Engineering Model. When the thermal model is capable of accurately reproducing the temperatures reached during the firing of the thruster, the model can be used for drawing conclusions about the thermal performance of the thruster in orbit. The environmental characteristics in orbit are well known, and can be accurately simulated with the tools Systema. The uncertainty lies in the thermal losses and contact conductivities. By validating the model, the uncertainties will be cleared, and the thruster model will have a performance comparable to the real thruster, regardless of the boundary conditions of the problem.

Validation Strategy

The validation of the thermal model aims to obtain a GMM and TMM of the mN-µHEMPT that can accurately reproduce the temperatures of the real Engineering Model. All characteristics of the GMM and TMM have been obtained from the literature or from the design specifications of the EM, as exposed in the previous section. Only three uncertainties remain to be cleared in order to have a complete thermal model. As it was presented in table 3.17, the uncertainties in the model are: thermal losses, distribution of these losses and contact conductivities. During the model validation, these uncertainties have to be cleared. The validation strategy follows several steps in order to achieve this, and the method used is the correlation of the model results to experimental test results. The process is described as follows:

1. Correlation to heater testing in steady-state
    - With the system turned off, a heater raises the temperature of the system.
    - As the input power and its location is known, it is possible to correlate the contact conductivities of the Thermal Model.
2. Correlation to thruster testing in steady state
    - It is possible to correlate the thermal losses distribution fitting the model to the thruster test data.
    - The test did not reach a perfect steady state, so the exact value of the thermal losses cannot be correlated.
3. Correlation to thruster testing in transient
    - With the contact conductivities and thermal losses distribution fixed, the value of the thermal losses can be correlated.
    - This also allows to compute the steady state of the thruster testing as predicted by the model (necessary in this case because the thruster firing test did not reach a steady state).
    - Finally, a worst-case value of the thermal losses can be computed, for which the model always overestimates the temperature.

The initial correlation is done with the heater tests, which consist in measuring the temperature of the thruster when applying 10 W, 15 W and 25 W of thermal power through a heater located in the anode holder. The tests are described in detail in the following section. As the thruster is turned off, there are no thermal losses from the discharge chamber, so the input power of the Thermal Model, as well as the location of this power is accurately known. Given that these two uncertainties are not present anymore, the correlation of the thermal model to the test results is done by modifying the contact conductivities (the remaining uncertainty). This procedure had beed used in the literature as a way to know the order of magnitude of the thermal losses in the HEMPT [24]. The values of the contact conductivities obtained are then frozen for the following validation activities.

From this point onwards, figure 3.6 shows the validation strategy step-by-step. This is just an illustration for the temperature at an arbitrary location, and does not contain real data. The thruster test carried out was done with the Engineering Model firing at 100 W input power during 4.5 hours, during which the temperature of the thruster was measured. The thruster approached the steady state, but did not reach it completely due to problems during testing (achieving a steady state would have simplified the process). The test result is represented by the blue circles line in figure 3.6. With this data, several model correlations are possible.

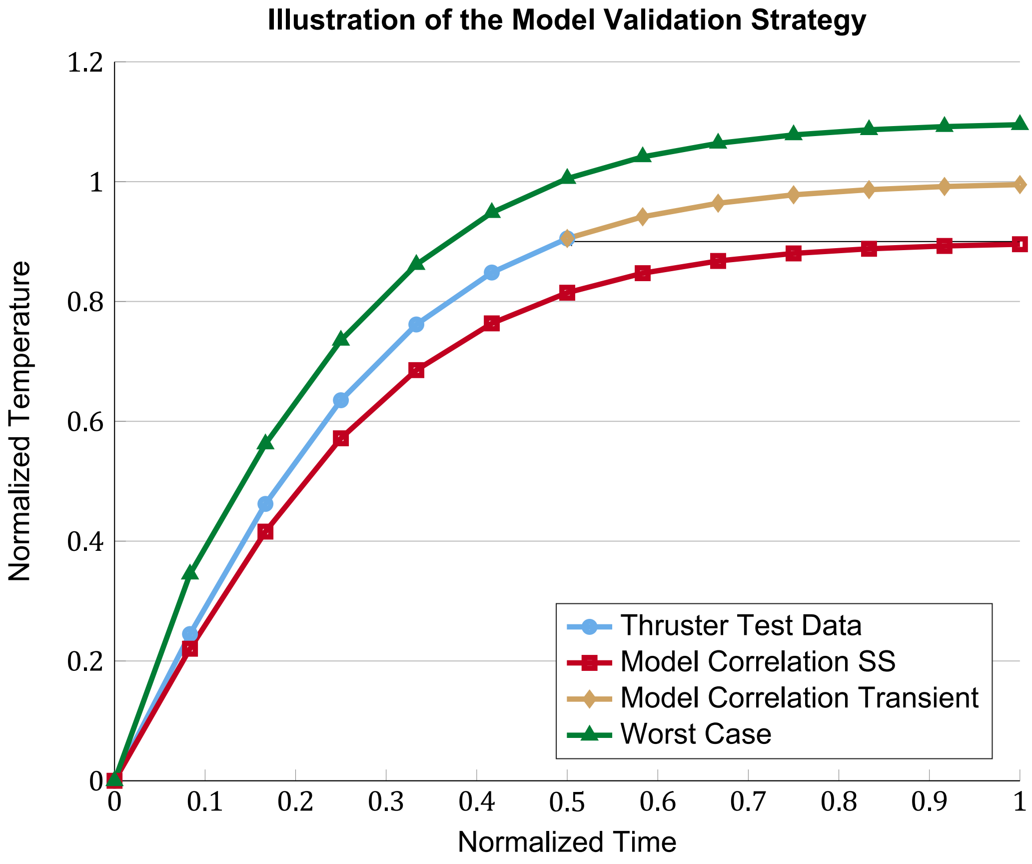

Figure 3.6: Illustration of the model validation strategy

In the first model correlation, the maximum temperature reached by the thruster is considered as a final steady state temperature. The correlation is done for the steady state temperature of the model, for which the red squares line is obtained. The purpose of this correlation is to find the thermal losses distribution. The value of the total losses modifies the temperature of all nodes in a similar way (as if applying an offset), so it is possible to find a value for which the temperatures of the model and the test are similar in an average value (in this case, it was 14.2 W). This value for the thermal losses is not accurate, as the correlation is done for the maximum temperature reached in the test and not for the real steady state. This explains the fact that in figure 3.6 the red squares line does not fit the test data (blue circles line), but the steady state of the former is similar to the maximum temperature of the latter. Fixing the total thermal losses leaves only one uncertainty: the thermal losses distribution. Modifying these parameters changes the temperature of each node differently. The correlation is done by fitting the model temperature at each node to the measured temperatures at the corresponding locations. In this way, a distribution for the thermal losses is achieved.

Subsequently, the model correlation is done for the transient. With the contact conductivities and thermal losses distribution obtained from previous correlations, this time the transient curve of the model is fitted to the thruster test curve. The parameter to be changed is the thermal losses. Normally, during correlations with transient data it is also possible to calculate more accurate heat capacities. However, these are assumed to be correctly modelled due to the fact that the geometry and material properties are well known for the thruster, and higher uncertainty is present in the thermal losses. This correlation confirms the assumption, as the curve shape obtained by the model is similar to the test. The curve obtained is the yellow diamonds curve in figure 3.6. It overlaps the thruster testing and continues further in time until reaching the steady state. The way to obtain this curve is to change the value of the thermal losses, which in the end is 14.5 W. With this model, in which all uncertainties have been cleared, it is possible to compute the steady state that the thruster testing should have reached.

The final step is to apply a safety factor to the model validation. If the model always overestimates the temperatures, then it always considers a worst case scenario. This is valid for hot case, in which a maximum temperature for the magnet stack limits the design. The cold case is less critical. Even if small errors had been done in the modelling process, they are accounted for in this margin of safety. To determine the worst case, the requirement was that the model should overestimate the temperature of the thruster during the transient and steady state, but not in more than 10ºC. This latter requirement is necessary to still have representative results. A very high margin of safety results in an unrealistically high temperature, which would have led to an oversized thermal control system. In order to compute this worst case, the variable modified is the thermal losses value, as it merely applies an offset to all thruster temperatures. The worst case is represented by the green triangles line in figure 3.6, always above the blue circles line, which represent the EM testing, and the value of thermal losses obtained for this worst case was 17.6 W.

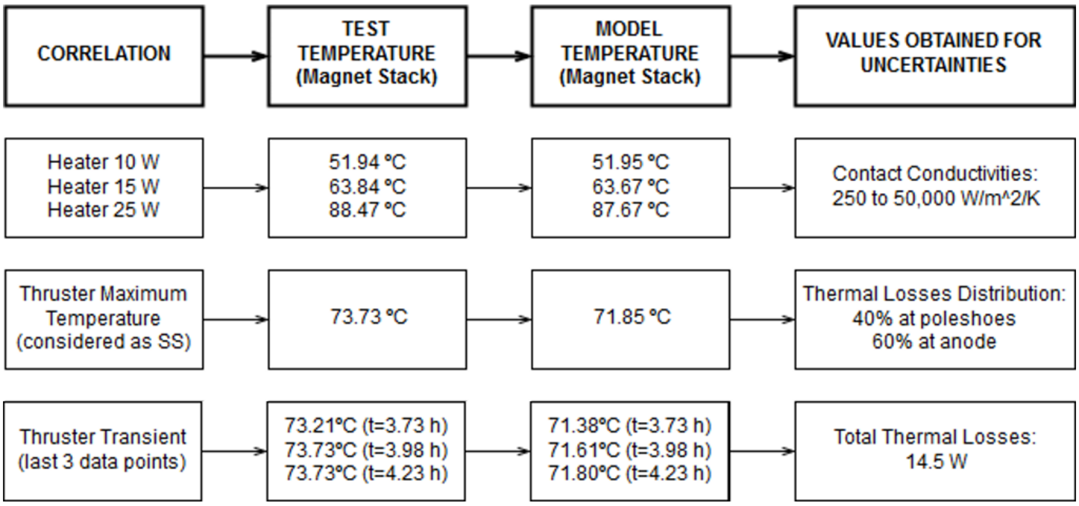

CORRELATION	TEST TEMPERATURE (Magnet Stack)	MODEL TEMPERATURE (Magnet Stack)	VALUES OBTAINED FOR UNCERTAINTIES
Heater 10 W Heater 15 W Heater 25 W	51.94 °C 63.84 °C 88.47 °C	51.95 °C 63.67 °C 87.67 °C	Contact Conductivities: 250 to 50,000 W/m^2/K
Thruster Maximum Temperature (considered as SS)	73.73 °C	71.85 °C	Thermal Losses Distribution: 40% at poleshoes 60% at anode
Thruster Transient (last 3 data points)	73.21°C (t=3.73 h) 73.73°C (t=3.98 h) 73.73°C (t=4.23 h)	71.38°C (t=3.73 h) 71.61°C (t=3.98 h) 71.80°C (t=4.23 h)	Total Thermal Losses: 14.5 W

Figure 3.7: Flowchart illustrating the model validation strategy and featuring an example with real values. The example taken is the correlation of the temperature at the magnet stack. The first correlation (heater testing) has the contact conductivities as the only uncertainty. The second correlation uses the maximum temperature reached in the thruster testing as steady state (as it was not possible to reach this state in the test), and obtaines the thermal losses distribution. The third correlation (transient of thruster test) checks the validity of the heat capacities and uses the last three data points to obtain the most accurate thermal losses.

With the idea of summarizing this validation process, as well as better illustrating the method used, figure 3.7 features an example with real values taken from the magnet stack temperature measurement and model values. It is clear that the temperature difference between model and test is always below the limits imposed by the requirements. Obtained from the literature, the conditions for the thermal model correlation (as indicated in requirements THR-TC-711/712/713) are: a maximum deviation of less than 3ºC, a mean deviation of less than 2.5ºC and a standard deviation of less than 3ºC [38, 39]. These restrictions are applied to every correlation followed in the validation process.

Test Set-up

The Laboratory of Enabling Technologies at Airbus Friedrichshafen counts with a micro-newton thruster test facility. It consists of a vacuum chamber (see figure 3.9) with an operational pressure in the 1E-6 mbar range. The chamber counts with over a cubic meter of capacity, necessary for reducing the influence of the walls on the thruster operation. It also needs to contain all the test supporting equipment. Inside the chamber, a micro-Newton thrust balance and a plasma diagnostics set-up have been installed [25].

In order to perform testing and characterisation activities, the Engineering Model of the thruster can be placed inside the chamber, either on the thrust balance or steadily attached to the chamber. Regarding the thermal measurements, these are done with PT100 thermistors [74], located in different points of the exterior of the thruster. A direct temperature measurement inside the thruster discharge chamber is not possible, as the plasma would damage the sensor. Figure 3.8 shows the different locations of the PT100 sensors. In total, 5 data points are used for the different tests, named TC1 to TC5. The thruster has to be mounted as thermally decoupled as possible. For this reason, the thrust balance counts with a macor component (low thermal conductivity) used as isolator between the thruster and the vacuum chamber. When mounting directly to the structure, there is no macor component, but the structure is made of anodized aluminium, which is has a very low thermal conductivity (1 W/m/K). In all tests, the thruster was mounted directly to the structure.

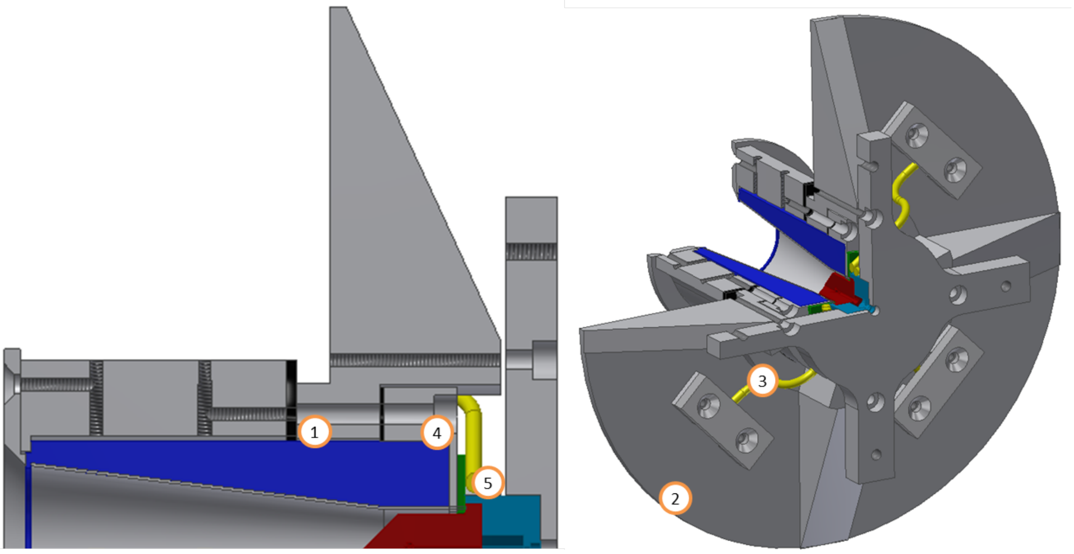

Figure 3.8: Locations of PT100s during the thruster testing. TC1: middle poleshoe (magnet stack), TC2: radiator outer part, TC3: radiator inner part, TC4: downstream magnet stack, TC5: anode holder.

During thermal testing of the thruster, the temperature is measured at the 5 locations described in figure 3.8. The result is a set of data temperature vs. time. Two different types of test were performed, which will be called from here onwards: heater test and thruster test. The former consists in applying a well-known thermal power into the thruster through a heater located on the anode holder, also in contact with the mount. The thruster is, in this case, switched off. The second type, thruster testing, consists in firing the thruster on a stable operation point and without changing the input power. For all tests, the thruster was fixed to the chamber, rather than attached to the thrust balance.

Three heater tests were performed, setting the heater input power at 10 W, 15 W and 25 W. Each test lasted for at least 6 hours, and in all cases the steady state was achieved (i.e. when the temperature of the system stays constant in time). The temperatures measured were around 50ºC, 65ºC and 85ºC, respectively. All testing results can be seen in appendix B.

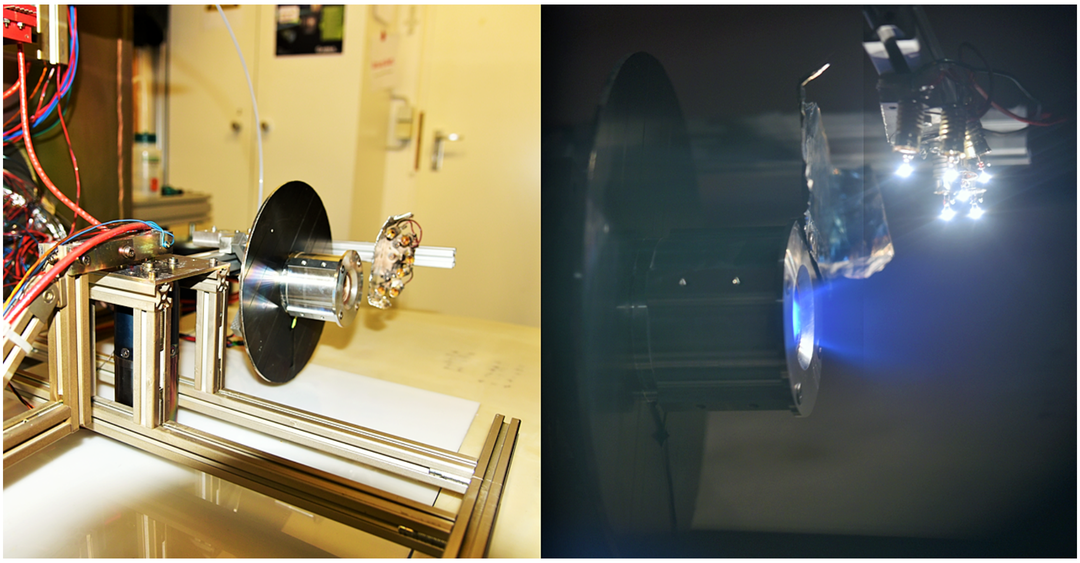

Figure 3.9: Thruster test set-up (left) and thruster firing (right)

Only one thruster test was performed, firing the mN-μHEMPT at 100 W input power during 4.5 hours. The propellant used was Xenon, at a mass flow rate of 3 sccm. Although the steady-state was not achieved, the change rate of the temperatures had begun to decrease, which indicated the approach of the steady state. The temperatures measured were in between 60ºC and 75ºC.

The results obtained from the testing have an error which can be estimated. The total error is the result of several error contributions, obtained from uncertainty in the measurement taking process and a testing set-up that is not ideal. While some of the errors can be computed/propagated and accounted for (systematic), others have to be estimated (statistical) [75]. Table 3.18 shows the error sources for the testing.

Table 3.18: Error sources and values from thruster and heater testing. HTR: heater, THR: thruster. X is an unknown value, as the error due to electronic noise from plasma interaction with the sensors could not be estimated, and only the sign of the error was deduced.

Error source	**Type**	**Test**	**Error [ºC]**
Extra resistance from cable length	Systematic	HTR 10/15/25 W	-2.8
	Systematic	THR firing	-2.3
Offset in measurement-taking program	Systematic	HTR 10 W	+6.2 (TC1); +7.7 (TC2); +7.4 (TC3); +14.8 (TC4); +7.4 (TC4)
	Systematic	HTR 15/25 W	+6.2 (TC1); +7.7 (TC2); +7.1 (TC3); +15.1 (TC4); +7.4 (TC4)
Glue between PT100 and components	Systematic	All	+/-0.002 (negligible)
Resistance measurement accuracy	Statistical	All	+/-0.8
Electronic noise from plasma interaction with the sensors	Statistical	THR firing	-X (TC2)

All errors from table 3.18 have been computed or estimated, except for the electronic noise from plasma interaction with the sensors, for which only the direction of the offset was calculated. The two first systematic errors from the table were computed with the help of a second measurement technique. Thermistors measure a resistance whose value changes with temperature. When adding a long cable, its resistance is added to the measured value. Before starting the measurements, the resistance of the sensors was measured with and without the cable, obtaining the offset values (-2.8ºC and -2.3ºC). The program for data read-out (built in Labview) converted the resistance into Kelvin degrees. However, in the process, an offset error was present. Measuring the resistance on the PT100s with a multimeter and comparing it to the program measurements gave the offset error. The last systematic error is the fact that the temperature measured by the sensors is not the temperature at the element, as a thin layer of glue lies in between. Computing the conduction through the glue, with a thickness of 0.2 mm and a thermal conductivity of 8 W/m/K, the temperature change turns out to be two to three orders of magnitude below the other errors (+/-0.002ºC), and thus negligible. The calculation of this value is part of the sensitivity analysis, further explained in appendix A.

As far as the resistance measurement accuracy is concerned, this error was computed by propagating an error in the resistance measurement into an error in the temperature. The PT100 resistance-temperature relationship is well defined in the product datasheet, reference [74], and it was calculated that a +/-0.3 Ohms resistance error is propagated as a +/-0.8ºC temperature error. This value is consistent with the observed reality, where the multimeter value read-out (with an accuracy of 0.1 Ohms) usually varied in +/-0.2 to +/-0.3 Ohms, as it did not stay fixed on a single measurement value.

Finally, the electric noise from plasma interaction with the sensors could not be estimated nor calculated at the time. It could only be assummed that the TC2 would be the point most affected for being the most exposed (outer edge of the radiator). The plasma would provoke an overestimation of the temperature at that point, which means that the error is only in the negative direction.

When presenting the test data, the error bar will be +/-0.8 (contribution from the PT100 accuracy measurement). This is because the offsets will already be incorporated in the data as corrections, given that they have been accurately calculated. The error due to plasma interaction is not considered, due to the lack of an estimate value, and the glue error is neglected.

Model Set-up for Validation

In order to validate the Thermal Model, it has to be adapted to the testing conditions. This means that, instead of in orbit, the thruster is placed in a model of the vacuum chamber. Given the high thermal mass of the chamber, made out of steel, the temperature of its walls is considered constant throughout all tests. This is implemented on the thermal model as boundary nodes, which can absorb and emit heat without changing their temperature. Figure 3.10 shows the thruster inside the vacuum chamber model. The optical properties of the chamber are described in table 3.19. While the side walls are directly made out of stainless steel with a rough finish, the bottom is covered by POM (Polyoxymethylene), part of the mechanisms that allows the displacement of the plasma diagnostics.

Notice that all the supporting equipment (e.g. cabling, intruments, mounting structure etc.) are not considered in the model. This is not a problem for the validation, as the temperature of these components is similar to the one of the vacuum chamber. The strategy followed to decouple the thruster from the chamber in terms of conduction was to add a macor component

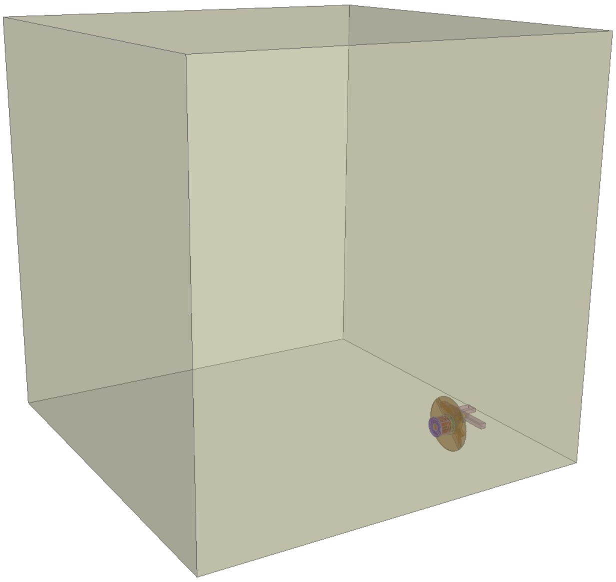

Figure 3.10: Illustration of the model set-up for validation showing the thruster inside the vacuum chamber

Table 3.19: Optical properties used on the Thermal Model

Material	**Part**	**Emissivity**		**Absorptivity**	
POM	Chamber Bottom Wall	0.95	[76]	0.2	[61]
Stainless steel (rough)	Chamber Side/Top Walls	0.38	[61]	0.58	[61]

in the interface. The resultant GL (conductive coupling) between the thruster and the chamber is 0.077 W/K. As an example, for the thruster firing with 17.6 W of thermal losses, the heat flux between thruster and chamber structure through conduction would be 2.54 W. This means that with the 0.077 W/K conductive coupling, almost a 15 % of the thermal losses are evacuated via conduction into the chamber wall.

Apart from the uncertainties previously described in table 3.17, the results obtained from the Thermal Model have an error. This error, as in the case of the testing data, is computed by combining different error contributions. They come mostly from modelling deficiencies or simplifications, and a summary of all error contributions can be seen in table 3.20.

Table 3.20: Error sources and values from thruster Thermal Model

Error source	**Symbol**	**Type**	**Error [ºC]**
Modelling Area Error	E_{area}	Statistical	+/-1.6
Conductive couplings	E_{gl}	Statistical	+/-1.0
Chamber boundary temperature	E_{cha}	Statistical	+/-1.0
Neutralizer not included in model	E_n	Systematic	+1.0
Optical properties	E_{opt}	Statistical	+/-4.2
Total error	$E_{tot} = \sqrt{E_{area}^2 + E_{gl}^2 + E_{cha}^2 + E_{opt}^2} + E_n$		+5.7/-4.7

The first error in table 3.20 refers to the fact that Systema Thermica uses only simple geometries (e.g. cylinders, cones, rectangles etc.). Thus, complex shapes from the Engineering Model cannot be introduced in the Thermal Model. The assumption of a 5% error in the area was propagated into thruster temperature error, and the result obtained is +/-1.6ºC. The calculation is further described in the appendix A.

Another error is due to the difference between the materials' specification and the real material used. Properties such as the thermal conductivity of a component may not be exactly as stated in materials reference databases. This plays a role in the conductive couplings calculations. Furthermore, the way of calculating these couplings is a simplification of reality, as heat does not follow straight paths from node to node, but rather moves with the temperature gradient. This is a statistical error, because the exact difference between model values and reality cannot be computed, so a 10% difference in values is assumed. The 10% errors on area, length and thermal conductivity are propagated into the GL, and then the GL error is propagated into temperature error (based on ECSS-E-HB-31-03A [37]). The error propagation is done via derivation of the GL equation with respect to the modified variable. Adding the contributions of the three errors (10% variation in area, length and thermal conductivity) via a squared sum, the result is only a 1°C error (rounded).

The following error is related to the assumption that the temperature of the chamber is constant. The chamber temperature used in the models was 18.22°C, as measured at the beginning of the tests. There are two effects that could change the temperature of the chamber: (i) the thruster heats up the chamber walls and (ii) heat from the vacuum chamber is extracted through radiation and conduction into the cryo-pumps and the ambient (outside the chamber, into the laboratory). The impact of boundary temperature variation is ultimately calculated as a 1°C error on the thermal model temperatures. This value was obtained by propagating a 5ºC temperature variation of the chamber wall into the temperature of the thruster, and the complete explanation can be found in appendix A.

Regarding the neutralizer, this was not modelled due to its little impact in terms of input power to the thruster, thus simplifying the model. However, a systematic error could be derived from this omission. The neutralizer radiates at 14 W/m^2 at a distance of 2 cm from the thruster. Considering half of the area of the radiator and half of the area of the housing are affected by this radiation, the input power into the thruster is 0.26 W, which results in a 1°C temperature change in the thermal model on average. This value is only in the positive direction, as the temperature of the thruster increases when introducing more incoming power. The results of the simulations with and without the neutralizer can be seen in appendix A.

Finally, the optical properties of the materials are the last error source of the model, affecting the radiative couplings. Specification values may differ from real material and coating values. In order to consider the worst case scenario, a simulation was performed raising 0.01 each absorptivity and reducing 0.01 each emissivity of the Thermal Model (based on ECSS-E-HB-31-03A [37]). The result is an error of 4.2°C in the model temperatures (maximum temperature difference, reached on the hot case), and the simulation results can be seen in appendix A. This gives an insight into the high sensitivity of the thermal model to the optical properties, and how coatings can be effective tools for passive thermal control, as just a small variation can lead to important temperature changes.

The calculation of the total error is done with a geometric addition (i.e. the square root of the sum of each error to the square [77]). This is common practice for uncorrelated statistical errors, as a simple addition would overestimate the error. In this way, errors for modelling of the areas, conductive couplings, boundary temperature and optical properties are added via geometric addition. On top of this result, the systematic errors are added, resulting in a +5.7/-4.7°C error (the difference between upper and lower error is introduced by the neutralizer, which only contributes to the upper error, see table 3.20).

Notice that the error (+5.7/-4.7ºC) is larger than the maximum deviation stated by requirement THR-TC-711 (+/-3°C). Model error and deviation requirements are separate values. Initially, the model has a calculated error (5.7ºC). During the model correlation, the values of the model are adjusted to fit the deviation requirements (3ºC). When this is achieved, the model is said to be ”validated”, and its error is lower than the deviation requirements (<3ºC).

Merit Figures for Best Fit Selection in Model Correlations

Once the test and model set-ups and errors have been defined, it is possible to perform the correlation to the testing results with the objective of validating the Thermal Model. Recalling the validation strategy, the procedure is as follows:

1. Correlation to heater testing in steady-state
2. Correlation to thruster testing in steady state
3. Correlation to thruster testing in transient

When performing a correlation, the design variables of the model are modified until it can reproduce the temperatures of the test with sufficient accuracy. The set of design variables which best fit the test data are taken as the final configuration. In the first correlation, the design variables are the contact conductivities. In the second one, they are the thermal losses distribution and the value of the total losses. Finally, in the third correlation, the design variable is only the value of the total losses.

In order to have a final configuration or ”best fit”, the results produced by the model must fulfil the following requisites:

- In terms of errors, all test data points with their error bars (+/-0.8ºC) have to fall inside the error bars of the model results (+5.7/-4.7ºC).
- In terms of deviations, requirements THR-TC-710/711/712 define limits to the maximum deviation (3ºC), mean deviation (2.5ºC) and standard deviation (3ºC) that have to be met.
- The temperatures produced by the model have to be consistent with the expected physical behaviour.

It is clear that meeting the requirements on deviations automatically means achieving the requisite of having the error bars of the test inside the ones of the model, because the former are more stringent. For this reason, the merit figures to be monitored during the design iterations are the deviations. Appendix C provides supporting information on all three correlation processes, showing the initial configurations and iterations followed. In this section, only final results will be presented.

A best fit or final configuration is not the best possible solution to the correlation problem. It is merely a solution that satisfies all three requisites. In this way, the results obtained from each correlation have limitations, and should be used carefully when drawing conclusions. The final objective is to have an accurate thermal model, so as long as the model does not exceed the deviations from the requirements and the physical behaviour is consistent, there is no need in further refining the values of the design variables.

The formulas for the maximum, mean and standard deviation are as follows:

$$Maximum\ Deviation = max(T_{n,model} - T_{n,test}) \tag{3.4}$$

$$Mean\ Deviation = \frac{\sum_{n=1}^{N} \mid T_{n,model} - T_{n,test} \mid}{N} \tag{3.5}$$

$$Standard\ Deviation = \sqrt{\frac{\sum_{n=1}^{N} (T_{n,model} - T_{n,test})^2}{N}} \tag{3.6}$$

Table 3.21 shows the deviations in the different model correlations. All final configurations meet the requirements. When analysing each individual correlation, the requisites on errors and physical behaviour will also be verified.

Table 3.21: Maximum, mean and standard deviations for the different test correlations

Correlation	**Max. Deviation [°C]**	**Mean Deviation [°C]**	**Std. Deviation [°C]**
Heater 10W	1.60 (TC5)	0.61	0.85
Heater 15W	2.76 (TC5)	1.02	1.42
Heater 25W	1.96 (TC2)	1.43	1.50
Thr. steady state	2.85 (TC4)	1.65	1.96
Thr. transient (mean values)	2.80 (TC4)	1.62	1.91

Heater Testing Correlation via Variation of Contact Conductivities

To begin with, figure 3.11 shows the model correlation to the heater testing. All three tests are shown: 10 W, 15 W and 25 W, together with the model results for those heater input powers (final configuration). The purpose of this initial correlation is to fix the values of the contact conductivities of the model. These values, as seen in the previous sections, have a high uncertainty.

The correlation was performed by running the simulation with different contact conductivities until achieving a ”fit” (i.e. all testing data values, together with the error bars, fall inside the error bars of the model). This was achieved for every measurement point at every input power, except for TC5 in the 25 W test. This measurement point is located on the anode holder, exactly where the heater is attached. Given that the heater is the only source of heat, it is clear that this point should reach the highest temperature of the thermal model. It is thus concluded that an error is taking place in this measurement, and it is not considered in the correlation. The contact conductivity values can be seen in table 3.22.

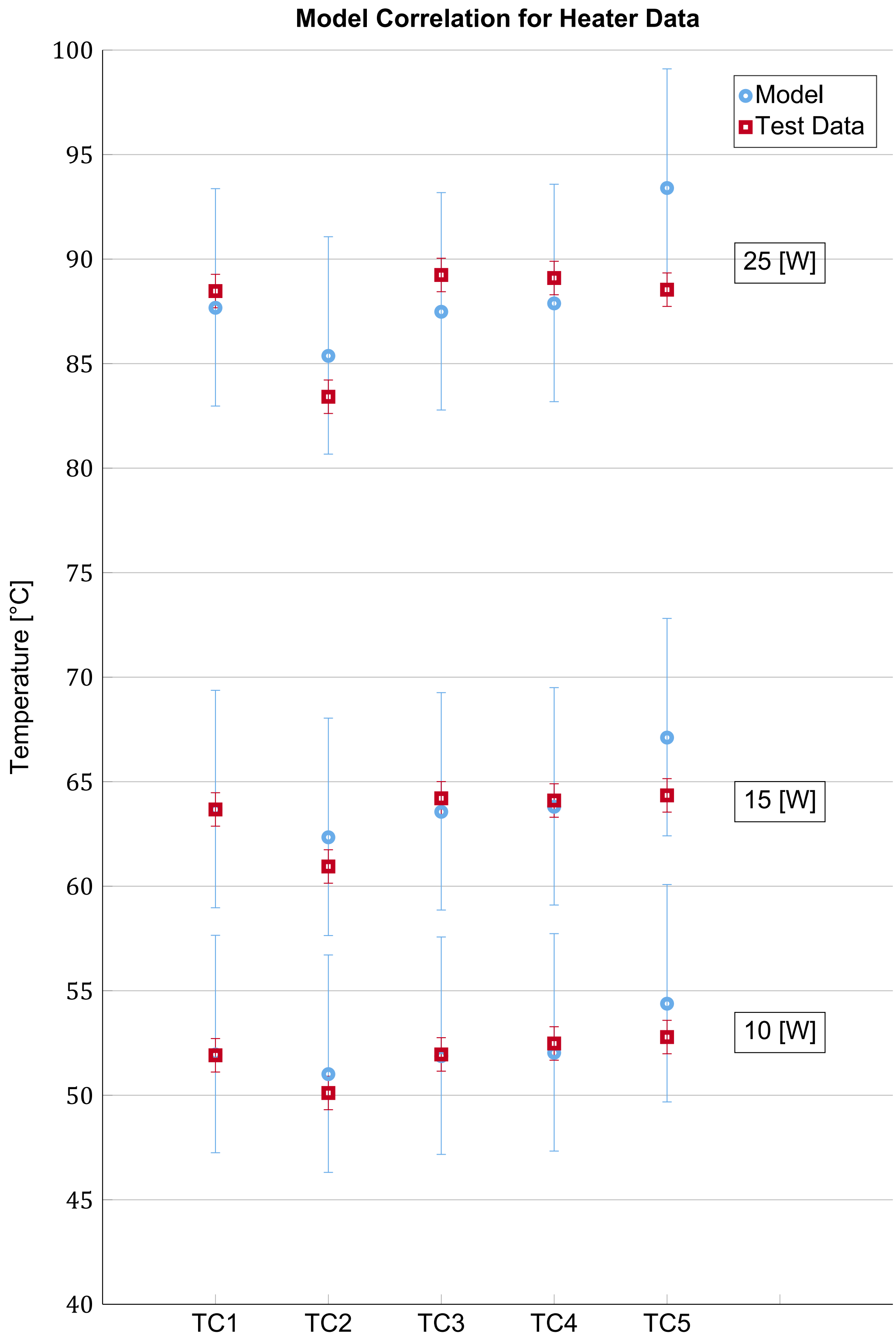

Figure 3.11: Test and model predicted temperatures for heater testing (10, 15 and 25 W) steady state at the five temperature measurement locations. Error bars for model: +5.7/-4.7°C, error bars for test: +/-0.8°C.

The merit figures used for selecting the best fit were the maximum deviation, required to be under 3°C (req. THR-TC-711), the mean deviation, required to be under 2.5°C (req. THR-TC-712) and the standard deviation, required to be under 3°C (req. THR-TC-713). All values were already shown in table 3.21. Apart from meeting these requirements, the temperatures need to be consistent with the expected physical behaviour. In this sense, the results are satisfactory: bolted joints have a high contact conductivity (e.g. radiator-housing) and parts with low thermal conductivity have low contact conductivity values (e.g. macor ring). In appendix C, an in-depth explanation of the process followed is included, with the evolution of the contact conductivity values during the model correlation.

Table 3.22: Contact conductivities after correlation to heater tests

Interface	**Materials**	**CC [W/m^2/K]**
Magnet - Housing	Sm2Co17 - Aluminium	10,000.0
Magnet - Front Radiator	Sm2Co17 - Aluminium	10,000.0
Magnet - Magnet Press	Sm2Co17 - Aluminium	10,000.0
Magnet - Spacer	Sm2Co17 - Sigraflex	10,000.0
Magnet - Poleshoe	Sm2Co17 - St37	20,000.0
Magnet - Chamber Coating	Sm2Co17 - Boron Nitride	250.0
Poleshoe - Magnet Press	St37 - Aluminium	12,000.0
Poleshoe - Chamber Coating	Sm2Co17 - Boron Nitride	250.0
Housing - Front Radiator	Aluminium - Aluminium	50,000.0
Radiator - Spacer	Aluminium - Sigraflex	50,000.0
Radiator - Housing	Aluminium - Aluminium	50,000.0
Radiator - Mount	Aluminium - Aluminium	50,000.0
Radiator - Heat Pipes	Aluminium - Copper	45,000.0
Magnet Press - Spacer	Aluminium - Sigraflex	12,000.0
Magnet Press - Macor Ring	Aluminium - Macor	800.0
Mount - Vacuum Chamber	Aluminium - Anodised Al.	12,000.0
Anode Holder - Macor Ring	Boron Nitride - Macor	800.0
Anode Holder - Anode	Boron Nitride - Brass	1,000.0
Anode Holder - Mount	Boron Nitride - Aluminium	500.0
Anode Holder - Heat Pipes	Boron Nitride - Copper	45,000.0
Anode - Macor Ring	Brass - Macor	800.0
Anode - Chamber Coating	Brass - Boron Nitride	500.0

Thruster Testing Correlation via Variation of Thermal Losses Distribution

The next step of the model validation is to obtain the thermal losses distribution. This is done by correlating the Thermal Model to the thruster testing in steady state configuration. As it was mentioned previously in this section, the thruster test did not reach a steady state during testing. In order to work around this problem, the maximum temperature reached during the test is used as steady state temperature. The limitation of using this temperature is that the real steady state has a higher overall temperature and there is a smaller relative difference between the measurement points (i.e. the heat in steady state is better distributed, reducing the temperature gradients). This is due to the heat capacities and heat conduction: the small components close to the thermal losses will heat up faster than the high thermal mass components far away from the losses, because they need more time. In the steady state, time does not play a role anymore, and the result is that the temperatures are better distributed than at any point in the transient. It is important to bear this in mind when drawing conclusions from this correlation.

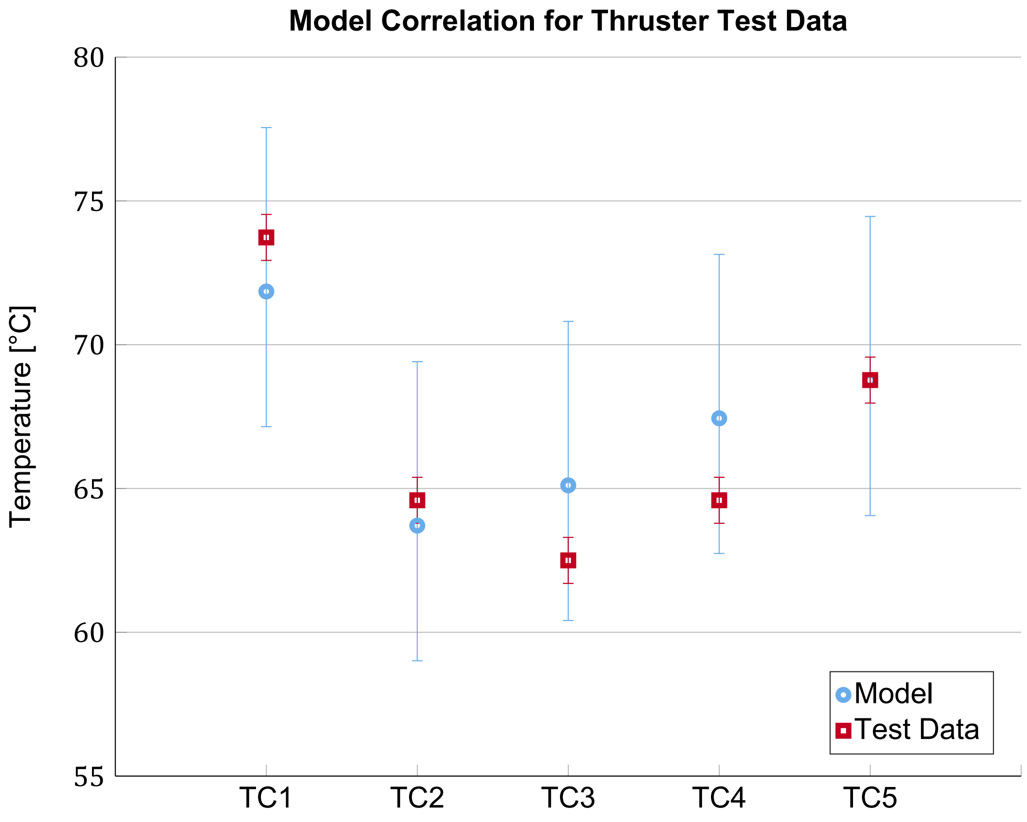

Figure 3.12: Test and model predicted temperatures for thruster testing steady state at the five PT100 locations. Error bars for model: +5.7/-4.7°C, error bars for test: +/-0.8°C.

Figure 3.12 shows the test and model temperatures for each PT100 location. A good fit is achieved, as all the test temperatures with their error bars fall inside the error bars of the model, and the deviations are within the requirements. Table 3.21 already showed the deviations (mean, maximum and standard) between model and test data for the final configuration. The fit is achieved by tuning the thermal losses distribution, and the values selected can be seen in table 3.23 as percentage of the total value of the thermal losses. This result was obtained by changing the thermal loss percentage at each location. The step in this variations was 2 percentage points or less. This gives an error of +/-2% to the values for heat distribution obtained. Appendix C further explains the correlation process, showing the initial values for the thermal losses distribution and their evolution until reaching the final results.

While the thermal losses distribution are the variables selected via this correlation, there is still one variable with room for modification: the value of the thermal losses. This value is chosen arbitrarily in order to fit the model, as it displaces upwards or downwards all model temperatures, equal to applying an offset. The value selected was 14.2 W, but it is not the real value of the thermal losses. Because of using the maximum temperature reached during the test and not the steady state, the value of thermal losses that best fits the data is lower than the real one (as it was shown previously when explaining the validation strategy, see figure 3.7). The real thermal losses value will be calculated with the next correlation.

Table 3.23: Thermal losses distribution for the mN-μHEMPT (Airbus) and the HEMPT3050 (Thales). Locations of the thermal losses are: downstream poleshoe (A), middle-downstream poleshoe (B), middle-upstream poleshoe (C) and anode (D).

Thruster	**Thermal Losses Distribution A/B/C/D [% of Total Losses]**
HEMPT3050 (Thales)	8/32/12/48
mN-μHEMPT (Airbus)	2/28/10/60 +/-2%

On table 3.23, the thermal losses distribution for the mN-μHEMPT (Airbus) and the HEMPT 3050 (Thales) are presented. The significant differences between the mN-μHEMPT and the HEMPT 3050 were expected, as the systems have different sizes as well as different magnetic field design. The values from the HEMPT3050 were however a suitable starting point for the iterations in order to find the best fit.

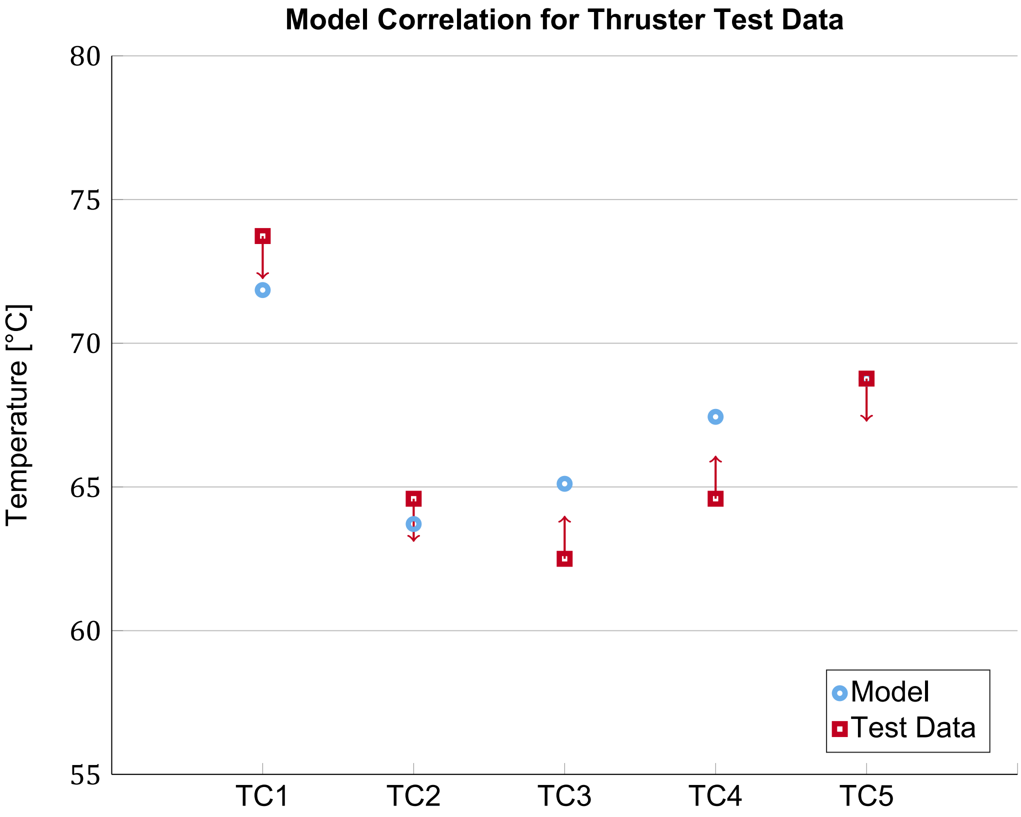

Figure 3.13: Test and model predicted temperatures for thruster testing steady state at the five PT100 locations. Arrows on test data show direction of temperature evolution (and not value) when corrected for steady state error and plasma interaction.

The temperatures of the data points are consistent with the expected physical behaviour. TC5 (anode holder) and TC1 (middle poleshoes) were expected to reach the highest temperatures for being the closest to the heat sources. This is the case for both the model and the test data. It was expected that TC2 (outer part of the radiator) would have the lowest temperature, because it is the furthest away from the heat source. Although this is the case for the model, it is not in the test data. The reason behind this is the error due to not having a steady state and due to the plasma interaction with the sensors (recalling table 3.18, this error affected the TC2 sensor for being the most exposed to the plasma).

Figure 3.13 shows how the test data is expected to behave, should the errors from steady state and plasma interaction be removed. The arrows show the direction (and not the value) of the relative displacement of each temperature with respect to the others. TC1 would have a temperature closer to the other nodes because in transient the poleshoes heat up more quickly than other model parts (low heat capacity and close to the heat source). This is also the case of TC5. TC3 and TC4 would suffer the contrary effect: their relative temperature would increase once they stop depending on the high thermal intertia at the steady state. Finally, TC2 has two counter-acting effects: temperature should rise if considering the steady state, but the plasma interaction increases the temperature measured by the PT100, which would mean that the real temperature is lower. Following the physical understanding of the system, the plasma effect must outweigh the steady state effect, in order to have a lower temperature at TC2 than at TC3. The conclusion is that the corrected test data would be closer and more similar to the Thermal Model.

Thruster Transient Correlation via Variation of Total Thermal Losses

At this point, the only source of uncertainty left is the value of the total thermal losses. In order to overcome this uncertainty, the model is correlated to the transient thruster test. This is done by finding the thermal losses value that best fit the transient data. The best fit is found by minimizing the difference between test data and model. This is done for the three last measurements of the thruster test before switch off (t=3.73, t=3.98 and t=4.23 hours). The reason for this is that the three last points are very close to the steady state, which means that the data is more reliable and does not contain the perturbations of initial warm-up (there were a total of 30 measurements until turn-off).

The heat capacities were calculated accurately with the material properties and dimensions, resulting in a good fit to the test data shape (see figure 3.14), and only the thermal loss value is modified, with a minimum change of 0.1 W. The best fit is obtained for thermal losses of 14.5 W, and the deviations between model and test were presented in figure 3.21. Appendix C further explains the correlation process. It also shows the results obtained for 14.4 W and 14.6 W to prove that the value chosen is the best fit.

Table 3.24: Temperature difference between test data and model for the last three measurements at all five locations

Time [h]	TC1 [°C]	TC2 [°C]	TC3 [°C]	TC4 [°C]	TC5 [°C]
t=3.73	1.83	0.62	-2.32	-2.89	0.16
t=3.98	2.13	0.85	-2.37	-2.65	0.21
t=4.23	1.93	0.89	-2.60	-2.87	0.03

Figure 3.14 shows the test and model temperature evolution at all temperature measurement locations (TC1 to TC5). Table 3.24 shows the temperature difference between the test data and the model for the last two measurements at all five locations. The result is consistent with the steady state calculation, where the model overestimated temperatures at TC3 and TC4 and underestimated the temperatures at TC1, TC2 and TC5.

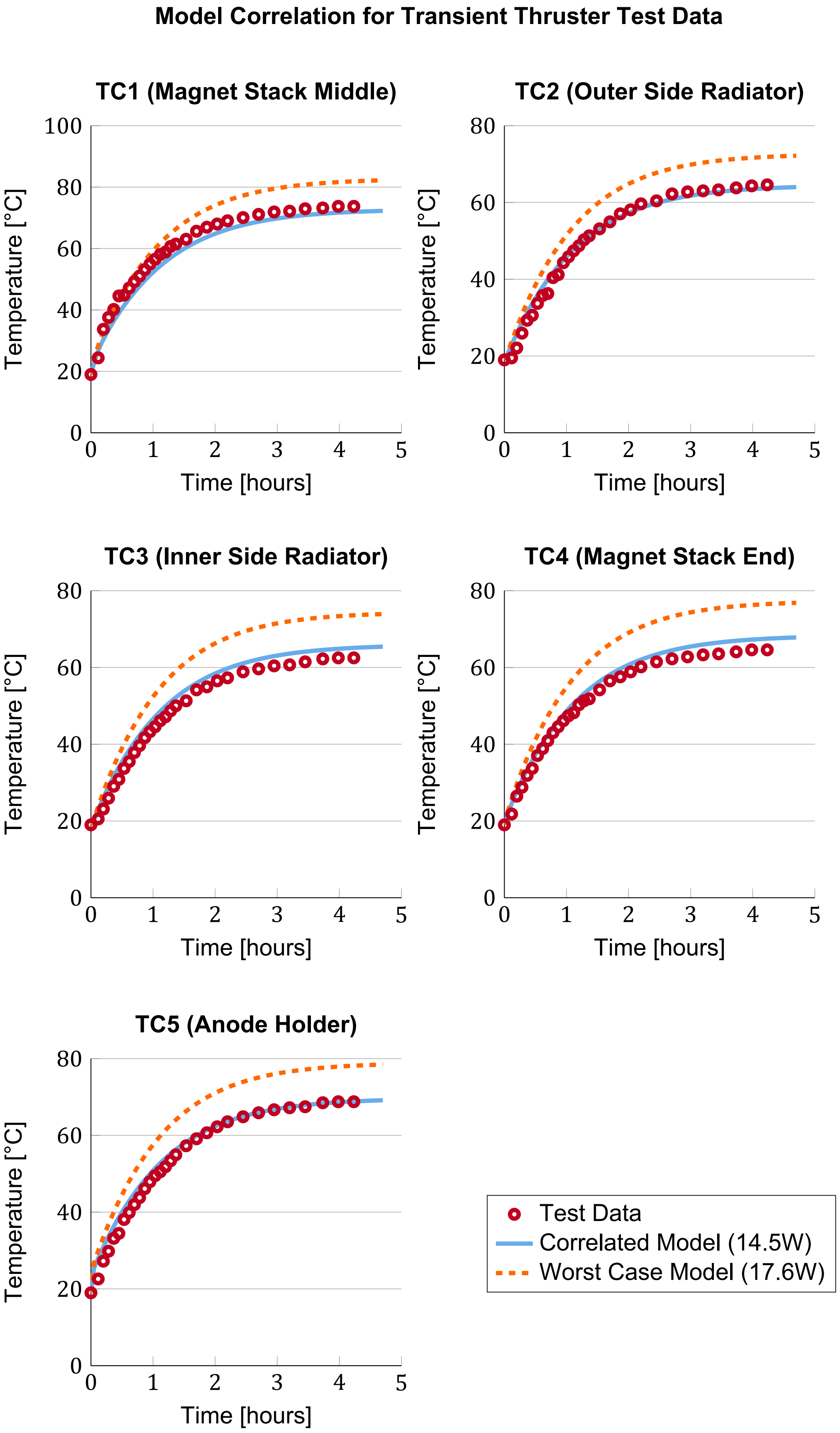

Figure 3.14: Model correlation for transient thruster data at magnet stack. The figure shows the test data, model that best fits the data (14.5 W losses) and model worst case (17.6 W losses).

With this correlation, all uncertainties have finally been eliminated. The model at 14.5 W thermal losses can calculate the steady state that the thruster testing would have reached, should it have continued for enough time. The temperatures at each measurement point during steady state would have been as shown in table 3.25. It is also possible to calculate a worst case, for which the Thermal Model always overestimates the temperature at each location by a maximum of 10°C. The worst case can also be found in figure 3.14 for each location.

Table 3.25: Temperatures at all five measurement locations for three cases: maximum temperature reached by the thruster during testing, model-predicted steady state for the thruster testing and worst case model, for which all temperatures are overestimated

Case	**TC1 [°C]**	**TC2 [°C]**	**TC3 [°C]**	**TC4 [°C]**	**TC5 [°C]**
Test Max. Temp.	73.73	64.59	62.50	64.59	68.77
Model Predicted SS (14.5 W)	72.84	64.52	65.95	68.37	69.68
Worst Case SS (17.6 W)	82.77	72.65	74.42	77.35	78.94

Using the worst case during the thruster simulations in orbit will compensate for any mistakes in the heat capacities. As seen in figure 3.14, and considering a transient point before the steady state is reached, increasing the thermal losses value has a similar effect to decreasing the heat capacities. This is a way to ensure that the model never predicts temperatures that are lower than the ones the thruster would reach in reality.

Finally, the Thermal Model of the mN-µHEMPT has been successfully correlated to the test results (all correlations fulfilled the requisites in terms of deviation and physical consistency). From this validation, two main conclusions can be drawn. The first one, with respect to the thermal losses distribution, is that a difference exists between the Thales HEMPT 3050 system and the Engineering Model, in view of the thermal loss distribution computed in this section. However, this difference is relatively small. The two thrusters have different magnet stack configuration, which affects the plasma and electron distribution inside the chamber. It was anticipated that the thermal losses distribution would be similar and this is what has happened: the HEMPT 3050 loses 50% to the anode and 50% to the magnets, while the loses for the mN-µHEMPT are 40%/60%.

The second conclusion is drawn from the calculated value for the thermal losses. This value of 14.5% of the input power (remember that for 100 W input power, the losses were 14.5 W) is in line with the results published for the HEMPT 3050 (15%) [24], but is in great disagreement with the value calculated in section 3.3 (35%). The reason for this inconsistece lies in the analytical calculation of the thermal losses. Although ionization and excitation losses were considered, the double and multiple ionization was not considered. The HEMPT is known to produce multiple ionization [78], at least up to Xe^{+5} [79].

However, multiple ionization only accounts for a small percentage of the total ions. In addition to this, the recombination process by which ions become neutrals by catching an electron and can become ionised again is not considered either [80]. Another explanation would be that the assumption stating that the beam current is 70% of the anode current could be false, meaning that the beam current is being underestimated. A higher beam current would result in higher beam power and ionization losses, thus reducing the calculated thermal losses.

3.5. Thruster In-Orbit Performance: Results Analysis

The thruster Thermal Model has been successfully validated (all correlations fulfilled the requisites in terms of deviation and physical consistency). Now it can be used to simulate the performance of the mN-µHEMPT in orbit, which is the first objective of the Thermal Model (as stated in the end of section 3.2). The current section will present the preliminary results obtained for the Thermal Model in orbit.

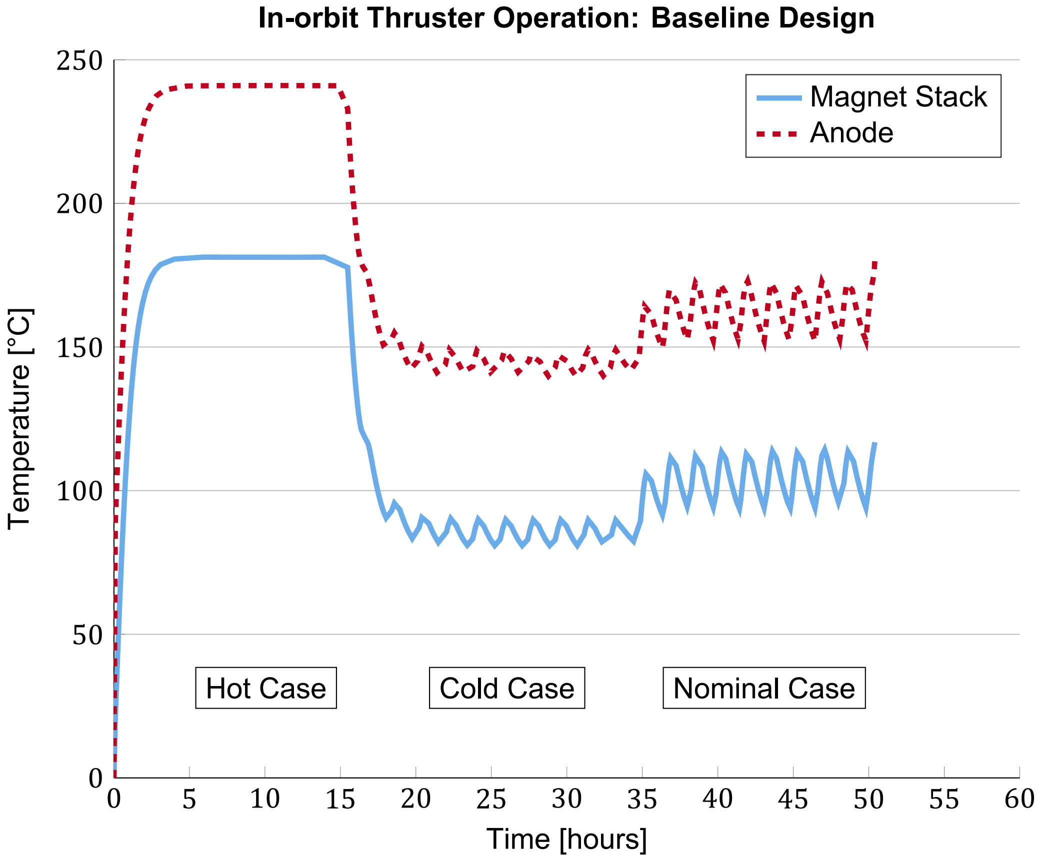

Figure 3.15: Temperature evolution with time of the hottest nodes at anode (node T10001, located in the tip) and magnet stack (node 1050, located in contact with the middle poleshoes). Hot, nominal and cold (all cases with thruster on) load cases. Thermal model of the baseline mN-µHEMPT, each case ran for 10 orbits.

Figure 3.15 shows the hot, nominal and cold load cases (all cases with thruster on) for the Thermal Model of the mN-µHEMPT Engineering Model without any modifications, which is taken as baseline design. The input power for the simulations is 17.6 W of thermal losses: worst case calculated during the model validation. The highest temperatures of anode and magnet stack are plotted, the former because it is the highest of the complete model, the latter because of the strict requirement of 200°C (THR-TC-200). The simulations were ran for 10 orbits in order to achieve a steady state.

As it was anticipated, the temperatures during the hot load case are higher than in the nominal case, which are respectively higher than the cold case. On the hot case, the temperature variation in the steady state is unnoticeable, while the other cases have great variation with time, although always cyclical in the steady state. The cause of these variations is the eclipse. As the hot case considered an orbit without eclipse, there are no visible variations with the orbital period. On the nominal case, the thruster stops receiving Sun radiation during eclipse, resulting in a high temperature difference between sunlight and eclipse (around 20°C). On the cold case, the sunlight never impinges the thruster, as it is always covered by the spacecraft. The difference during eclipse is that the spacecraft also covers the Earth (due to the fact that the thruster always points away from the Sun), so the Earth IR and Albedo radiations do not hit the thruster. The result is that no external heat radiation enters the thruster, so the temperatures reached are the lowest. Regarding the values of the temperatures, the magnet stack stays under its requirement (200ºC). This means that there is a margin for improvement: either the input power can be increased, or the design can be modified to reduce the mass or the envelope volume, until the temperature of the magnet stack reached the limit. This is not advisable, as the effect of temperature on the magnet stack is already noticeable before reaching the allowable temperature.

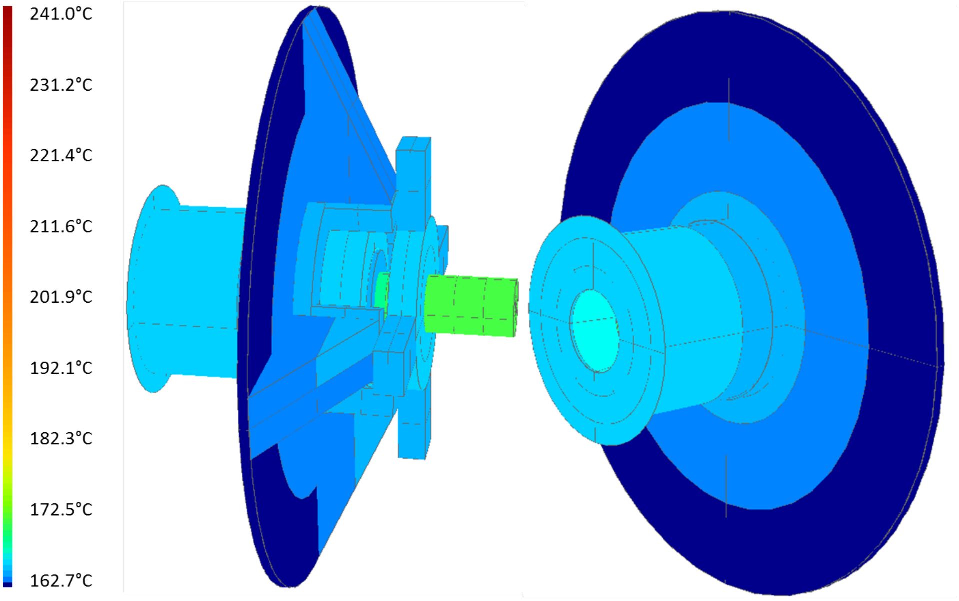

Figure 3.16: Temperature map of the thruster in the steady state of the hot load case

Figure 3.16 shows the temperature distribution for the thruster during the steady state of the hot load case. The purpose of this figure is to illustrate the heat flows in the thruster housing and radiators. The anode holder is the hottest component after the magnet stack and anode, while the outer part of the radiator is the coldest. Due to the high thermal conductivity of aluminium, the temperature gradients in the housing and radiator are small (less than 10ºC). The biggest jumps in temperature are caused by the contact conductivities between the parts.

The coldest case is achieved without firing the thruster. A simulation with the thruster switched off is seen in figure 3.17. In this case, the interesting points are the coldest nodes. The coldest one is located in the outer part of the radiator, and the coldest point of the magnet stack is in the downstream end. In order to appreciate the scale of this case, the hottest node is also included in figure 3.17. The difference in temperature on the complete model is only a couple of degrees (less than 3ºC). It is clear that the thruster thermal losses create higher temperature gradients along the thruster, due to the fact that they are applied only in specific areas. On the contrary, the external radiation impinges the thruster in a greater and more uniform area. As the external fluxes rule the thermal behaviour of the thruster in the cold case, the temperature is more uniform than it was for the cold and nominal cases.

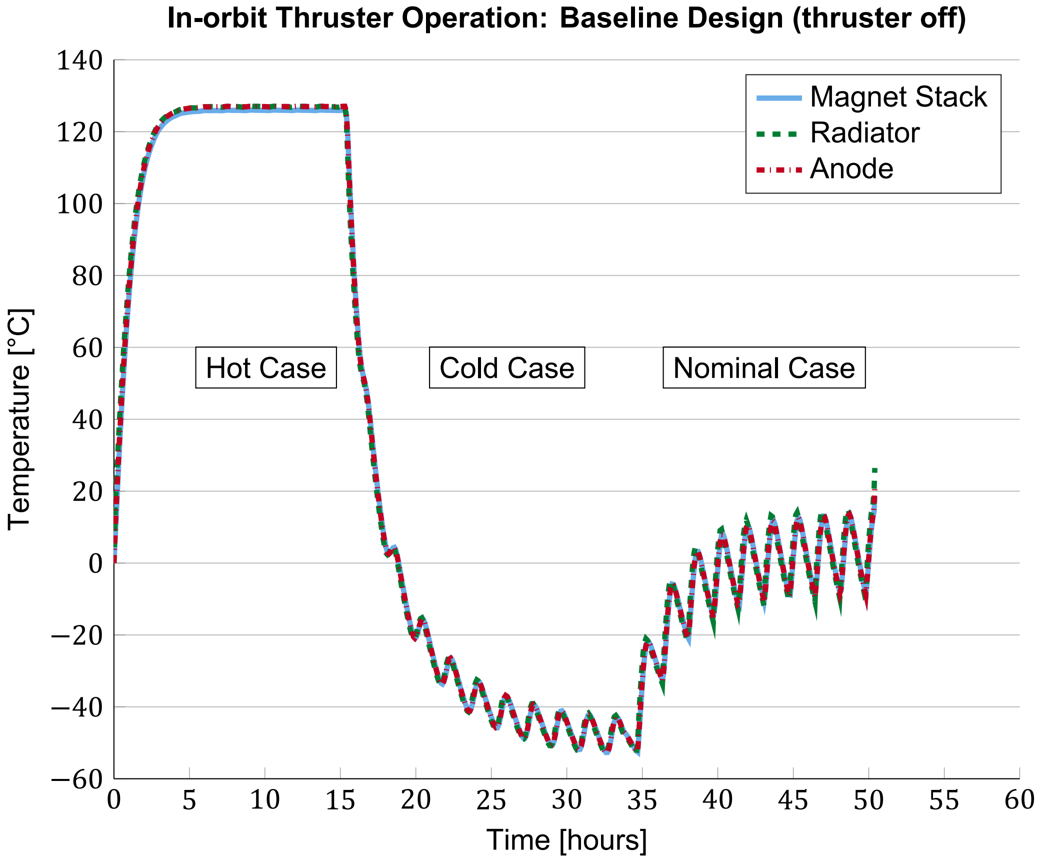

Figure 3.17: Temperature evolution with time of the coldest nodes at magnet stack (node T1132, located in the magnet stack end), radiator (node 4007, located in the outer edge) and the hottest node of the model at the anode (node 10001, located in the tip). Cold, hot (with thruster off) and nominal (with thruster off) load cases. Thermal model of the baseline mN-μHEMPT.

Another point worth mentioning is the important difference in temperature between having the thruster switched on and switched off, which can be seen in figure 3.18. Given the small difference in temperature between nodes with the thruster turned off, the figure shows the hottest points of the magnet stack and anode. The temperature difference is significative, reaching 190°C variation between having the thruster on and off (for the cold case). The reason why the temperature difference is higher in the cold and nominal cases than in the hot case is because on the former cases the thermal losses have a higher contribution to the total heat input to the thruster. In the hot case, the external heat input represents a higher percentage of the total heat input, which is why a variation in the thruster thermal losses has a smaller impact than on the other cases.

In general, extreme changes in temperature of spacecraft components should be limited as much as possible, which is why these results raise concern. Apart from the absolute difference in temperature, the time needed to switch from one temperature to the other should also be analysed. As a rough estimation for the hot-to-cold change, the cool-down data from the thruster test, found in appendix B, can be used. In the last moments of the test, the thruster was switched off, and the decrease in temperature was measured during 27 minutes. In this time, some nodes cooled faster than others, ranging from -42ºC/hour (TC1 in the magnet stack reduced its temperature by -19ºC) to -23ºC/hour (TC2 in the outer radiator reduced its temperature by 10ºC). Considering the magnet stack, and assuming also that the -42ºC/hour

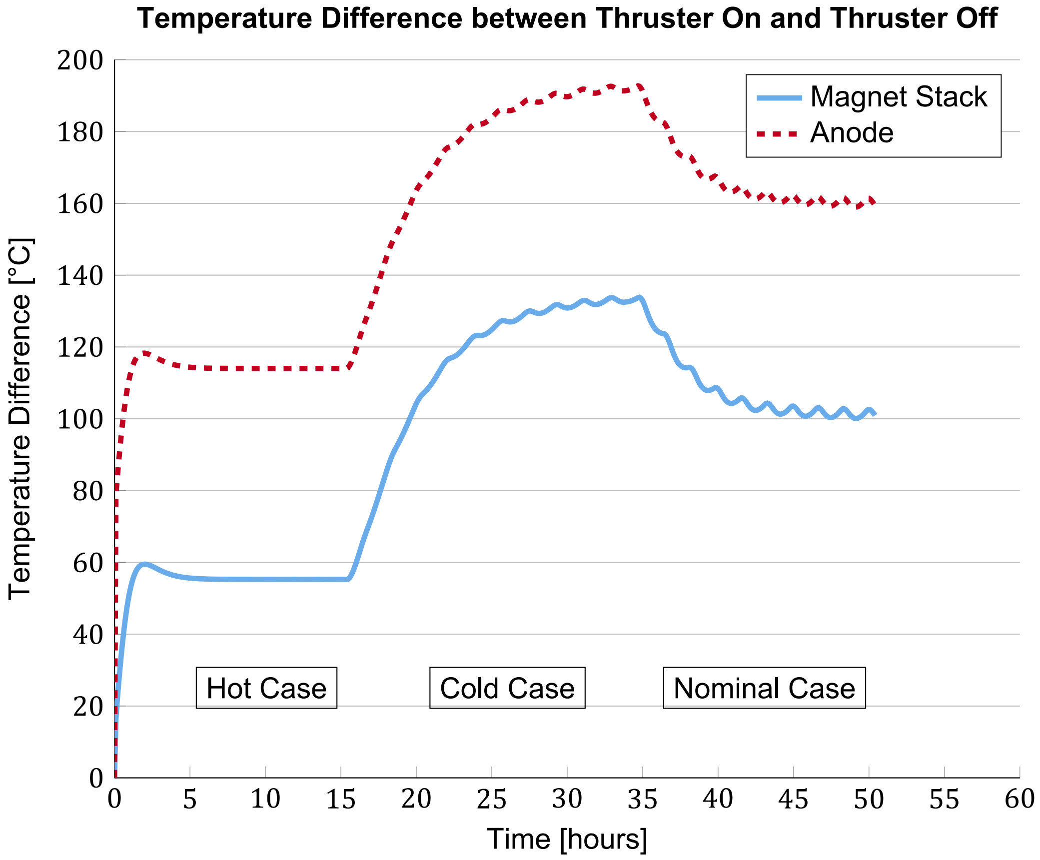

Figure 3.18: Temperature difference between thruster on and off for the hottest nodes at magnet stack (node T1132, located in the magnet stack end) and anode (node 10001, located in the tip). Hot, cold and nominal load cases. Thermal model of the baseline mN-µHEMPT.

rate is maintained constant (in order to have a conservative value), the thruster would need 3.2 hours to change the 135ºC (maximum temperature difference in magnet stack). This means that the extreme temperature changes between thruster on and thruster off would take around 2 orbits.

Regarding the cold-to-hot case, the transient of the thruster test can also be considered, again found in appendix B. For the magnet stack (TC1), the maximum temperature increase rate was +57ºC/hour (25.6ºC in the first 27 minutes). Considering it again as constant to stay on the conservative side, an increase of 135ºC would last 2.4 hours (less than for the hot-to-cold case), which is around 1.5 orbits.

The thruster, used as main propulsion system in small satellites, will most likely have intervals of several orbits without being fired if it is used for orbital manoeuvres, which may be done from once a week to once a month. The previous calculations show that the extreme temperature changes between thruster on and off will possibly take place during operation. In this way, the general variation in temperature between thruster on and off cases should be reduced if possible.

Continuing with the analysis of the results, the effective decoupling between thermal losses at the magnet stack and at the anode can also be noticed from the simulation results. The total heat flux from the anode into the magnet stack amounts for 1.84 W from the 10.56 W that enter the anode (a 60% of the 17.6 W of total thermal losses). This low value of heat flux is due to the successful isolation performed by the boron nitride discharge chamber and the macor ring. The former component has a low absorptivity which reduces the radiative heat exchange with the anode. The latter allows to isolate the magnet stack from part of the anode and the anode holder (which also reaches high temperatures) thanks to its low thermal conductivity.

When focusing on the magnet stack, it is possible to identify an additional problem with the design. Figure 3.19 shows the temperature distribution on the magnet stack for the hot case and the cold case (during eclipse) already on steady state, both cases with the thruster turned on. The maximum and minimum temperatures are indicated on the image, showing a difference of around 17.3°C between them. The reason for this is the low conductivity of the Sm2Co17 as well as the concentration of most thermal losses in the middle of the magnet stack. This temperature gradient is not desirable, especially for high temperatures close to the requirement.

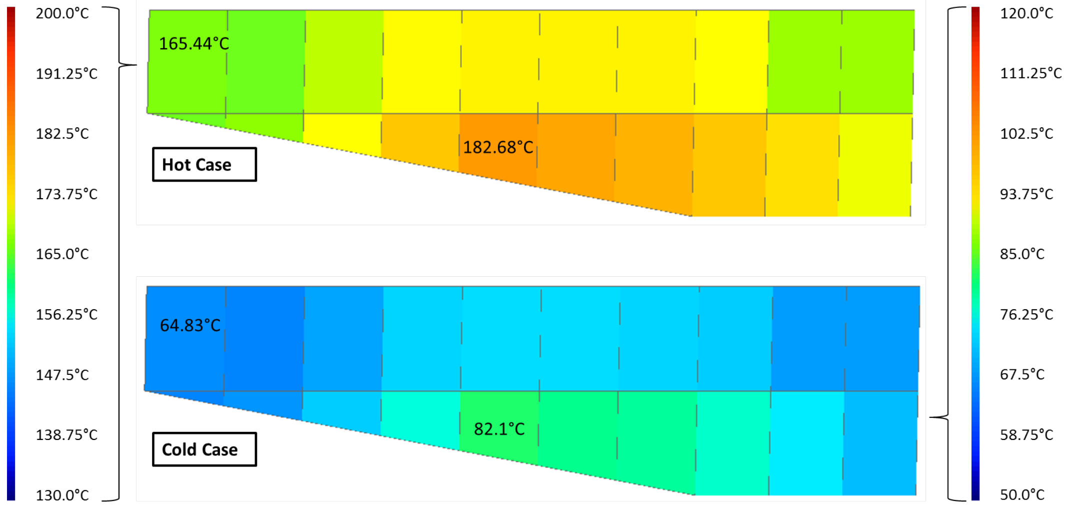

Figure 3.19: Temperature map of the magnet stack during hot and cold cases (cold case in eclipse) for the baseline design. Illustrations show a section view of a dummy magnet stack, where the discharge chamber would be the bottom part, and the anode would be on the bottom-right side. Maximum and minimum temperatures are indicated on the magnet stacks.

The magnetic performance may be slightly affected even below the requirement temperature, and an uneven temperature would result in a magnetic field distortion. The effect can be reversible (below the allowable temperature) or irreversible (over the allowable temperature). The reversible effects are measured by the RTC (Reversible Temperature Coefficient) which considers the change in residual magnetic flux density per degree celsius. When the RTC is zero, temperature changes do not affect the magnetic performance until the allowable temperature. In the case of Sm2Co18, the RTC changes between +0.012 %/ºC to -0.025 %/ºC, depending on the temperature range [46]. These variations can be sufficient to affect the performance of the thruster, and have to be considered when designing an optimal magnet stack. If the temperature is maintained constant throughout the magnets, it is easier to account for the RTC in the magnet stack design, optimising the magnetic field for the operation points. Furthermore, a better distribution of the temperature would automatically reduce the temperature at the hottest locations.

In view of the results of simulating the thruster temperature evolution in orbit for all load cases, a set of conclusions is drawn, collected in table 3.26. These conclusions call for design modifications, in order to improve the thermal performance of the Engineering Model in orbit. The following chapter will deal with this topic, proposing a series of improvements of the thruster and assessing their impact on the temperatures. However, not all the conclusions have the same level of importance. Reducing the temperature in the magnet stack is one of the main objectives, due to the high sensitivity of the magnetic field to the temperature of the magnets.

Table 3.26: Conclusions obtained from first simulation results of the baseline design

nº	Conclusion	Priority
1	Temperature difference between load cases could be reduced	Medium
2	Temperature difference between thruster on/off could be reduced	Low
3	Magnet stack could be better isolated from the heat coming from the anode	High
4	Temperature gradient in the magnet stack could be reduced	Medium

Following in priority, the temperature difference between load cases should be reduced, in order to decrease the dependency of the thruster temperatures on the orbit selected as much as possible. This is in line with the mindset behind the design that aims for a system with defined characteristics and interfaces that can be easily implemented in a spacecraft and a mission. It is also needed for the thruster to have a stable operation point. Changes in the temperature of the magnet stack during thruster firing would lower the performance, as the magnetic field is optimised for a certain temperature.

Regarding the following conclusion, the temperature gradient over the magnet stack directly affects the performance of the thruster, as it influences the generated magnetic field. However, there is little room for improvement, due to the fact that the Sm2Co18 magnets have a low thermal conductivity.

Finally, the difference in temperature between on and off cases has a lower level of importance, as there are no major requirements in the lower limit and it does not have a direct effect on the thruster performance (once the thruster is turned off, the variation in temperature is not as crucial). However, when performing a structural analysis of the system, the lower temperatures should be considered, as well as the thermal cycling, which can lead to structural failure.

Even if further design modifications are required, the thermal model already meets two of its three objectives, stated in section 3.2. The first one (obtain the temperature distribution of the thruster under the load cases) is achieved when simulating the thermal model in the three load cases, as seen in figures 3.15 and 3.17. The second objective (demonstrate thermal feasibility of in-orbit thruster operation) is also reached, as all the elements stay under their allowable temperatures. This includes the magnet stack in the hot load case. Even if the thruster can already be operated in orbit, its performance can be optimized. The third objective, concerning the reduction of the temperature at the magnet stack, will be dealt with in the following chapter.

4

Design Modifications

After analysing the first results of the thruster performance in orbit, it has become clear that the baseline design has several points of improvement. The aim of this chapter is to present the design modifications that tackle the identified deficiencies and show the improvement in thermal performance. The process followed in order to develop the new design starts with analysing the conclusions obtained from the simulation of the baseline design, defining a set of objectives to be met by the design changes. A set of modifications and solutions is proposed, targeting each critical point identified. These solutions are assessed in order to ponder their feasibility and advantages in comparison to the baseline design.

In order to assess the design modifications, two types of implementation are followed: directly on the baseline and through a design case. The changes implemented on the baseline are three: change of the radiator optical properties by applying a boron nitride coating, removal of the heat pipes and creation of a conductive interface directly between the radiator and the magnet stack. Regarding the design cases, three different ones are assessed: the Design Case 1 involves removing the radiator, the Design Case 2 consists in the modification of the existing radiator (in terms of geometry and orientation) and finally the Design Case 3 considers the addition of an extra radiator attached to the anode holder.

4.1. Objectives and Proposed Design Modifications

Even if the results of simulating the baseline design demonstrated its feasibility to operate in orbit, several conclusions were drawn, resulting in improvement points and design considerations to bear in mind. These conclusions were described in table 3.26 in the previous chapter, and are related to the thermal performance of the system. Apart from these, the general objectives of the Thermal Model can be recalled, in particular the last one (reduction of the maximum temperature at the magnet stack) and the secondary ones (mass reduction, volume envelope reduction and design simplicity). From the combination of all the aforementioned conclusions and goals, a set of objectives of the design modifications is elaborated, and can be seen in table 4.1.

Table 4.1: Conclusions obtained from initial thermal model simulations and proposed design modifications

nº	Objectives of the Design Modifications	Origin of the Objective
1	Reduce the temperature difference between load cases	Conclusion from Baseline simulation
2	Reduce the temperature difference between thruster on and off	Conclusion from Baseline simulation
3	Reduce the heating of the magnet stack due to the anode	Conclusion from Baseline simulation
4	Reduce the spatial temperature gradient in the magnet stack	Conclusion from Baseline simulation
5	Reduce the external heat flux into the thruster	Conclusion from Baseline simulation
6	Reduce the maximum temperature of the magnet stack	Primary objective of the Thermal Model
7	Simplify the design	Secondary objective of the Thermal Model
8	Reduce the mass	Secondary objective of the Thermal Model
9	Reduce the volume envelope	Secondary objective of the Thermal Model

In order to target all of these objectives, six design solutions were visualized, and can be seen in table 4.2. All of these design solutions were thought of by analyzing the thermal behaviour of the thruster, which is why only a small set of tailored design modifications was elaborated. Moreover, and given the fact that an Engineering Model with the baseline design already exists, the implementation is done directly on the baseline when possible. When the design change is significative, a design case is created. The design cases are variations of the baseline that try to proof the effectiveness of a design modification. They are not optimized, but are representative of the impact of the modification on the thermal performance of the thruster.

Table 4.2: Proposed design modifications targeting the different objectives found in table 4.1 and model of implementation

Design Modification	Objectives	Implementation
Change radiator coating	1, 2, 5, 6	Changes to Baseline
Remove heat pipes	7	Changes to Baseline
Conductive coupling radiator-magnets	4, 6	Changes to Baseline
Replace external radiator with body-mounted	8, 9	Design Case 1
Change radiator orientation/shape	1, 5, 6	Design Case 2
Decouple thermal losses anode-magnets	3, 6	Design Case 3

Changing the radiator coating is motivated by the elevated external heat load entering the thruster through this surface. When considering the hot case, a radiator requires a high emissivity in order to evacuate as much heat as possible. But when the radiator receives external heat fluxes (e.g. solar radiation), it should have a low absorptivity, so that the α/ε ratio is low and as little heat as possible is absorbed. Black Kapton tape has a high absorptivity, which was not an issue in the vacuum testing, but it would be in mission scenarios on which the radiator points towards the Sun. However, when considering the cold case, a radiator with a low α/ε ratio would reach very low temperatures. There is a trade-off to be done when choosing the radiator optical properties. In the case of the mN-μHEMPT, reducing the temperature of the magnet stack has a higher priority than increasing the temperature of the cold case, or reducing the difference between thruster on and off. This consideration will be taken into account when making a decision on this design modification.

As far as the heat pipes are concerned, they add an extra point of failure to the thruster. As it has been seen that the anode is far below its allowable temperature, it is interesting to reassess the need for these elements. A trade-off is done between the complexity and added risk of the heat pipes and its improvement of the thermal performance.

The last baseline modification that is investigated is the creation of a conductive coupling between the radiator and the magnet stack. In the baseline design, only the front housing and the magnet press had a contact interface with the magnets. Simulating this design modification will shed light on its effectiveness at reducing the temperature gradient along the magnet stack.

All three aforementioned modifications have a straightforward implementation. The three remaining ones involve greater changes of geometry, mainly involving the radiator. Given that the radiator plays the most crucial role in the thermal control of the thruster, its performance is investigated in detail.

On the Design Case 1, the radiator is removed, and changed for a body-mounted one, taking advantage of the housing, which cannot be removed. This changes completely the response to the different load cases, as the radiative area is oriented perpendicularly to the baseline's radiator. The Design Case 2 modifies the geometry of the radiator, with the idea of finding a better performing solution by inclining it forwards and backwards. Lastly, the Design Case 3 adds an extra radiator, attached to the anode holder, which dissipates the thermal losses at the anode. In this way, the magnet stack is thermally decoupled from the anode.

4.2. Changes to the Baseline Design

Boron Nitride as Radiator Coating

To begin with, and as explained in section 4.1, a change in the radiator coating is the obvious design modification, given that the black Kapton tape in the baseline design has a very high absorptivity (0.93). In the vacuum chamber and for testing, this is not an issue, as without any external source of radiation the important variable is the emissivity (0.85). When simulating the thruster in orbit, the high absorptivity of the radiator together with the big area cause the thruster to absorb a considerable amount of incoming heat. As explained in section 4.1, the most important objective in this case is to reduce the temperature of the magnet stack. For this reason, coatings with a low α/ε ratio, such as, for example, white paint, are considered. The impact on the cold case temperatures and the difference between thruster on and off will also be assessed and quantified, as a white coating will have a negative effect on these aspects. Table 4.3 shows commonly used coatings with a low α/ε ratio.

Boron nitride is a ceramic normally used for its electrical insulation properties (such as in the discharge chamber of the mN-μHEMPT), high thermal conductivity and thermal stability. However, it also counts with a very low α/ε ratio. In the literature, the material is said to have around 0.9 emissivity [59] and 0.1 absorptivity [60], resulting in a α/ε ratio of 0.111, similar to the teflon with silver backing coating (commonly used in space radiators). Ceramic white coatings have already been tested in space (e.g. AZW/LA-II on EO-1 mission [81]), although boron nitride has not yet been tried. It is however starting to be considered for missions such as Parker Solar Probe [82].

Table 4.3: Compilation of common space-application coatings with a low α/ε ratio [61]. Boron Nitride*: not yet space-application status.

Coating	α/ε
Barium Sulfate with Polyvinyl Alcohol	0.068
Boron Nitride*	0.114
GSFC White Paint MS74	0.185
OSR	0.075
Helios Second Surface Mirror/Silver Backing	0.088
Teflon with Silver Backing	0.102
Zinc Orthotitanate with Postassium Silicate	0.141

Given the availability of boron nitride in the LET laboratory, an optical properties test was prepared to assess its suitability for thruster testing. Notice that, at the moment, a boron nitride coating could not be used on a flight model, because it is not space-qualified. But as the optical properties are similar to other common radiator coatings and it outperforms normal white paint, it could be an affordable replacement for model testing. The testing was successful, and the best α/ε obtained was 0.114 (as shown in table 4.3), for emissivity and absorptivity values of 0.8291 and 0.0944, respectively. The complete test procedure and results can be found in the appendix D.

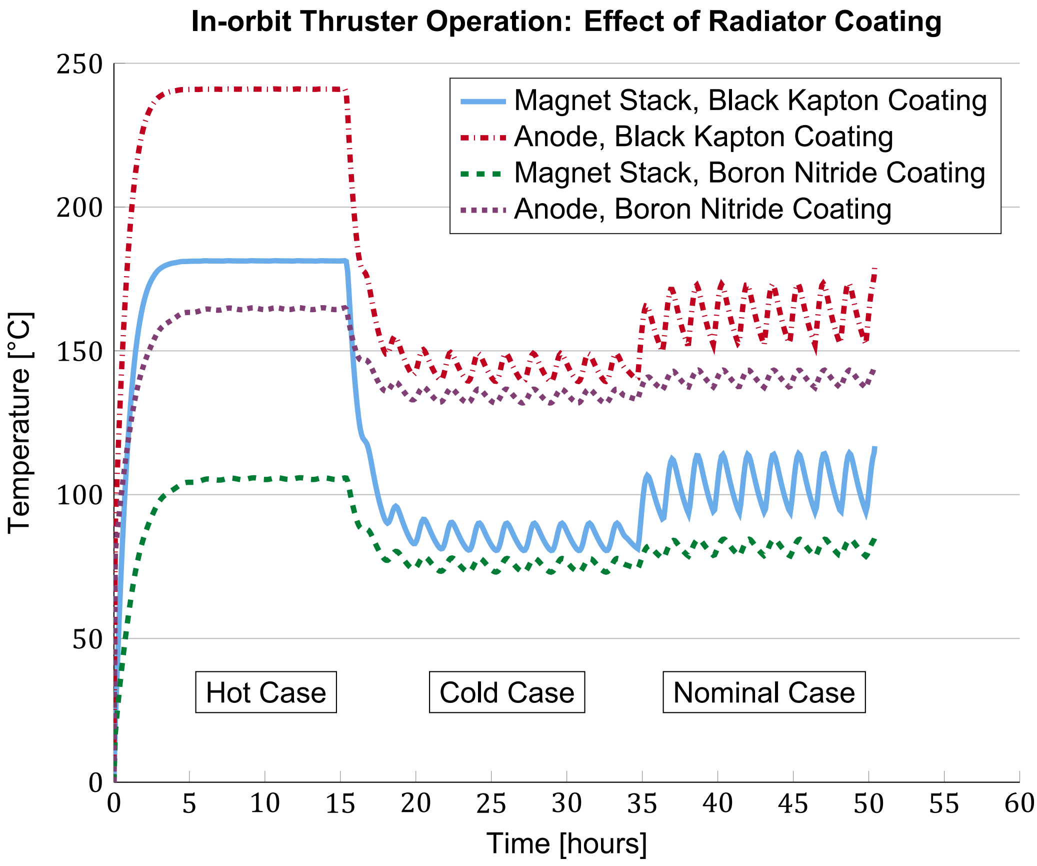

Figure 4.1: Temperature evolution for the baseline design, first with black Kapton tape and then with boron nitride coating at the radiator surface during the hot, nominal and cold orbits, with the thruster on. The locations of the temperatures are the hottest node in the anode and the hottest node in the magnet stack.

Figure 4.1 shows the effect of this change on the maximum temperatures reached by anode and magnet stack with the thruster on. As it can be seen, the change in temperature is around 80ºC for the hot case, 10ºC for the cold case and between 20ºC and 30ºC for the nominal case. This is a significant improvement, as it decreases the maximum temperatures and reduces the difference between the load cases (which changes from almost 100ºC to barely 30ºC).

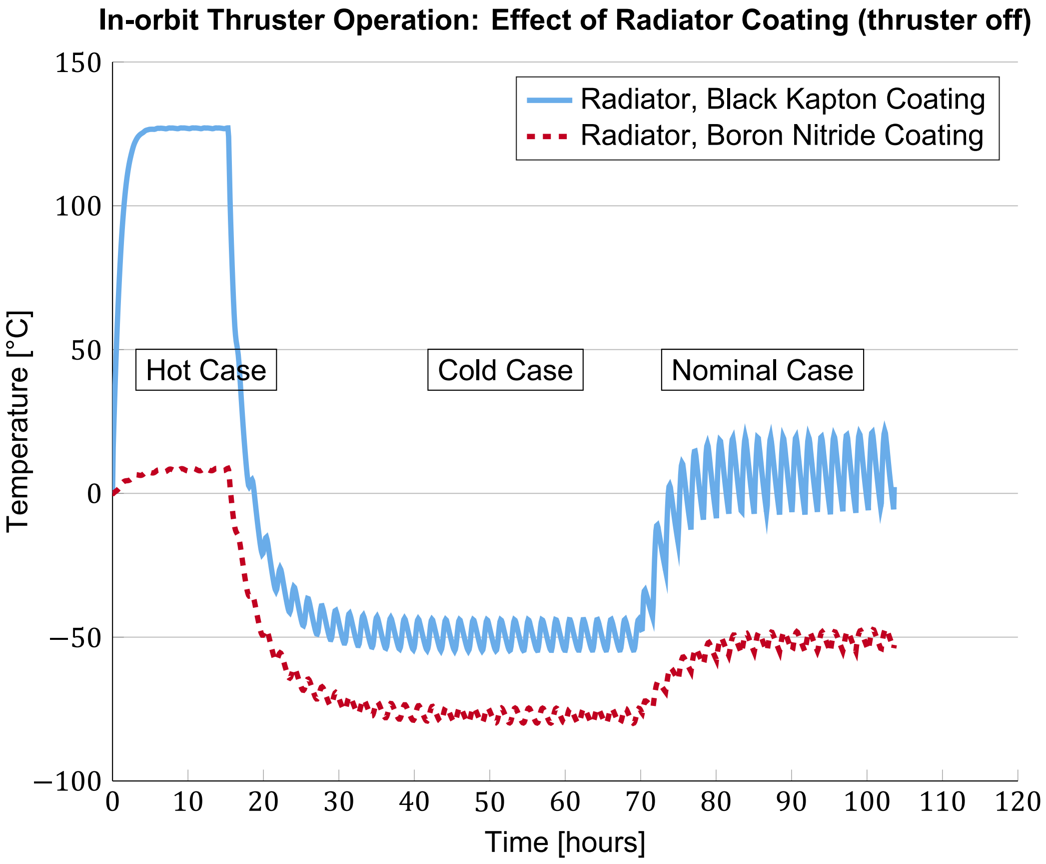

Figure 4.2: Temperature evolution for the baseline design, first with black Kapton tape and then with boron nitride coating at the radiator surface during the hot, nominal and cold orbits, with the thruster off. The location of the temperature is the outer edge of the radiator.

After analysing the temperature evolution with the thruster on, figure 4.2 shows the coldest node in the thermal model during the load cases with the thruster turned off. As the temperature variation between the coldest and hottest nodes of the model is less than 2°C, it can be assumed that all components are at the same temperature. The plot is done for a node at the radiator, representative of the temperature at any point in the thruster. The reduction in temperature is considerable: 120°C on the hot case, 25°C on the cold case and 50-70°C on the nominal case. In total, the difference in temperature between thruster on and thruster off is increased. For the hot case, the anode temperature changes from 114°C to 155ºC, and the magnet stack temperature changes from 55°C to 97°C. For the cold case, the change is from 190°C to 216ºC at the anode and from 131°C to 157°C at the magnet stack.

The results obtained are not entirely advantageous: there is a great improvement in the magnet stack temperature, the heat flux into the thruster is reduced and the difference in temperature between load cases decreases, but the temperatures with the thruster turned off decrease, and the difference between thruster on and off increases. These effects had been expected, and a trade-off is necessary. In order to support the decision on this design modification, table 4.5 assesses the change in performance with respect to the objectives previously defined. This decision table is straightforward: ”+” indicates an improvement, ”0” indicates no change and ”-” indicates a decrease in performance. The final conclusion is done taking into account the total sum of pluses and minuses, as well as the objectives for which the performance improves or becomes worse. It is clear from this table that the advantages outweigh the disadvantages.

In this sense, it is concluded that an implementation in the baseline design would be beneficial. The boron nitride coating is decided to be implemented in the baseline thermal model in order to gain expertise on the use of this coating for thruster testing. However, due to the negative effects on the cold case temperatures, it is recommended that another design iteration should take place before a final coating is chosen. In this iteration, a structural analysis and testing process should take place, analysing the impact of cold temperatures and thermal cycling on the structural components of the thruster, in case a coating with a higher α/ε is preferred, having a better combination of advantages and disadvantages.

The following analyses will already include this design modification as if boron nitride coating was part of the baseline design. Normally every design modification would be compared to the same initial baseline. But the change in temperature due to the boron nitride coating is substantial: the impact of the design modifications on the thermal performance is different for the black Kapton and the boron nitride baselines. Given that the implementation of this new coating on the baseline design is likely to take place (as mentioned before, to gain expertise on the use of this coating in thruster testing), it is decided to compare all other design modifications to this updated baseline design.

Table 4.4: Decision table for boron nitride radiator coating

Objectives:	**1**	**2**	**3**	**4**	**5**	**6**	**7**	**8**	**9**	**Conclusion**
Boron Nitride Coating	++	-	0	0	++	++	0	0	0	Implement on baseline

Removing the Heat Pipes

A further design modification is the removal of the heat pipes. Its performance has not yet been computed, and even if removing them would hinder the overall thruster temperature, it is interesting to assess the impact of this change on the magnet stack. Avoiding the use of heat pipes would be beneficial in terms of simplicity of design, as they are a possible failure point.

When removing the heat pipes, the heat from the anode holder is evacuated mostly through radiation, as the presence of the macor ring limits the heat conduction into the magnet press. Given the small size of the anode holder, it is expected to require a high temperature to emit all the heat.

Figure 4.3 shows the temperatures at the anode and magnet stack for the baseline with and without the heat pipes, with the thruster on. Notice that the baseline has already been updated with the boron nitride coating, as it was mentioned earlier when discussing that design modification. The little effectiveness of the heat pipes is visible. While its impact on the anode temperature is considerable, the magnet stack almost does not suffer any change in temperature. Given that the anode can withstand high temperatures and that the critical point is the magnet stack, the removal of the heat pipes would be justified in the light of these results.

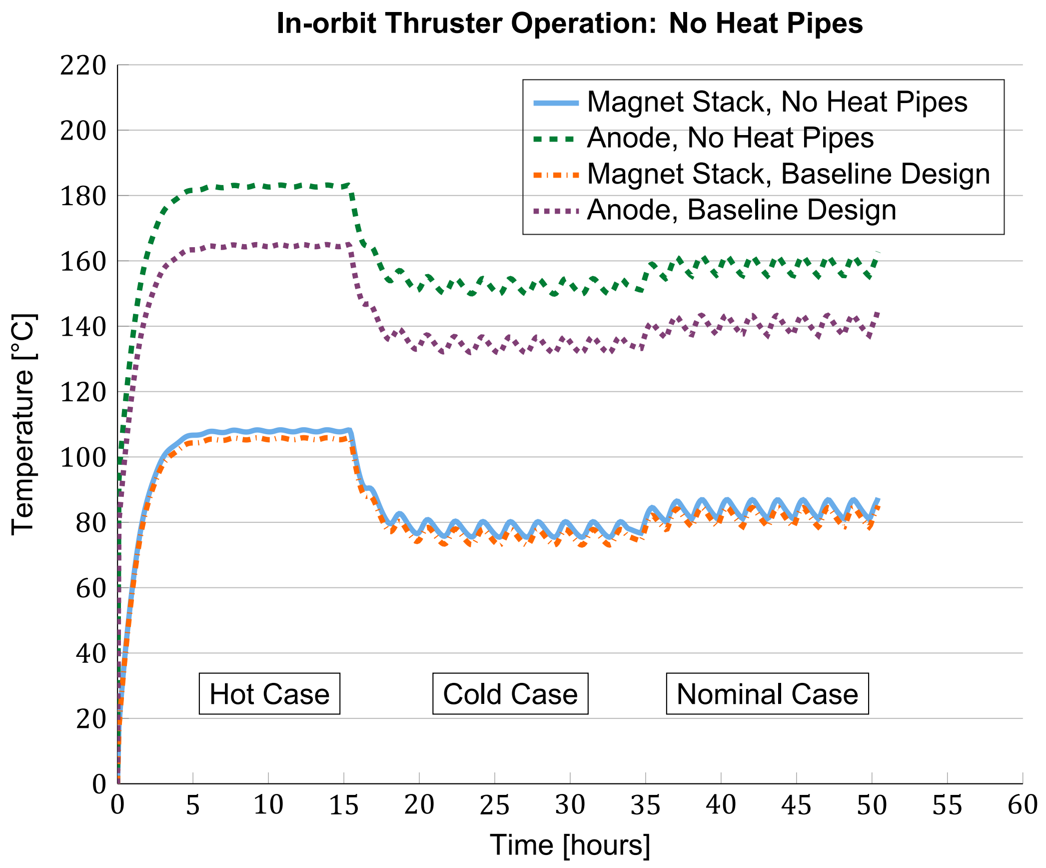

Figure 4.3: Temperature evolution for the baseline design with and without heat pipes, both at the anode and the magnet stack, for all three design cases, with the thruster on

Regarding the performance of the system with the thruster turned off, the difference made by removing the heat pipes or not is negligible, falling within the model error. This design modification does not affect the absorbed external heat fluxes, which rule the overall temperature of the thruster. Conduction is less crucial in the cold case, as the heat enters the thruster through a large distributed area.

Table 4.5 shows the decision table for this design modification. The advantage in simplicity is considerable, and the decrease in thermal performance is minimal. Given that they are already installed on the Engineering Model, they will be removed on the next design iteration. However, in order to reduce the temperature of the anode and avoid high thermal gradients as much as possible, other solutions will be investigated, such as dissipating the heat of the anode through conduction via the structure and into the radiator. This will also be analysed in the design cases, with modification to the mount (part 8).

Table 4.5: Decision table for heat pipes removal

Objectives:	**1**	**2**	**3**	**4**	**5**	**6**	**7**	**8**	**9**	**Conclusion**
No Heat Pipes	0	-	-	0	0	-	++	0	0	Implement on next design iteration

Conductive Coupling between Radiator and Magnets

In the baseline design, the magnet stack is hold together by the front radiator, the front housing and the magnet press. The main radiator is joined to these two latter elements, but not to the magnet stack. In order to improve the extraction of heat from the magnet stack and reduce the temperature gradient through this element, the radiator is modified and attached to the magnet stack. The contact area is similar to the ones in the housing and magnet press interfaces with the magnet stack, and the contact conductivity selected is 10,000.0 W/K/m^2 (same as in the housing-magnets and magnet press-magnets interfaces).

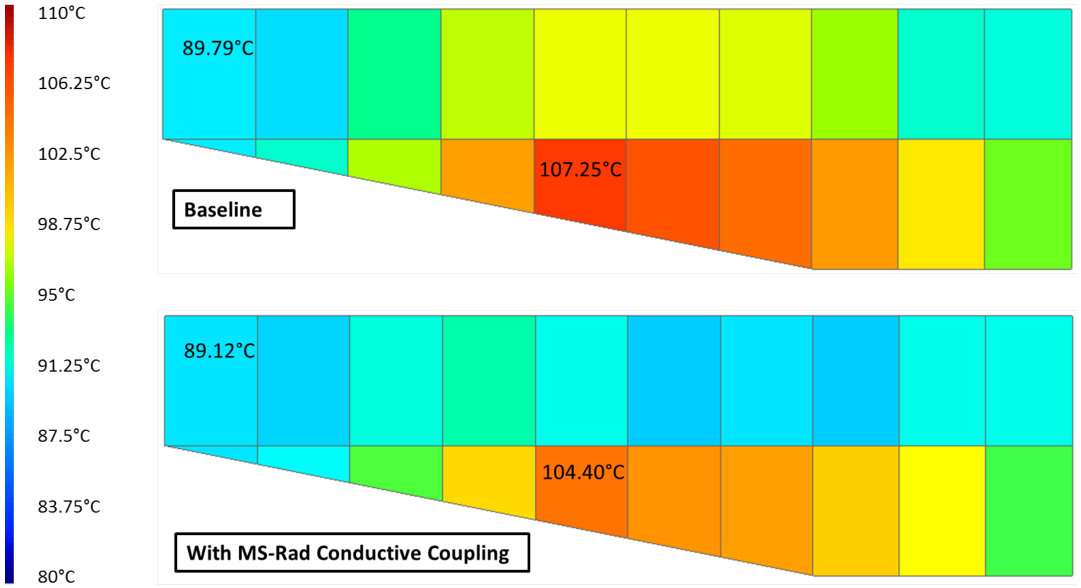

Figure 4.4: Temperature map of the magnet stack during hot case for the baseline design with and without radiator-magnets conductive coupling. Illustrations show a section view of a dummy magnet stack, where the discharge chamber would be the bottom part, and the anode would be on the bottom-right side. Maximum and minimum temperatures are indicated on the magnet stacks.

Although the decrease in temperature was in the order of magnitude of the model error (around 3°C), this improvement is directly transformed into a decrease in the magnet stack temperature gradient. Figure 4.4 shows the temperature distribution along the magnet stack during the hot case, and figure 4.5 shows the results for the cold orbit (with the thruster on). Both figures compare the temperature gradient for the baseline with and without conduction between magnet stack and radiator. The baseline already implements the boron nitride modification.

The decrease in the temperature gradient is a 12.5% for the hot case and a 13.5% for the cold case. This however, in absolute temperature, is passing from a gradient of 17.46°C to 15.28°C and from 17.16°C to 14.85°C, respectively for each case. This is a small improvement which does not justify the manufacturing of a new radiator, but could be implemented if the radiator required further design modifications. It is clear that if the temperature gradient needs to be further reduced, a new design solution should be elaborated, tackling this problem in a different manner. One option could be to attach cobalt rings to the steel poleshoes. Cobalt has a high conductivity and could help to better distribute the heat in the magnet stack.

Table 4.6 is the decision table elaborated for this design modification. This design solution shows only improvements with respect to the baseline. However, these improvements are

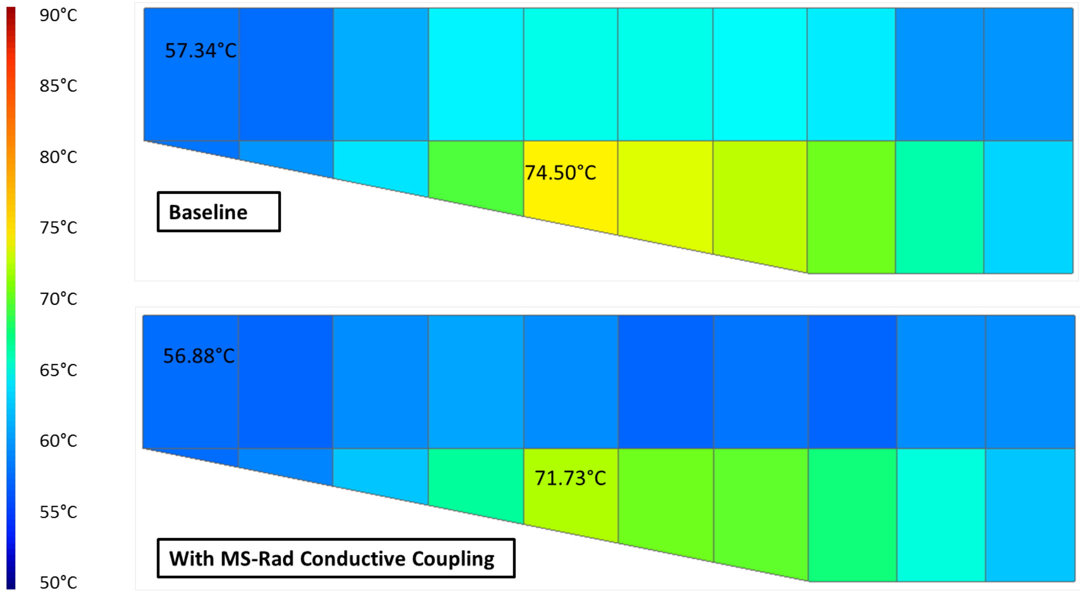

Figure 4.5: Temperature map of the magnet stack during cold case (thruster on) for the baseline design with and without radiator-magnets conductive coupling. Illustrations show a section view of a dummy magnet stack, where the discharge chamber would be the bottom part, and the anode would be on the bottom-right side. Maximum and minimum temperatures are indicated on the magnet stacks.

small (13% decrease in temperature gradient at the magnet stack and around 3°C decrease in the magnet stack temperature). This is why the design modification is not seen as urgent, and can be implemented in the next design iteration, should the radiator be replaced.

Table 4.6: Decision table for magnet stack - radiator conductive coupling

Objectives:	**1**	**2**	**3**	**4**	**5**	**6**	**7**	**8**	**9**	**Conclusion**
MS-Rad Conduction	0	0	0	+	0	+	0	0	0	Implement on next design iteration

As it was discussed, for the following analyses of the design cases, only the boron nitride coating is applied to the baseline. The conductive coupling between magnets and radiator, as well as the removal of the heat pipes is not yet implemented into the baseline.

4.3. Design Cases

Description of the Design Modifications

As it was mentioned before, the three design changes will implement different design modifications, mainly concerning the radiator. On the first one, the radiator is removed. On the second one, the shape and orientation of the radiator is modified. Finally, on the third one, a second radiator is added and attached to the anode holder.

The Engineering Model was seen to perform within the requirements when simulated in orbit. From this working design, only small changes have to be done, with the idea of optimising the thermal performance of the thruster. Each one of the three design cases serves a purpose in this sense. Design Case 1 aims to reduce the mass and volume envelope of the thruster. Design Case 2 has the purpose of reducing the temperature difference between the load cases, as well as lowering the maximum temperature of the magnet stack and external heat flux into the thruster. Design Case 3 intends to reduce the heating of the magnet stack caused by the anode and at the same time lower the magnet stack temperature. All design cases are modifications to the baseline design, trying to reuse as many components as possible, in order to make the implementation easier.

The process followed to obtain the design cases involved several iterations, analysing the impact of the changes on the magnet stack temperatures. The design cases have not been optimized: the objective was that each case had a representative value of the design modifications, meaning that they can be used to analyse the impact on thermal performance. This is only a first step towards improving the Engineering Model by assessing the advantages of certain design modifications, but a further structural analysis and design iteration would be necessary before making any of the proposed changes to the baseline design. All design cases here presented are the final iteration, while appendix E includes previous design iterations and further justification of the design selection.

Regarding Design Case 1, the principal modification is the removal of the radiator. The housing and magnet press are extended, covering the space left by the radiator. After several iterations, it was found that making the outside of the thruster inclined had its advantages: increasing the radiative area, less heat flow into the spacecraft and good performance in all three load cases analysed. In the end, the housing becomes a body-mounted radiator, and is also coated with boron nitride. Furthermore, the mount is modified: in order to have heat conduction from the anode to the housing, a new component similar to the magnet press is attached at the back of the thruster, connecting the anode and the rest of the housing, and leaving the macor ring in between to avoid heat conduction into the magnets. In order to fit this mount, the anode is extended in length. Having the heat flow go directly from the anode into the aluminium mount (and avoiding the anode holder) results in a better heat transfer, as it is hard to tightly attach a component to the boron nitride anode holder. Figure 4.6 shows the Design Case 1 as modelled in Systema. Refer to appendix E for further details on the iterations followed in order to reach this design case.

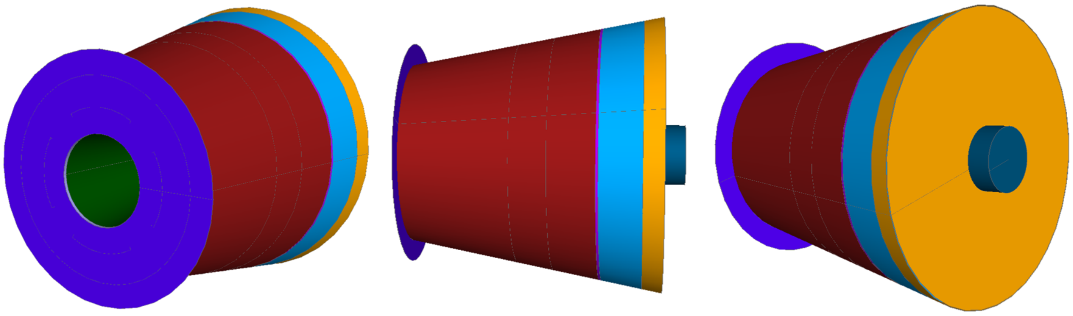

Figure 4.6: Front, side and back view of the Design Case 1: no radiator. The visible parts are the front radiator (purple), front housing (dark red), magnet press (light blue), modified mount (yellow) and anode holder (dark blue). The exit of the discharge chamber is always on the left.

With this design, the envelope volume is reduced from 0.2 m diameter to 0.09 m. Having a smaller size makes it easier to be incorporated in the spacecraft design. As the radiative surface points in the direction perpendicular to the discharge chamber, the temperature difference between each load case will be reduced. This is because the new radiative surface will not receive as much solar radiation in the hot case as the baseline radiator did. The mass of the Design Case 1 is 1.41 kg, a 10% reduction with respect to the 1.55 kg of the baseline design.

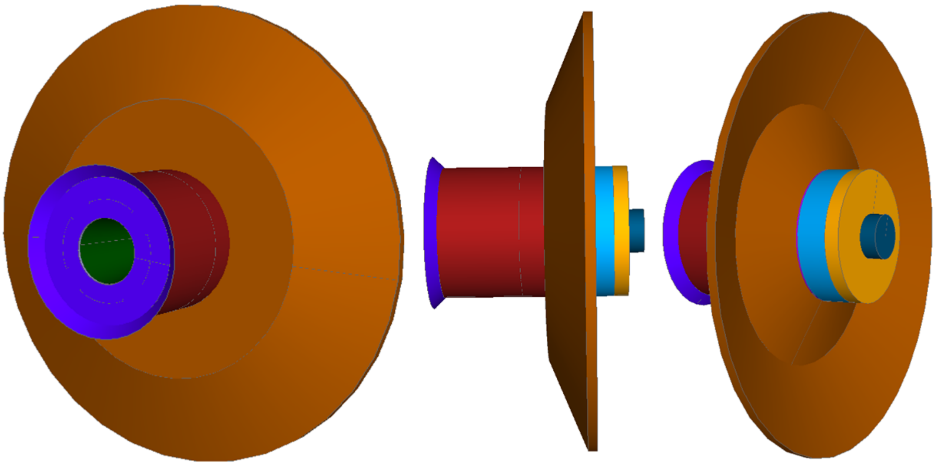

Figure 4.7: Front, side and back view of the Design Case 2: modified radiator. The exit of the discharge chamber is always on the left. The radiating surface of the radiator (i.e. the one coated with boron nitride) is the one pointing in the same direction as the discharge chamber.

Figure 4.7 illustrates the Design Case 2, in which the radiator is modified. As in the previous design, the mount is modified and transformed into a heat path for the thermal losses at the anode into the magnet press and then the radiator. In this way, the heat pipes are not necessary anymore. The shape of the radiator was changed, assessing the performance of different cases, such as inclining it backwards or forward. In the end, a backward-inclination of the outer part of the radiator was found to perform well overall, i.e. considering all three load cases. Appendix E shows the results for different radiator shapes that were considered during the iterative process to define the Design Case 2. The mass of this design case is 1.52 kg, still under the baseline design mass. The purpose of this design was to analyse the impact of the radiator inclination on the magnet stack temperature. It was found that the flat design of the baseline had a good performance, and little improvement could be achieved by modifying the shape, although this will be analysed later in the chapter.

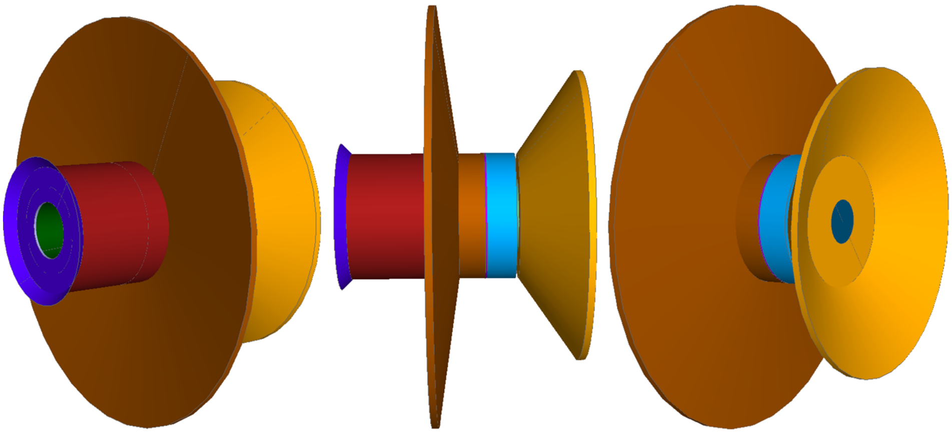

Figure 4.8: Front, side and back view of the Design Case 3: two radiators. The exit of the discharge chamber is always on the left. The radiating surfaces of the radiators (i.e. the one coated with boron nitride) are the ones pointing in the same direction as the discharge chamber. For the first radiator (orange), it is the concave side, while for the second radiator (yellow), this is the convex side. The spacecraft side panel would be located behind the second radiator.

Finally, the Design Case 3 can be found in figure 4.8. With the objective of completely decoupling the thermal losses at the anode from the ones at the magnet stack, two radiators are used. On the one hand, the magnet stack radiator maintains a shape similar to the baseline design (only slightly inclined forward). On the other hand, the mount, which had already been modified in the previous designs, is changed again. This time, instead of being attached to an extension of the anode and connected to the magnet press, it is attached to the anode holder, and added a radiative surface. This surface is inclined backwards in order to increase the view factor into space, as the magnet stack radiator already limits its field of vision. In terms of mass, the Design Case 3 counts with 1.54 kg (ten grams lighter than the baseline design).

The inclination of both radiators was optimized, not in value, but in arrangement. It was found that a forward-backward pair achieved the best performance. Moreover, making the magnet stack radiator larger than the anode radiator was beneficial for the overall temperature. The first radiator shields the sunlight during the hot case (Sun pointing). The iterations followed in order to arrive to the Design Case 3 are presented in appendix E. Notice that during nominal cases on which the anode radiator receives direct sunlight in the front side (boron nitride), the magnet stack radiator receives the radiation through its back side (aluminium). The low absorptivity of aluminium is ideal for protecting the radiators against undesired radiation. Figure 4.9 shows schematically the shape of the inner and front radiators, and also indicates the locations of the radiative surfaces. The figure also indicates the location of the spacecraft panel wall.

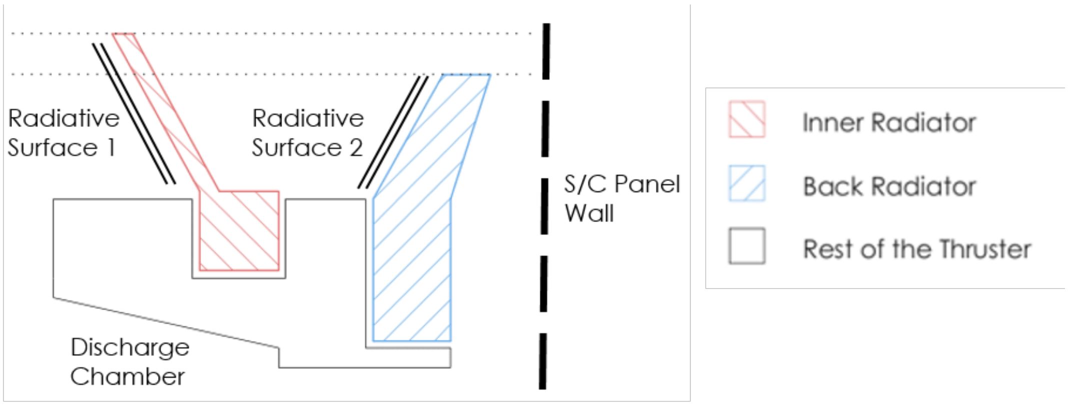

Figure 4.9: Illustration showing the inner and back radiators of the Design Case 3 and an indication of the radiative surfaces and the s/c panel wall

Thermal Performance of the Design Cases

All three design cases have been described. At this point, the thermal performance of each one can be assessed. The first thing to analyse is the in-orbit performance with the thruster switched on (hot and nominal cases), observing the maximum temperatures reached and the difference between load cases. Afterwards, the simulations with the thruster turned off are analysed, observing the lowest temperatures reached during the cold case as well as the temperature difference between thruster on and thruster off cases.

Figure 4.10 shows the maximum temperature at the magnet stack for all design cases as well as the baseline, while figure 4.11 is the equivalent graph elaborated for the anode. It is clear that the Design Case 3 (two radiators) outperforms the baseline, while all other designs perform similar or worse. The temperature evolution for the two radiators is similar to the baseline in shape, with a 30°C difference between hot and cold case. The improvement in temperature is higher at the magnet stack than at the anode, which shows that two radiators is an effective solution for lowering both the temperature of the magnet stack and the overall thruster temperature. The key to the success of this design is the complete decoupling between thermal losses at the anode and at the magnet stack.

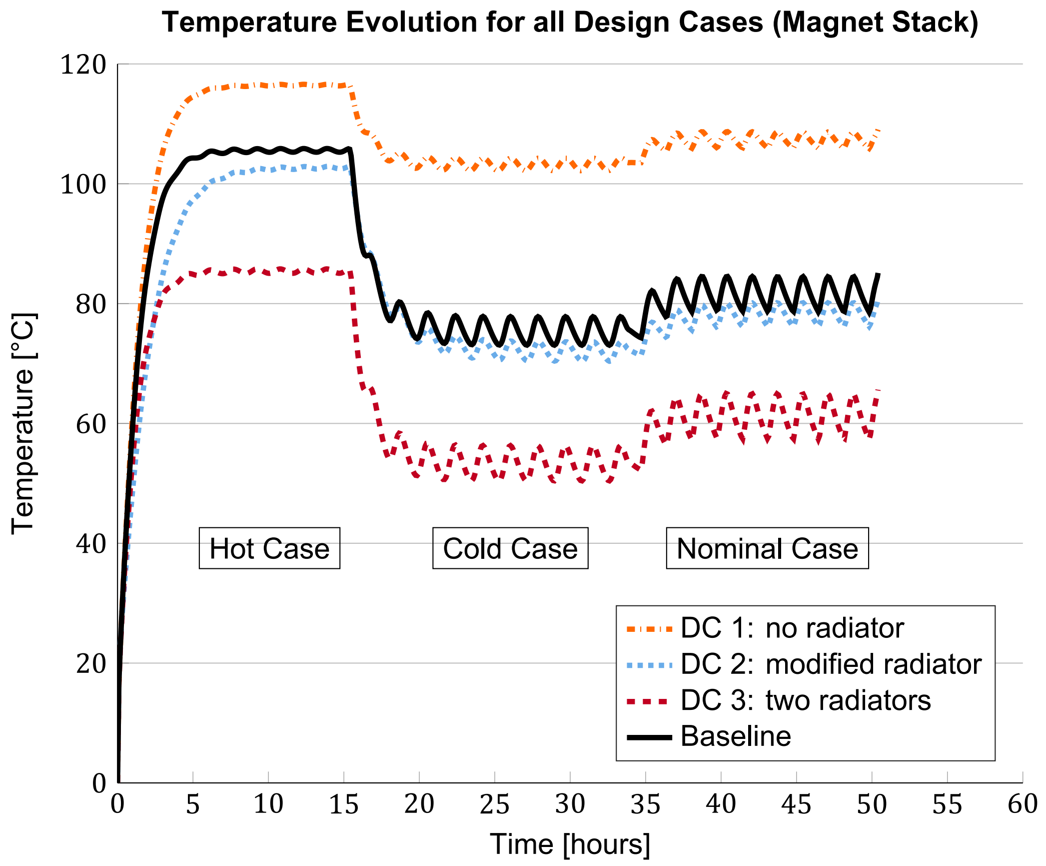

Figure 4.10: Temperature evolution of the hottest node in the magnet stack, for all design cases during the hot, nominal and cold orbits, with the thruster on

Another conclusion that can be obtained from these plots is the poor performance achieved with the modified radiator (Design Case 2). Even if the modified radiator has a better performance than the flat radiator, the modified mount, used for conducting heat from the anode and into the radiator, is not an effective solution. Maximum temperature at the anode is higher than for the baseline, which counted with the heat pipes as a way to guide the thermal losses at the anode into the radiator. The temperature at the magnet stack is reduced in a small quantity, because the hot anode counteracts the benefit from the new radiator shape. It is concluded that the change in shape of the radiator is beneficial, but the heat from the anode has to be handled differently. Manufacturing complexity shall also be considered if this option is further investigated.

The last observation concerns the Design Case 1 (removing radiator). Having a body-mounted radiator has the advantage of a more uniform temperature distribution, regardless of the load case. The difference in temperature between hot case and cold case is reduced from 30°C to 10°C. It has, nevertheless, the disadvantage of an increase in the temperature of the magnet stack and anode. This design case calls for a cost-benefit analysis, on which thermal performance and simplicity of design and size have to be traded off. The mounted radiator

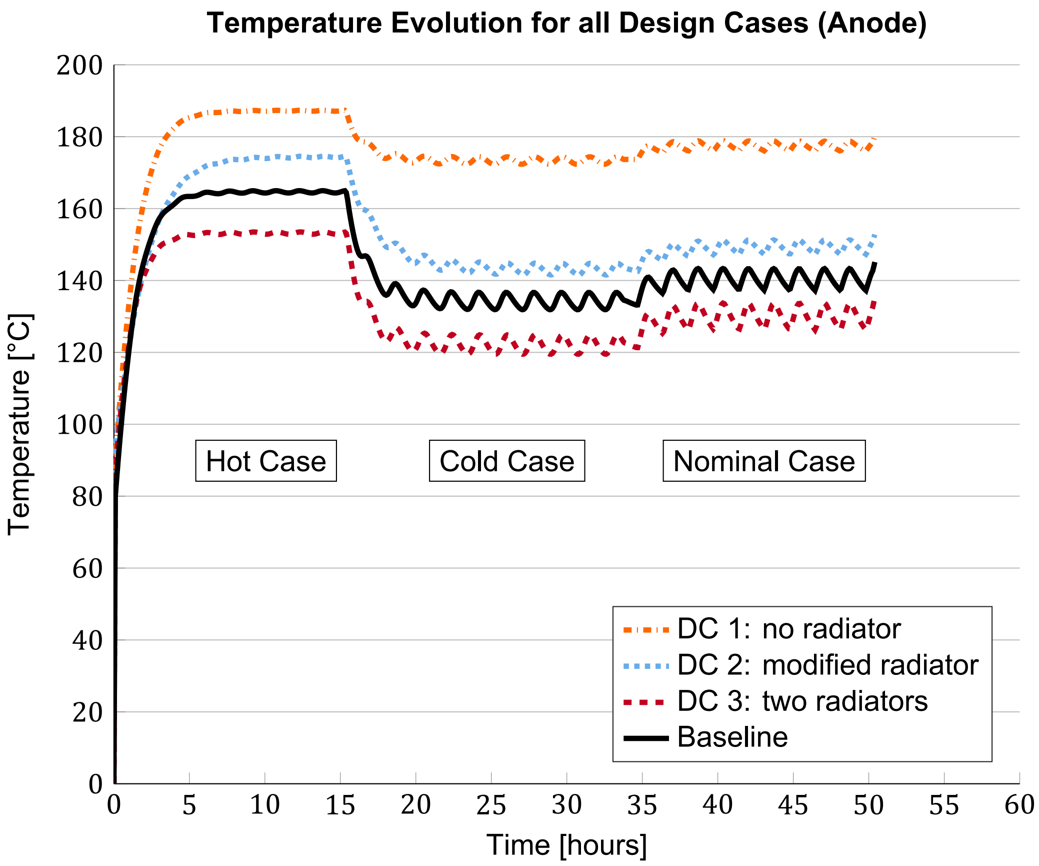

Figure 4.11: Temperature evolution of the hottest node in the anode, for all design cases during the hot, nominal and cold orbits, with the thruster on

is compact and its performance has a low dependency on the load case. Furthermore, the highest temperature reached is still further below the requirement, enabling an input power increase or a further reduction of the housing mass.

Figures 4.12 and 4.13 show the temperature difference between the baseline and the design cases for the hottest locations at the magnet stack and the anode, respectively. In the case of the modified radiator (DC2), the temperature difference is negligible at the magnet stack (it is in the order of magnitude of 5ºC), and 10°C at the anode. Although the design case without radiator shows a high increase in temperature (40°C) for the cold and nominal cases, the temperature only increases 20°C for the hot case, which is the limiting one from the design point of view. This difference is caused by the new orientation of the radiative surfaces, which point in the direction normal to the thrust. When comparing to the baseline (or to the other designs), the body-mounted radiator (DC1) is more protected in the hot case than in other cases against Sun radiation, while the baseline receives the maximum sunlight during this particular case.

As a final comment, the Design Case 3 (two radiators) reduces the temperature at the anode by 10°C and at the magnet stack by 20°C. This improvement is promising, as the mass and volume is similar to the baseline. Heat pipes are avoided, and the only major modification is the transformation of the mount into a second radiator.

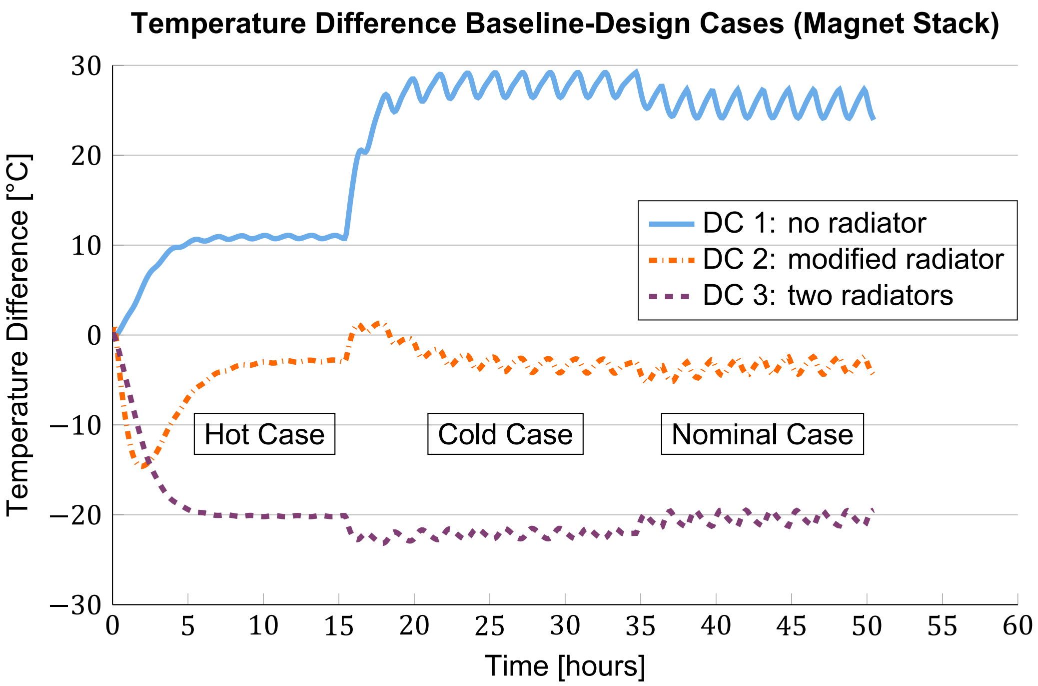

Figure 4.12: Temperature difference between baseline and the different design cases for the hottest node in the magnet stack, during the hot, nominal and cold orbits, with the thruster on

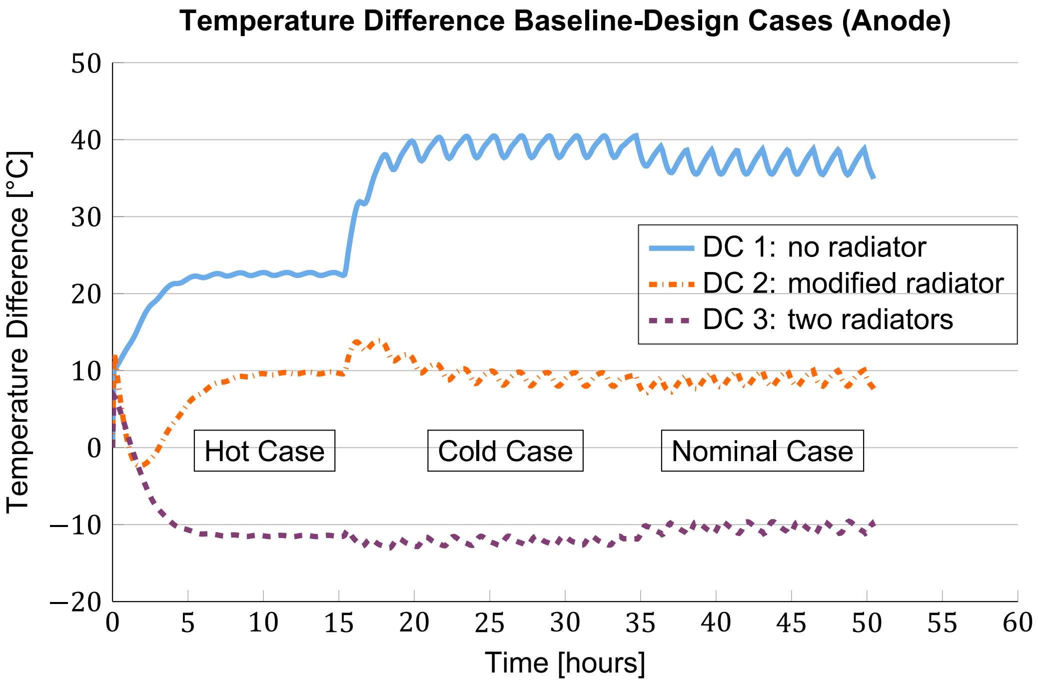

Figure 4.13: Temperature difference between baseline and the different design cases for the hottest node in the anode, during the hot, nominal and cold orbits, with the thruster on

Figure 4.14 illustrates the temperature distribution in the housing for the two radiator design case (DC3), during the steady state of the hot case. As it can be observed, the anode radiator reaches a higher temperature than the magnet stack radiator. This shows how the thermal loss at the anode outweighs the thermal losses at the magnet stack plus the external heat fluxes entering the radiator.

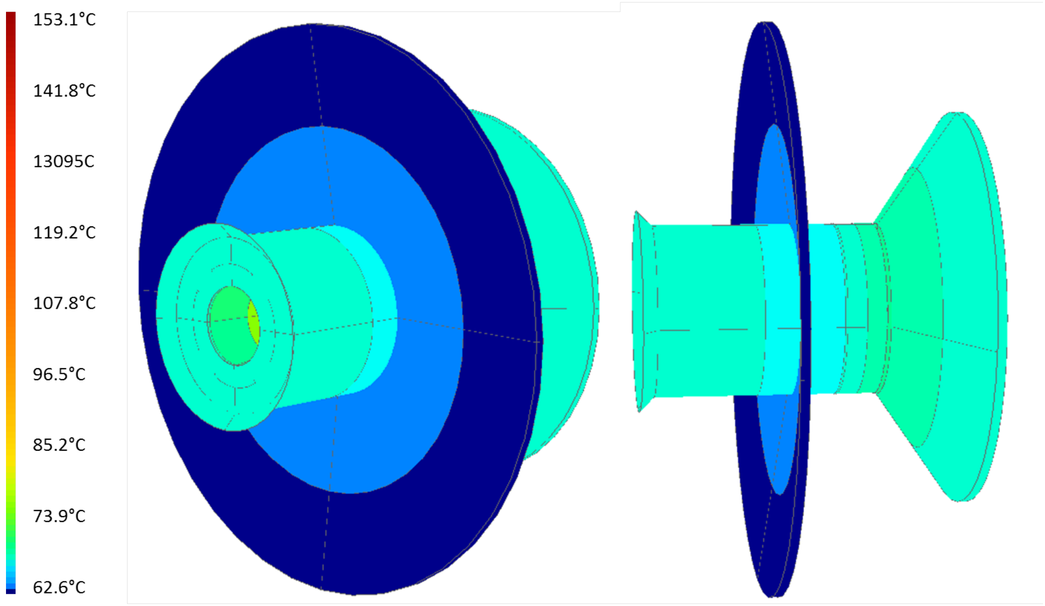

Figure 4.14: Temperature distribution on the Design Case 3 (two radiators) during the hot case, with the thruster on

After having analysed the temperature distributions with the thruster turned on, it is possible to evaluate the performance in the cold cases, with the thruster switched off. Figure 4.15 shows the temperature evolution for all three design cases and the baseline with the thruster turned off. Even if the temperature shown is at the magnet stack, the temperature difference in the model is smaller than the model error, which means that the temperature at the magnet stack is representative of all other temperatures.

From the plot (figure 4.15), it is clear that the design cases 2 and 3 (modified radiator and two radiators, respectively) remain similar to the baseline. When the thruster is turned off, the external heat fluxes drive the temperature distribution. As the radiative area of the thruster remains similar for these two design cases and the baseline (i.e. the area absorbing heat is still the radiator at the magnet stack location and the housing), the heat flux entering the thruster is similar. On the contrary, the Design Case 1 has a completely different radiative area, as the radiator is removed. During the hot case, a small amount of radiation enters the body-mounted radiator, which explains the difference in temperature with the other designs. Similarly, in the nominal orbit, the Design Case 1 reaches a colder temperature because the radiative area exposed to the Sun radiation is in general smaller than for the other design cases. Lastly, all design cases have a similar performance on the cold case because the thruster does not receive any direct sunlight.

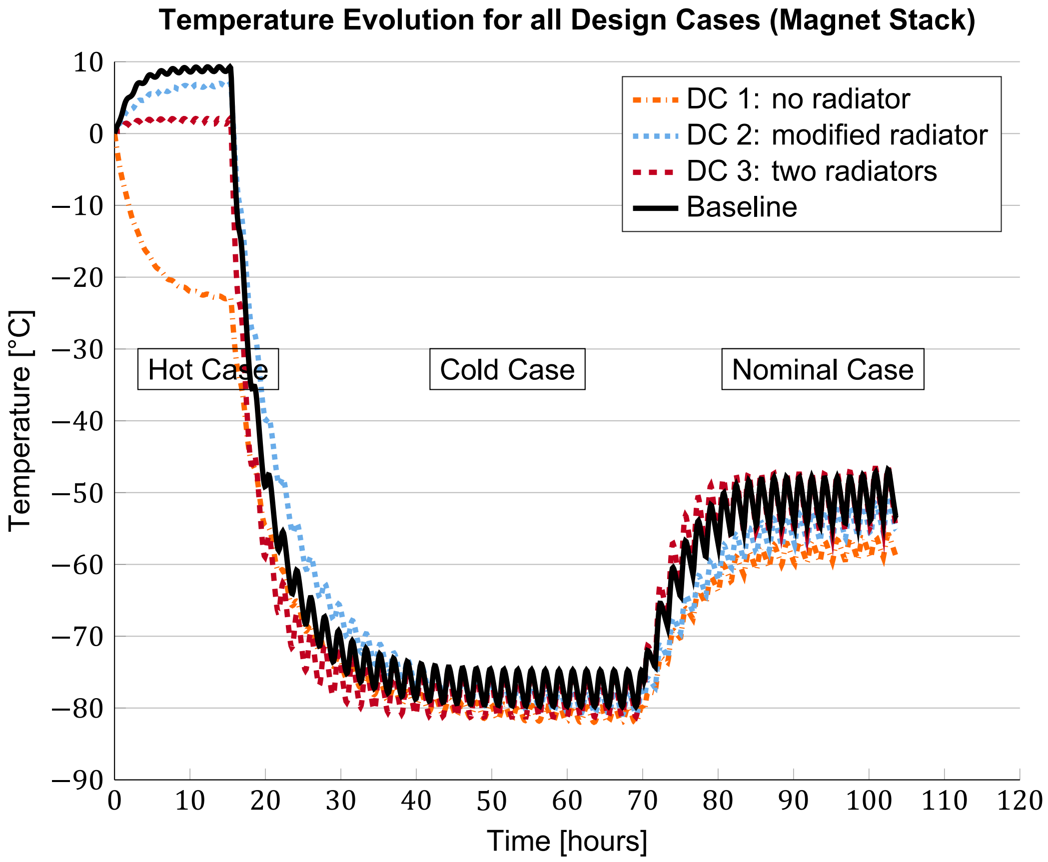

Figure 4.15: Temperature difference between baseline and the different design cases during the hot, nominal and cold orbits, with the thruster off

Table 4.7 shows the temperature difference between the thruster turned on and turned off, for all three design cases and the baseline, during all three load cases. The great increase in this temperature difference that was caused by the boron nitride coating was already discussed in chapter 3. When comparing to the baseline with the new coating, the Design Case 1 increases this temperature difference both at the magnet stack and at the anode. On the contrary, Design Case 3 reduces the temperature difference in all cases, although still not reaching the values from the initial baseline. Finally, the Design Case 2 produces almost no change in the magnet stack temperature difference, and increases it a small amount for the anode.

Table 4.7: Temperature difference between the thruster on and thruster off for all load cases at the magnet stack and anode

	$T_{on} - T_{off}$ **[°C] (Magnet Stack)**			$T_{on} - T_{off}$ **[°C] (Anode)**		
Design Case	**Hot**	**Cold**	**Nominal**	**Hot**	**Cold**	**Nominal**
Baseline (KPT)	55	131	101	114	190	160
Baseline (BN)	97	157	139	155	216	198
DC 1	139	186	168	209	256	238
DC 2	105	160	143	178	232	215
DC 3	84	137	121	152	206	189

Even if one objective was to reduce the temperature difference between the thruster on and off cases, a trade-off with the other objectives has to be done, in order to make a decision on the design modifications. It is clear that the radiator coating and orientation/shape changes, which were the design modifications intended to reduce this temperature difference, did not work as expected, as they ended up increasing the temperature difference between the thruster on and off. The problem was the multi-objective design: these design modifications also intended to reduce the external heat flux into the thruster and to decrease the maximum temperature at the magnet stack. In this sense, the design modifications were focused on the cases with the thruster on, leaving aside the performance with the thruster off.

Table 4.8: Temperature gradient at the magnet stack for all design cases

Design	Case	Max/Min Temp. [°C]	Temp. Diff. [°C]
Baseline	hot	107.3 / 89.8	17.5
	cold	74.5 / 57.3	17.2
DC 1	hot	116.6 / 99.7	16.9
	cold	104.3 / 87.8	16.5
DC 2	hot	102.8 / 84.9	17.9
	cold	73.7 / 56.1	17.6
DC 3	hot	85.8 / 69.2	16.6
	cold	56.3 / 39.5	16.8

As far as the temperature gradient at the magnet stack is concerned, table 4.8 shows the values for all design cases. The variation is below 1°C, far below the model error, which means that the design modifications implemented have no impact on the magnet stack temperature gradient.

In table 4.9, the evaluation of each design case with respect to the objectives is presented. The Design Case 1 has some advantages in terms of envelope volume and reducing the difference in temperature between the load cases. However, the thermal performance is severely hindered, due to the bad management of the thermal losses coming from the anode, as well as the reduction of radiative area. It is then concluded that a redesign of this option can be studied, should the radiator be eliminated for other design reasons.

Table 4.9: Decision table for design cases 1 to 3

Objectives:	1	2	3	4	5	6	7	8	9	Conclusion
DC 1	+	- -	-	0	+	- -	+	0	++	Reconsider anode losses evacuation
DC 2	0	0	-	0	0	+	0	0	0	Better performing radiator shape
DC 3	0	+	++	0	0	++	0	0	0	Further structural analysis

As far as the Design Case 2 is concerned, there are no clear advantages. This design is useful to ensure that the radiator shape of the baseline could not be substantially improved: the temperature change for the magnet stack was in the order of 5°C. However, one thing not considered at this stage, but that should be kept in mind, is that the backward inclination of the radiator creates a higher radiative heat flux from the thruster into the spacecraft (recall figure 4.9, where the location of the side wall relative to the design cases is indicated).

This problem is also encountered by the body-mounted radiator. When a considerable amount of radiation from the thruster impinges the spacecraft panels, a design solution such as a thermal shield (i.e. a physical barrier that blocks radiation) can be implemented between the thruster and the spacecraft. Another option is the use of MLI to cover the backward side of the thruster, reducing the temperature of the outermost surface and in consequence the amount of heat emitted by the radiator into the spacecraft. In conclusion, the Design Case 2 serves to notice the better performance of this radiator shape. However, no implementation is foreseen, given that the advantage is small and there could be derived problems from radiation into the spacecraft.

Finally, the Design Case 3 has the best score, achieving a better thermal performance than the baseline, thanks to successfully decoupling the thermal losses at the anode from the ones at the magnet stack. Subsequently, this design is proposed for further analysis and optimization, from the mechanical and structural points of view. It is believed that after another design iteration, this configuration could be manufactured, integrated and tested in the vacuum chamber. In addition, and recalling the objectives elaborated for the thermal model in section 3.2, the two radiator design accomplishes the last objective: reducing the temperature of the magnet stack during operation via design modifications.

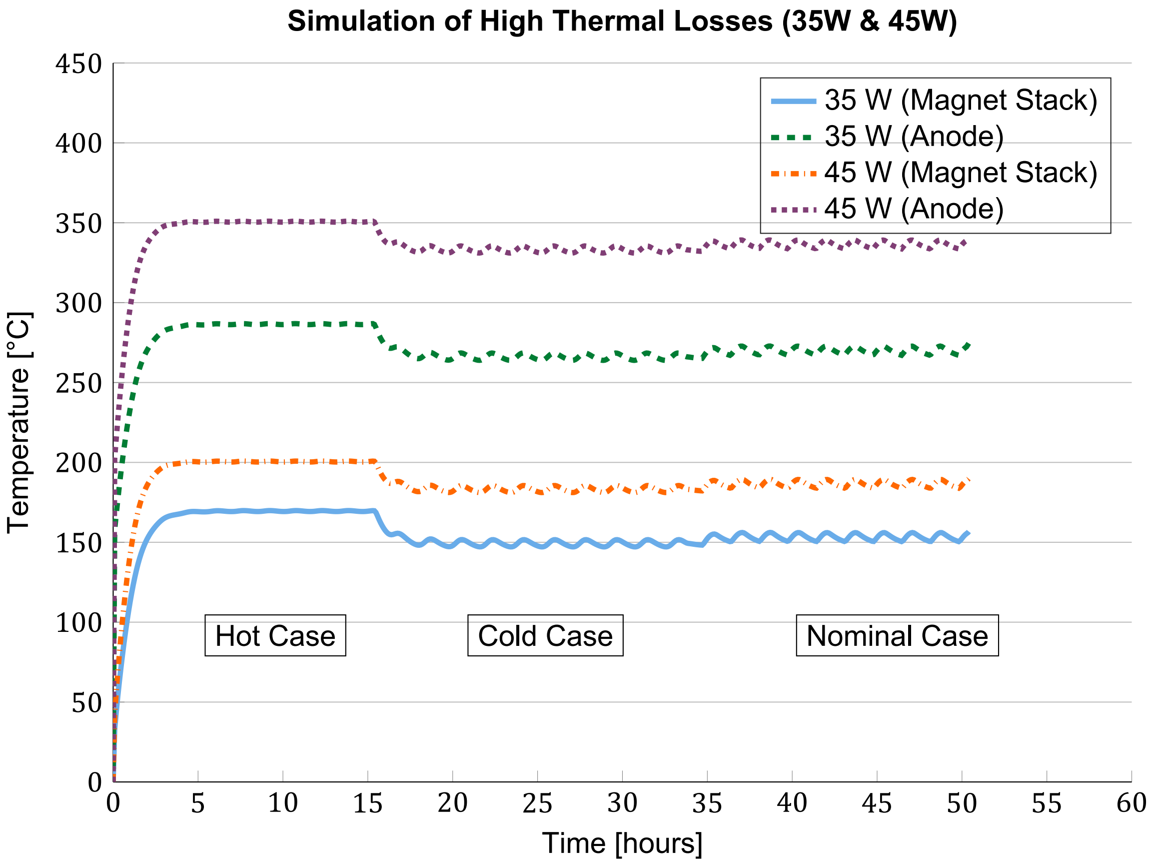

Figure 4.16: Temperature evolution for the baseline design with boron nitride radiator coating, with thermal losses of 35W and 45W, for all load cases

With respect to the requirements, it is now possible to verify requirement THR-TC-201, which states that the thruster shall be able to dissipate 35 W without any component surpassing their allowable temperature. Figure 4.16, done for the baseline with boron nitride coating, shows the temperature at the anode and at the magnet stack for 35 W, proving that the magnet stack does not reach its limit of 200ºC. It also shows the temperature evolution for 45 W of thermal losses, which is the limit of this design. The two radiator design case would allow even higher thermal losses.

5

Conclusions and Recommendations

This is the final chapter, closing the cycle started in the introduction by providing an answer to the research questions. Moreover, this chapter compiles all the conclusions drawn during the development of the thesis, as well as the results obtained. It also includes a set of recommendations for future research in the topic.

To begin with, the answer to the research questions is provided:

1. Which assumptions on the thermal losses inside the thruster can effectively describe its thermal performance?
   It was found that for a 100 W input power, the best assumption was 14.5 W of thermal losses, distributed along the discharge chamber in the following way: 2% at the outer poleshoe, 28% at the mid-outer poleshoe, 10% at the mid-inner poleshoe and 60% at the anode.
    1.1. Which physical processes or parameter values regarding the thermal losses are unknown and have to be assumed?
    The unknown parameters are the value of the thermal losses and their distribution along the discharge chamber. It is known that the losses take place at the anode and at the poleshoes.
    1.2. How does the thermal modelling of the thruster correlate to experimental measurements on the Engineering Model?
    With the assumptions made on the thermal losses, the thermal model correlates to the test data in the following way: 2.85ºC maximum deviation, 1,65ºC mean deviation and 1.96ºC standard deviation.
2. What is the expected thermal behaviour of the thruster during operation?
   The thruster is expected to successfully operate in orbit, as all elements are within their allowable temperatures for the hot, nominal and cold cases, but there is room for improvement.

    2.1. What is the thermal performance when simulating the hot case (thruster on and direct sunlight)?
    The hottest point of the thruster is the anode with 241ºC, and the coldest point is the outer part of the radiator with 163ºC. The magnet stack reaches 183ºC, with a temperature gradient of around 17ºC throughout the stack.
    2.2. What is the thermal performance when simulating the nominal case (thruster on and indirect sunlight)?
    The hottest point of the thruster is the anode varying between 155ºC and 170ºC, and the coldest point is the outer part of the radiator between 75ºC and 95ºC. The magnet stack reaches between 95ºC and 115ºC, with a temperature gradient of around 17ºC throughout the stack.
    2.3. What is the thermal performance when simulating the cold case (thruster off and no direct sunlight)?
    The temperature of the complete thruster is between -50ºC and -40ºC, with a temperature gradient of 3ºC throughout the thruster.

3. Which thermal control system design modifications improve the thermal performance of the thruster?
   The change of kapton tape for a boron nitride coating on the radiator main surface, creating a conductive coupling between radiator and magnets, and either modifying the radiator with a backward inclination or adding a second radiator to decouple the losses at the anode from the ones at the poleshoes.

    3.1. What are the objectives of the design modifications with respect to the thermal performance?
    The objectives are to: reduce the magnet stack temperature, decrease the temperature gradient throughout the magnet stack, lower the difference in temperature between load cases with the thruster on, and shorten the temperature difference between the thruster on and off.
    3.2. Which design modifications effectively address the objectives?
    The change of kapton tape for a boron nitride coating on the radiator main surface reduces the temperature at the magnet stack. Creating a conductive coupling between radiator and magnets reduces the temperature gradient in the magnet stack. Modifying the radiator with a backward inclination reduces the temperature of the magnet stack. Finally, adding a second radiator to decouple the losses at the anode from the ones at the poleshoes reduces the magnet stack temperature.
    3.3. What is the increase in performance achieved with the design modifications?
    The increase in performance is: 80ºC reduction of the magnet stack temperature, with an additional 5ºC when modifying the radiator or 20ºC when adding a second one, 13% reduction of the magnet stack temperature gradient; and 70ºC decrease in the temperature difference between load cases with the thruster on.

All research questions were answered successfully by the research presented in this thesis, from which it follows that the research objectives are met. However, the research questions do not cover all the conclusions obtained while carrying out the research. The rest of the conclusions are presented hereunder. From the initial description of the Engineering Model, two problems were identified:

A - The highest temperatures achieved by the thruster are unknown.

B - The thermal performance of the thruster outside the testing environment is unknown.

Problems A and B were related to requirements which could not be verified with the available test set-up. Requirements THR-TC-100/101/102 were not verifiable because the Sun, Albedo and IR Earth radiation cannot be simulated in the laboratory at Airbus. Requirement THR-TC-200 could not be verified because the size and geometry of the thruster does not allow the integration of sufficient temperature sensors so as to measure the highest and lowest temperatures. The conclusion drawn from these problems was that a thermal model was required, with which orbital conditions could be simulated and the temperatures at every location of the thruster could be computed. All of these problems were solved by the thermal model, and the requirements were verified.

Prior to developing the thermal model, a set of objectives was elaborated:

1. Obtain the temperature distribution of the thruster under the load cases.
2. Demonstrate thermal feasibility of in-orbit thruster operation.
3. Reduce the temperature of the magnet stack during operation with design modifications.

Objectives 1 and 2 were successfully met with the simulation of the Engineering Model (baseline design) in orbit, under the load cases and always maintaining the elements within their allowable temperatures. Objective 3 was met through design modifications, reducing the maximum temperature reached by the magnet stack during the load cases by more than 80ºC, as it was shown in the answer to research question 3.

Continuing with the thermal model, three uncertainties had to be dealt with: thermal losses, spatial distribution of the losses and contact conductivities. Thanks to the successful correlation of the thermal model to the test data, the uncertainties were avoided and verified. This increased the knowledge of the HEMPT working principles and in particular the Engineering Model.

The value of the thermal losses was found to be 14.5 % of the input power, far from the calculated theoretical value: 35%, but close to the value obtained for the HEMPT3050 developed by Thales: 15% [24]. When computing the thermal losses analytically, double and multiple ionization was not taken into account, as well as recombination processes, which would have led to a lower percentage of losses, as these processes consume more power than single ionization. This however might not account for the big difference of 20 percentage points. Thus, it is believed that the assumption on the beam current could be false. Instead of the beam current being 70% of the anode current, it could be closer to 90%, resulting in higher beam power and ionization losses, and in consequence reducing the calculated thermal losses.

As far as the spatial distribution of the thermal losses is concerned, the found value was 2/28/10/60 % of the thermal losses at the outer, mid-outer, mid-inner poleshoes, and anode, respectively. This is comparable to the results obtained for the HEMPT3050: 8/32/12/48 %. Being the thrusters of different size and with different magnet stack configuration, it was expected a similarity, but not an exact fit. It can be concluded that the anode of the mN-µHEMPT receives a higher heat load than the magnet stack. Further correlation of these results to electron and ion tracing simulations could further shed light on the thermal loss process.

Finally, the contact conductivities are found via correlation to heater test data, with values between 250 and 50,000 W/m^2/K. From the literature, contact conductivities between 1,500 and 120,000 W/m^2/K had been considered. The strong dependency of these values on the surface roughness, pressure of the contact and material thermal conductivities created a high dispersion in the reference values, which is why testing of the real set-up was the normal procedure of calculation. This was the approach taken in this case, ending up with coherent contact conductivities that satisfied the following rules: contact conductivity increase with thermal conductivity and contact pressure decreases, and decreases with hardness and surface roughness.

As far as the design modifications are concerned, several conclusions were obtained. To begin with, it was seen that the boron nitride coating successfully reduced the heat load coming from external radiation. This resulted in a lower temperature at the magnet stack, principally during the hot case, for which the Sun radiation has a greater contribution to the total heat entering the thruster. In addition, the temperature difference between load cases with the thruster on was reduced. However, the temperatures with the thruster turned off were also reduced, which in the end increased the temperature difference between thruster on and off. A trade-off between the two effects had to be done. In the end, the final decision was to implement the coating already in the Engineering Model, in order to gain expertise on boron nitride coatings for thruster testing. The boron nitride properties were also verified through testing of several samples with different coating thickness and application methods, achieving a 0.83 emissivity and 0.09 absorptivity. Given its low price and better performance than simple white paint, due to a lower α/ε ratio, its application as radiator coating for thruster testing has a promising outlook.

Be that as it may, a reassessment of the coating would need to be done in a future design iteration, in which structural analysis determines the effect of temperature cycling and low temperatures on the thruster structure. Possibly, a coating with lower α/ε ratio would be selected, with more average properties.

The removal of the heat pipes had a negative effect on the temperatures of the thruster, although almost negligible for the magnet stack. Its advantage was simplifying the design, as the heat pipes are a source of errors and possible failure. It was concluded that further re-designs of the thruster should avoid the use of heat pipes. With the intention of reducing the temperature gradient at the magnet stack, the creation of a conductive coupling between radiator and magnet stack was simulated. It resulted in a 13% improvement, and will be implemented on the baseline whenever a new radiator is manufactured.

Regarding the design cases, all three options resulted in interesting conclusions. Replacing the external radiator for a body-mounted one hindered the performance, as the total area was reduced, but only in a small quantity. The anode losses were not managed successfully, and thus ended up heating the magnet stack. It was also seen that the existing radiator could be improved. By inclining it backwards, performance was increased, although only in a small factor. The most important observation made was that decoupling the thermal losses at the anode from the ones at the magnet stack reduced the temperature at the latter noticeably. The addition of a second radiator to evacuate the heat from the anode was the best performing solution, and its further development should be considered.

Finally, appendix F shows the verification status of the thermal control requirements. Requirements THR-TC-400, THR-TC-401 and THR-TC-600 are not verified at the moment being, but they will be in a further stage of the thruster development, which was not part of the current thesis. The only requirements that are dealt with in this thesis and are not verified are THR-TC-500 and THR-TC-501, regarding the heat power transferred from the thruster into the spacecraft side wall. While the requirements are 1 W for radiation and 1 W for conduction, the best achieved is 4.4 W for radiation and 2.5 W for conduction. This calls for a further analysis of the situation, considering other design solutions such as a thermal shield or covering the thruster with MLI.

As a summary, the recommendations for future research on the thermal losses of the HEMPT system and for the development of the mN-µHEMPT are the following:

- Perform electron and ion tracing simulations and compare them to the results obtained on the thermal losses to further understand the process.
- Investigate the discrepancy between analytically-calculated and experimentally-obtained thermal losses, considering double and multiple ionization in order to find out if other plasma processes are taking place inside the thruster.
- Implement the coating change into the current Engineering Model to gain experience on its performance and suitability for thruster testing.
- Reassess the coating selection, considering the impact of cold temperature and thermal cycling on the structures of the thruster, and investigate the use of a coating with a higher α/ε ratio but more compensated advantages and disadvantages.
- Consider other options for reducing the temperature gradient in the magnet stack, such as adding cobalt rings to the steel poleshoes, taking advantage of the high thermal conductivity of cobalt.
- Further develop the two-radiator design case by performing a structural analysis and defining the mechanical joints of the design.
- Maintain an updated thermal model of the baseline thruster for every major design iteration.
- Investigate an increase in input power (bearing in mind the power limitations on small satellites) or a reduction in mass and volume envelope in order to use the full potential of the thruster, bearing in mind that the magnet stack temperature is almost 100ºC below its allowed temperature.
- Analyse other ways to reduce the heat load from the thruster into the spacecraft, such as a thermal shield or covering the thruster with MLI.

A

Model Sensitivity Analysis

A sensitivity analysis is performed to assess the impact of different model parameters on the thruster temperature. The process followed is to compare the results of a simulation ran with and without modifying one parameter, ensuring that all other variables and boundary conditions stay the same. These simulations are then used to justify the error calculations of the model as well as the assumptions made.

Spacecraft Wall Temperature

To begin with, the effect of the s/c wall temperature on the thruster is analysed (for the in-orbit thruster simulation). With a simple calculation, it is estimated that the outer surface of the spacecraft in LEO would have a temperature of -50ºC. Assuming a worst case, in which the temperature was 25ºC higher (-25ºC absolute temperature), it is shown that the temperature of all parts of the thruster is in the order of 1ºC. Figure A.1 shows the temperature difference at the magnet stack between the models with -50ºC wall temperature (baseline) and -25ºC wall temperature.

Table A.1: Model temperature difference between -50ºC and -25ºC wall temperature. Locations shown are anode, magnet stack and radiator, for all three load cases.

Location	**Temperature Difference [ºC]**		
	Hot	**Cold**	**Nominal**
Magnet Stack	+0.839	+1.083	+1.024
Anode	+0.842	+1.086	+1.027
Radiator (outer side)	+0.840	+1.084	+1.025

Furthermore, table A.1 shows the temperature difference for anode, magnet stack and outer side of the radiator during the different load cases. It is clear that the temperature change is similar in all thruster locations. The impact of a 25ºC increase in the temperature of the spacecraft side wall is in the order of magnitude of 1ºC, which can be considered negligible.

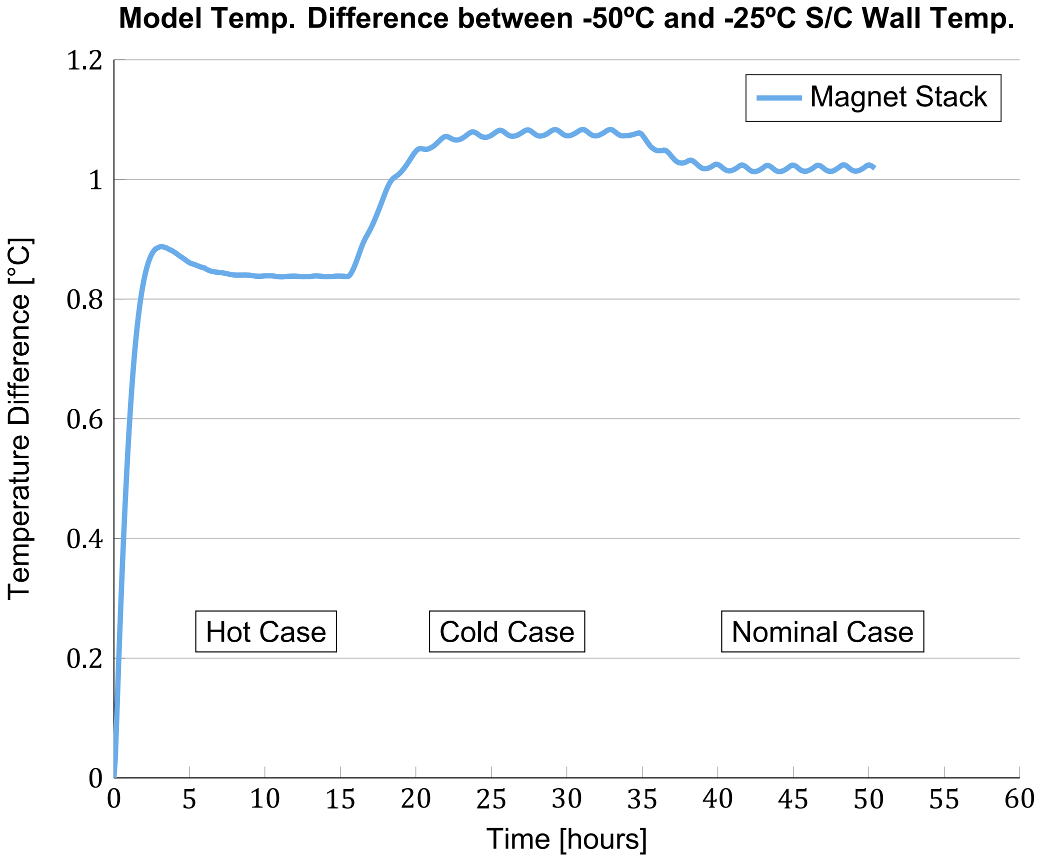

Figure A.1: Magnet stack temperature difference between -50ºC and -25ºC S/C wall temperature. All three load cases are considered.

Glue Layer at Temperature Sensors

Another point that was analysed was the impact of the glue used to attach the PT100s on the measured temperature. An additional thermal coupling was added to the model in the nodes of the temperature measurement to model the effect of the glue. With a thickness of 0.2 mm and a thermal conductivity of 8 W/m/K, the temperature change turns out to be negligible. Table A.2 shows the temperature difference caused by adding these conductive couplings to the model. Notice that the locations shown are anode, magnet stack and radiator, which are not the points at which the PT100s where attached.

Table A.2: Model temperature difference caused by modelling the conduction through the glue of the PT100s. Locations shown are anode, magnet stack and radiator, for all three load cases.

Location	**Temperature Difference [ºC]**		
	Hot	**Cold**	**Nominal**
Magnet Stack	+0.0006	-0.0014	+0.0012
Anode	+0.0010	-0.0010	+0.0020
Radiator (outer side)	+0.0007	-0.0012	+0.0013

Modelling with Simple Shapes: Area Error

The way of calculating the error introduced by the difference in area was to compute the exact error in one known case and extrapolate it to the complete model. The front housing has four outer fins that were not modelled, accounting for a difference in radiative area of 17% of the total area of the front housing. By running a simulation with an additional 17% of area in this part, the result obtained was that the temperature of the thruster varied less than 0.5ºC. Figure A.2 shows the temperature difference between the model with and without this additional radiative area.

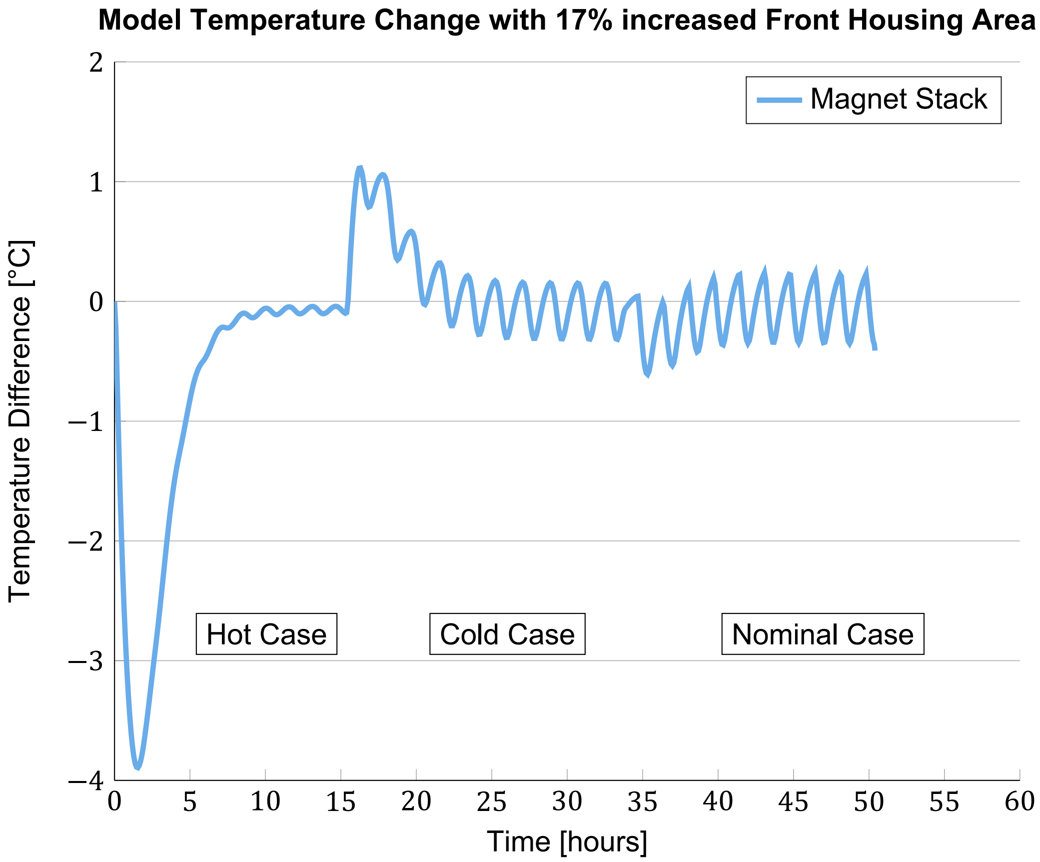

Figure A.2: Temperature difference between the model with and without the additional radiative area of the front housing. The peaks at 2 hours and 17 hours should not be considered as they do not correspond to a steady state. The result is that a variation of +/-0.44ºC is caused by the 17% front housing area increase.

It is sufficient to consider the temperature change at the magnet stack, given the fact that this is almost constant for all parts. Table A.3 shows the temperature change for magnet stack, anode and radiator during a point of the steady state of all three load cases.

The result is that a maximum temperature difference of +/-0.41ºC is provoked by a 17% increase in the front housing area (0.00155 m^2). This represents a 1.2% increase in the total area (0.125 m^2). It is assumed an average 10% area difference between model and reality (the 17% was an exception, and most of the parts would not show this level of inaccuracy). With a simple rule of three, if a 1.24% results in a +/-0.41ºC, then a 5% will result in a +/-1.6ºC variation, which represents the error due to area simplification in the modelling process.

Table A.3: Temperature change for magnet stack, anode and radiator due to additional radiative area of the front housing, during a point of the steady state of all three load cases

Location	**Temperature Difference [ºC]**		
	Hot	**Cold**	**Nominal**
Magnet Stack	-0.088	-0.312	-0.411
Anode	-0.029	-0.231	-0.362
Radiator (outer side)	-0.051	-0.230	-0.318

Effect of Neutralizer

As it was mentioned in section 3.4, the neutralizer inputs an additional 0.26 W into the thruster. Figure A.3 shows the temperature difference between the model with and without this additional power.

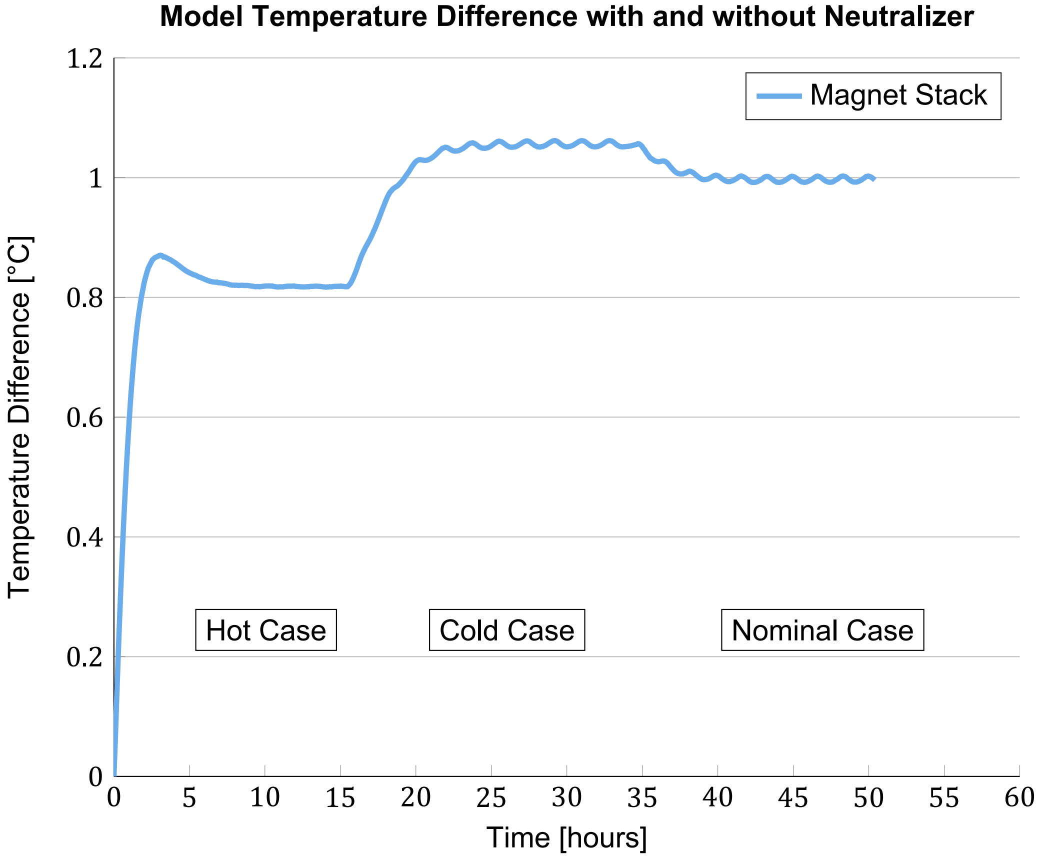

Figure A.3: Temperature difference between the model with and without the additional power due to the neutralizer, at the magnet stack and for all three load cases

Once again, the change in temperature is almost constant for all parts of the thruster, so it is correct to consider only the magnet stack. To justify this, table A.4 shows the temperature change for magnet stack, anode and radiator during a point of the steady state of all three load cases.

The result is that an error of around +1.0ºC should be introduced for not considering the neutralizer in the thermal model.

Table A.4: Temperature change for magnet stack, anode and radiator due to the additional power due to the neutralizer, during a point of the steady state of all three load cases

Location	**Temperature Difference [ºC]**		
	Hot	**Cold**	**Nominal**
Magnet Stack	+0.818	+1.061	+1.003
Anode	+0.816	+1.060	+1.001
Radiator (outer side)	+0.832	+1.076	+1.002

Vacuum Chamber Wall Temperature

The effect of the chamber wall temperature on the thruster temperature was computed with a simplified mathematical model. Assuming two nodes (thruster and chamber), the equation of heat balance in steady state is as follows:

$$Q_{in} = \sigma \cdot \varepsilon_{thr} \cdot A_{thr} \cdot (T_{thr}^4 - T_{cha}^4) \tag{A.1}$$

This equation says that the heat entering the thruster as thermal losses is evacuated through radiation into the chamber. By isolating the thruster temperature, T_{thr}, and taking the derivative with respect to the chamber temperature , T_{cha}, it is possible to calculate the effect of a differential variation of the chamber temperature on the thruster temperature:

$$T_{thr} = \sqrt[4]{T_{cha}^4 + \frac{Q_{in}}{\sigma \cdot \varepsilon_{thr} \cdot A_{thr}}} \quad \rightarrow \quad dT_{thr}/dT_{cha} \quad \rightarrow$$

$$dT_{thr} = \frac{T_{cha}^3}{\left(T_{cha}^4 + \frac{Q_{in}}{\sigma \cdot \varepsilon_{thr} \cdot A_{thr}}\right)^{3/4}} \cdot dT_{cha}$$

With the values of 14.5 W input power, 0.095 m^2 of aluminium radiative area (0.1 emissivity), 0.03 m^2 of black kapton radiative area (0.85 emissivity) and 18.22ºC of chamber wall temperature, the effect of 5 K variation on the chamber wall temperature on the thruster temperature is:

$$dT_{thr} = 0.19 \cdot dT_{cha} \quad \rightarrow$$

$$dT_{thr} = 0.19 \cdot 5\,K = 0.95\,K$$

By performing simulations adding +/-5 K to the chamber wall temperature, it was confirmed that the temperature variation in the different parts was in the order of 1 K. Thus, this is the value considered for the error due to uncertainty in the chamber wall temperature.

Optical Properties

The optical properties used in the Thermal Model have been obtained from the literature. However, specification values may differ from real material and coating values. In order to consider the worst case scenario, a simulation was performed raising 0.01 each absorptivity and reducing 0.01 each emissivity of the Thermal Model (based on ECSS-E-HB-31-03A [37]). Figure A.4 shows the temperature difference in the magnet stack provoked by this change with respect to the baseline thermal model.

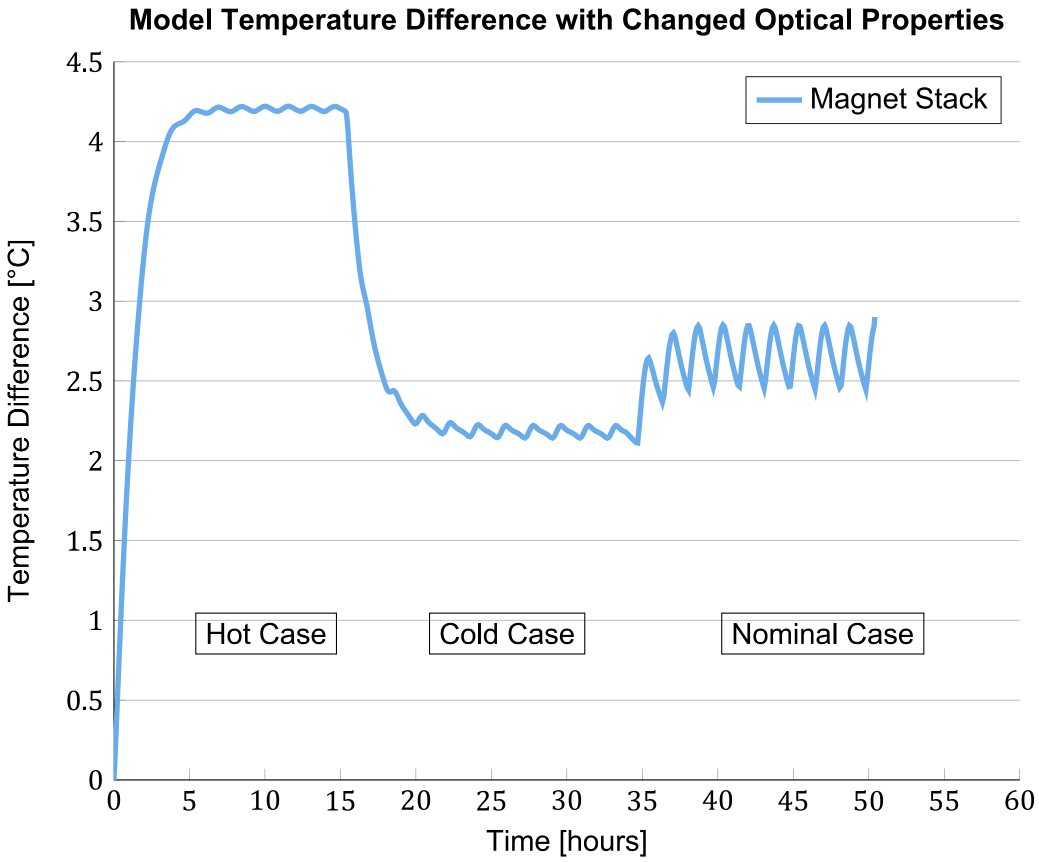

Figure A.4: Temperature difference caused by changing optical properties, at the magnet stack and for all three load cases. The change was to increase 0.01 the absorptivities and decrease 0.01 the emissivities of all parts of the model.

The change in temperature is almost constant for all parts of the thruster, so it is correct to consider only the magnet stack. To justify this, table A.5 shows the temperature change for magnet stack, anode and radiator during a point of the steady state of all three load cases.

Table A.5: Model temperature difference caused by changing the optical properties: increasing all absorptivities 0.01 and decreasing all emissivities 0.01. Locations shown are anode, magnet stack and radiator, for all three load cases.

Location	**Temperature Difference [ºC]**		
	Hot	**Cold**	**Nominal**
Magnet Stack	+4.221	+2.221	+2.900
Anode	+4.192	+2.214	+2.923
Radiator (outer side)	+4.213	+2.218	+2.897

The maximum deviation caused by the change in optical properties is +4.2ºC, for the hot case. By increasing absorptivity and decreasing emissivity, an increase in temperature was expected. When doing the contrary change (reduce absorptivity and increase emissivity), the opposite effect is expected. In the end, a +/-4.2ºC error due to variability in optical properties is considered. This is a worst case scenario in the sense that, most likely, not all optical properties would be erroneous (as considered in this calculation) but only some. Choosing the worst case, however, compensates for higher changes in optical properties (i.e. higher than 0.01 points), which would still be possible.

B

Test Results

The following figures show the results from the thruster and heater testing. Figure B.1 shows the test data for the heater at 10 W. Figure B.2 shows the test data for the heater at 15 W and 25 W. Finally, figure B.3 shows the test data for the thruster at 100 W input power. The decrease in temperature at the end of the test is caused by turning off the thruster, and represents the cool-down.

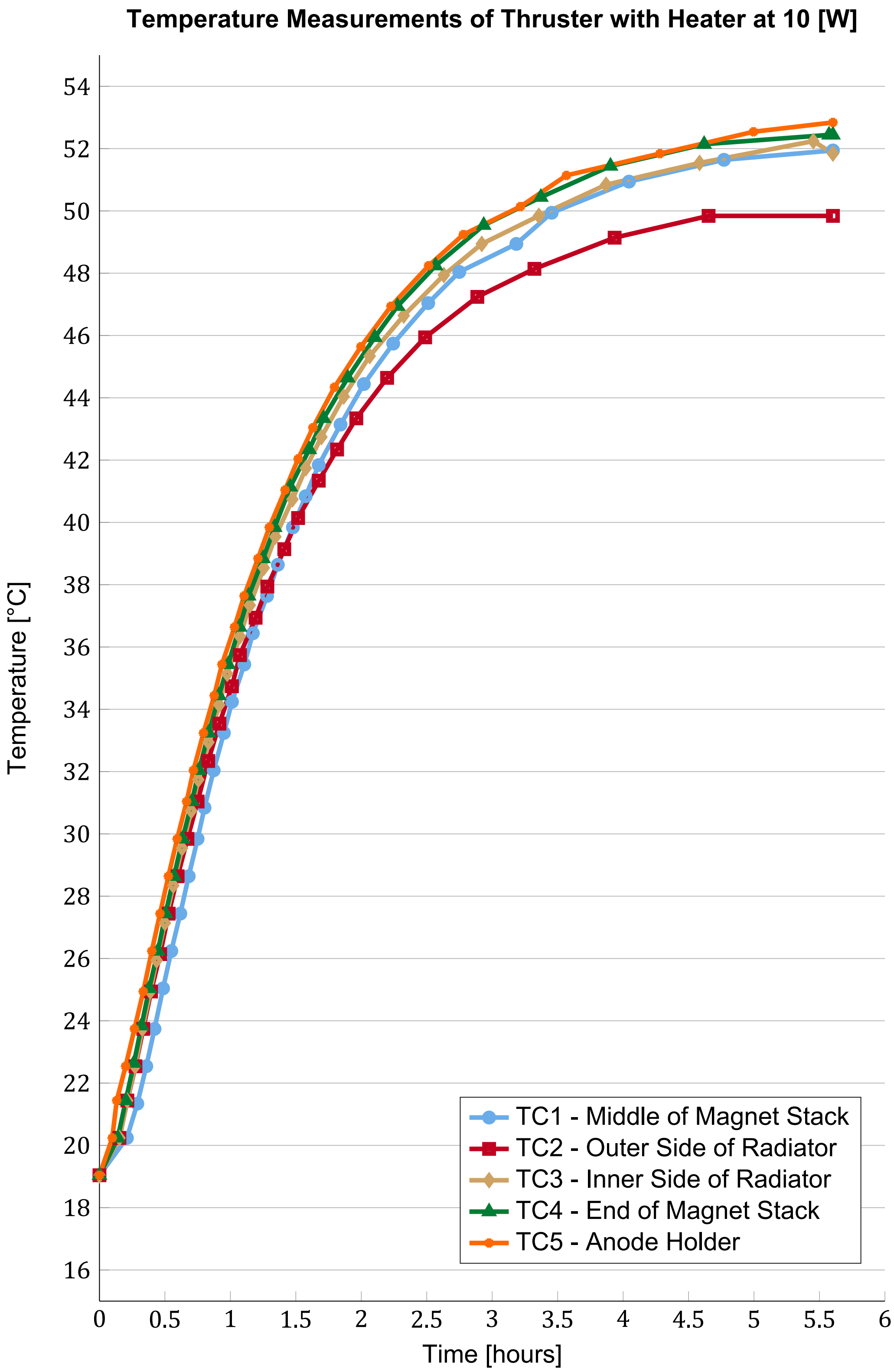

Figure B.1: Evolution of temperature with time at the 5 thermistor locations for 10 W heater

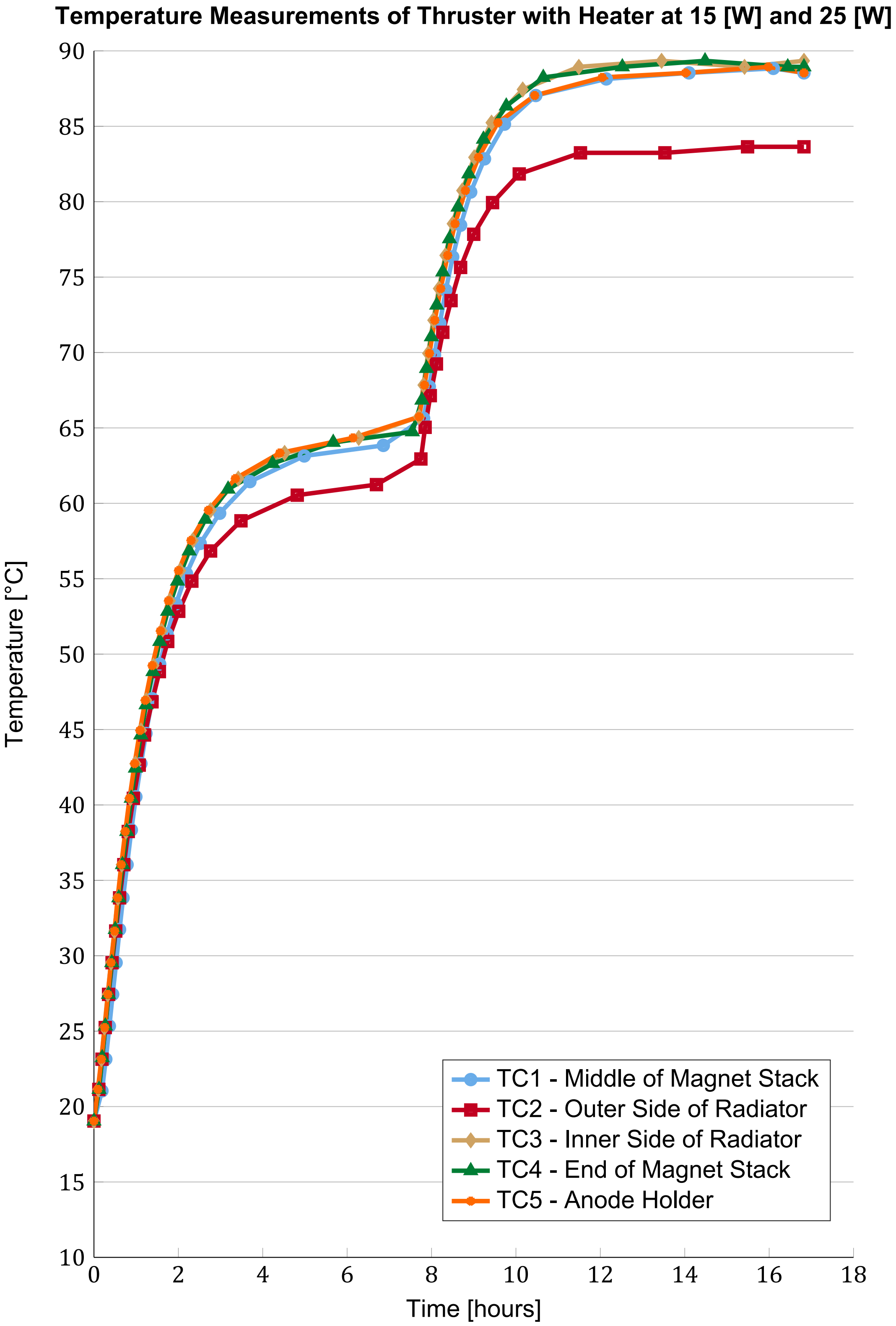

Figure B.2: Evolution of temperature with time at the 5 thermistor locations for 15 W and 25 W heater

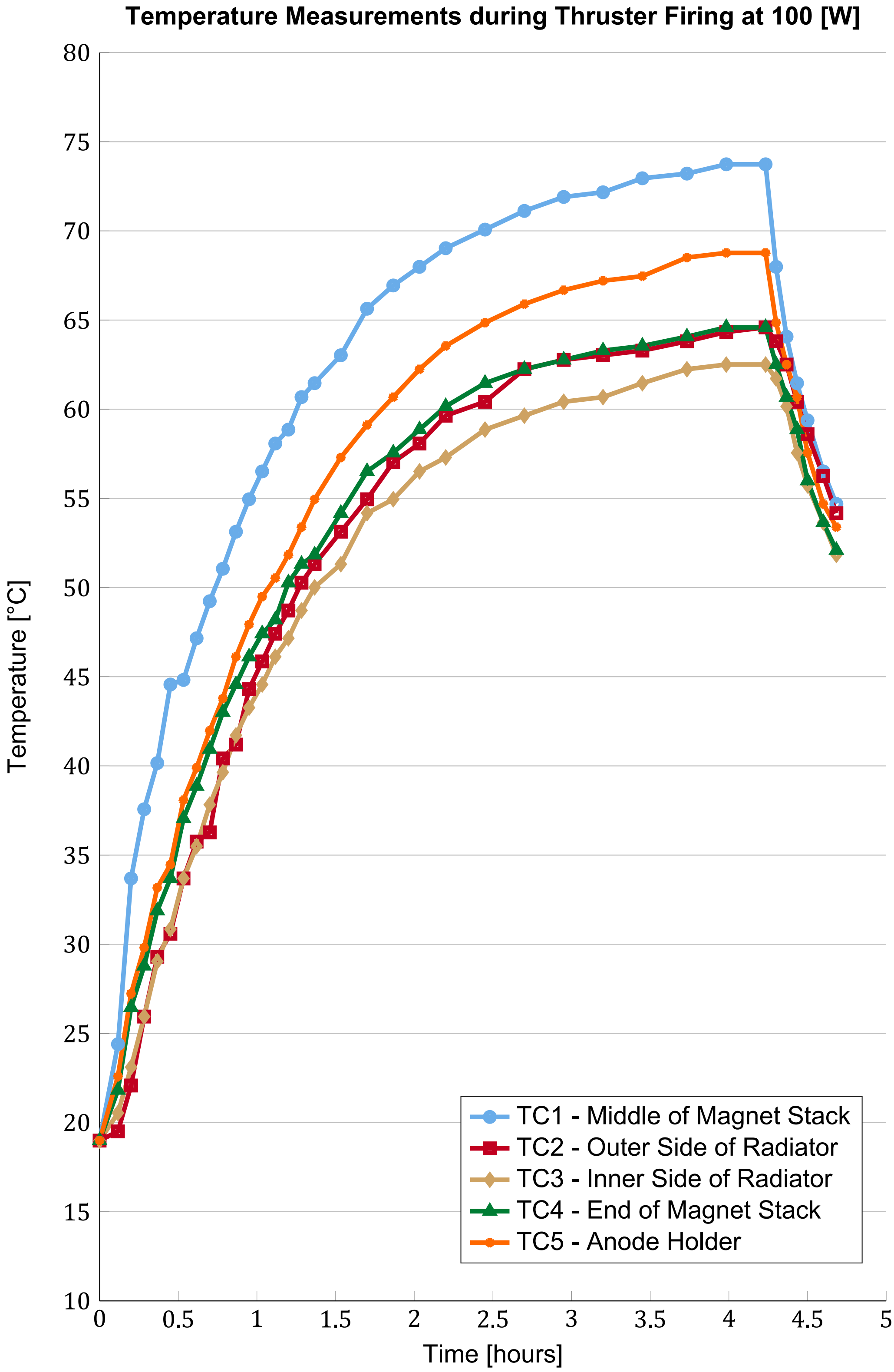

Figure B.3: Evolution of temperature with time during thruster testing for 100 W input power at the 5 thermistor locations. Thruster turned off briefly after 4 hours

C

Insight into the Thermal Model Correlation Process

The purpose of this appendix is to provide further explanation of the Thermal Model correlation process. Each correlation (to heater data, thruster steady state data and thruster transient data) is described in detail, showing the evolution of the design variables until reaching the final configurations. In general, the starting point of the design variables is shown, as well as an intermediate step and the final values selected. For reaching the final solution, multiple iterations and simulations were required, even though only the aforementioned ones are included here.

Heater Testing Correlation via Variation of Contact Conductivities

The first part of the model validation is the correlation of the model to the heater test data. The only variables that are modified during this correlation are the contact conductivities between the different parts. The literature showed a high uncertainty in these values, as mentioned in section 3.3. The value of the contact conductivity depends on the surface roughness, hardness and thermal conductivity of the materials, and pressure in the contact between the parts. Taking this into account, an initial set of values was proposed, in which contacts with high pressure (e.g. bolted joints) or contacts between highly conductive parts had a CC value of 50,000. The other contacts were assigned a CC value of 10,000. All values of the contact conductivities can be seen in table C.1.

Once the model results with the initial configuration are compared to the test measurements, it is clear that modifications of the contact conductivities are necessary, in order to meet the requirements. Table C.2 compares the temperatures measured during the test to the ones produced by the thermal model, and table C.3 shows the deviations (maximum, mean and standard) between the model and the test results. A further refinement of the contact conductivities takes place in a series of iterations, modifying each contact conductivity and assessing their impact on the model temperatures.

Table C.1: Contact conductivities: initial, modified and final values

Interface	**Initial CCs [W/m^2/K]**	**Modified CCs [W/m^2/K]**	**Final CCs [W/m^2/K]**
Magnet - Housing	50,000.0	10,000.0	10,000.0
Magnet - Front Radiator	50,000.0	10,000.0	10,000.0
Magnet - Magnet Press	50,000.0	10,000.0	10,000.0
Magnet - Spacer	50,000.0	10,000.0	10,000.0
Magnet - Poleshoe	50,000.0	20,000.0	20,000.0
Magnet - Chamber Coating	10,000.0	1,000.0	250.0
Poleshoe - Magnet Press	50,000.0	12,000.0	12,000.0
Poleshoe - Chamber Coating	10,000.0	1,000.0	250.0
Housing - Front Radiator	50,000.0	12,000.0	50,000.0
Radiator - Spacer	50,000.0	12,000.0	50,000.0
Radiator - Housing	50,000.0	100,000.0	50,000.0
Radiator - Mount	50,000.0	12,000.0	50,000.0
Radiator - Heat Pipes	50,000.0	10,000.0	45,000.0
Magnet Press - Spacer	50,000.0	12,000.0	12,000.0
Magnet Press - Macor Ring	10,000.0	500.0	800.0
Mount - Vacuum Chamber	50,000.0	12,000.0	12,000.0
Anode Holder - Macor Ring	10,000.0	500.0	800.0
Anode Holder - Anode	10,000.0	1,000.0	1,000.0
Anode Holder - Mount	10,000.0	500.0	500.0
Anode Holder - Heat Pipes	50,000.0	10,000.0	45,000.0
Anode - Macor Ring	10,000.0	1,000.0	800.0
Anode - Chamber Coating	10,000.0	500.0	500.0

As an example of an intermediate configuration before reaching the best fit, a modified contact conductivities configuration is shows in table C.1. The initial values resulted in a very low temperature. Most of the contact conductivities were decreased, passing from 50,000 to 10,000 and from 10,000 to 1,000 in general terms. The only value that was increased was the radiator-housing interface, with the hope of better distributing the heat from the heaters into the front part of the thruster. The CCs between the anode holder and the other parts are also reduced, as the contact is poor (the anode holder is tightly joined to the anode, but not to the mount or macor ring). This latter component has a very low thermal conductivity, which also motivates the reduction in the CCs in which the part is involved.

In view of tables C.2 and C.3, this modified configuration is not yet sufficient, as the deviations still do not meet the requirements; they are only met for the 25 W heater test. With respect to this test, it should be noticed that the correlation is only done for temperature measurements TC1 to TC4. TC5, as explained in section 3.4, is not consistent with the expected physical behaviour (it is located right next to the heater yet it does not reach the highest temperature), so it is not considered in the calculation of the deviations nor the correlation in general.

Further modifications of the contact conductivities resulted in the final configuration. Even if it is the best fit achieved, the values obtained have their limitations. This configuration meets the requirements for all heater tests and in all deviations, which means that further refinement of the contact conductivities is not necessary, as the objective is not to calculate the exact contact conductivities, but to have a sufficiently accurate thermal model. In this sense, there could be different contact conductivities for which a better fit could be achieved (in terms of minimizing the deviations from the test data). The values obtained are sufficient to have a working model, but should be used carefully when drawing conclusions or for use in other models, as their validity may be limited to this case.

Table C.2: Temperature values at the measurement points for different contact conductivities (initial, modified and final configurations), as well as the test data for all heater tests (10, 15 and 25 W)

Case	TC1 [°C]	TC2 [°C]	TC3 [°C]	TC4 [°C]	TC5 [°C]
Heater 10 W					
Test	51.91	50.11	51.95	52.48	52.78
Initial CCs	47.84	46.71	47.43	47.89	49.56
Modified CCs	51.41	49.81	50.81	51.44	56.90
Final CCs	51.95	51.01	51.87	52.03	54.39
Heater 15 W					
Test	63.67	60.94	64.21	64.10	64.35
Initial CCs	60.79	59.07	60.18	60.88	63.41
Modified CCs	65.16	62.75	62.25	65.20	73.36
Final CCs	63.68	62.34	63.56	63.80	67.11
Heater 25 W					
Test	88.47	83.42	89.24	89.10	88.54
Initial CCs	83.94	80.99	82.89	84.08	88.38
Modified CCs	88.92	84.90	87.42	89.01	102.5
Final CCs	87.67	85.37	87.48	87.88	93.40

Table C.3: Temperature deviations (maximum, mean and standard) between model and test (heater at 10, 15 and 25 W) for different contact conductivities (initial, modified and final configurations). The temperature measurement point for which the maximum deviation takes place is also indicated.

Case	Max. Dev. [°C]	Mean Dev. [°C]	Standard Dev. [°C]
Heater 10 W			
Initial CCs	4.58 (TC4)	3.96	4.00
Modified CCs	4.11 (TC5)	1.42	1.98
Final CCs	1.60 (TC5)	0.61	0.85
Heater 15 W			
Initial CCs	4.03 (TC3)	2.59	2.80
Modified CCs	9.02 (TC5)	2.69	4.20
Final CCs	2.76 (TC5)	1.02	1.42
Heater 25 W			
Initial CCs	6.35 (TC3)	4.58	4.79
Modified CCs	1.82 (TC3)	0.96	1.20
Final CCs	1.96 (TC2)	1.43	1.50

Thruster Testing Correlation via Variation of Thermal Losses Distribution

The location of the thermal losses in the thruster is indicated by figure C.1: A is the downstream cusp, B is the middle-downstream cusp, C is the middle-upstream cusp and D is the anode.

The objective of this correlation is to find out how much power is lost at each of these locations, as a percentage of the total losses.

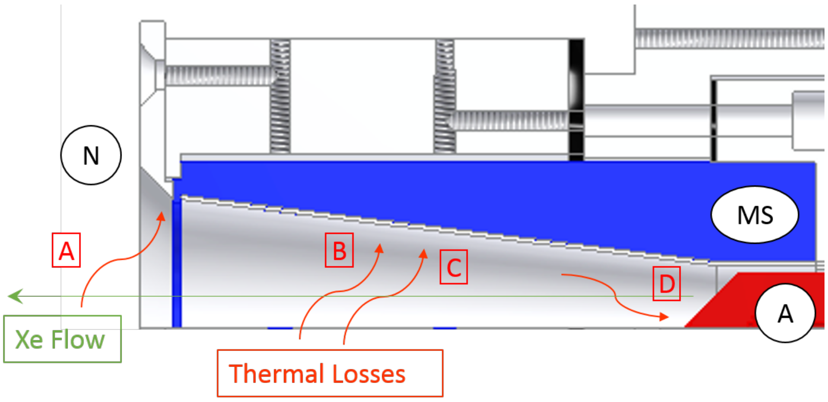

Figure C.1: Thermal losses in the mN-μHEMPT (locations A, B, C and D). The magnet stack (MS), anode (A) and neutraliser (N) are also visible, as well as the discharge flow direction.

The initial values used for the thermal losses distribution were the ones of the HEMPT3050, thruster developed by Thales and taken as reference [24]. As it did not meet the requirements in terms of deviations, the values had to be modified. Table C.4 shows the thermal losses distributions in the initial and final configurations, as well as an intermediate one to illustrate the iterative process. From having 52% losses in the cusp regions and 48% losses in the anode (HEMPT3050 values), the final configuration, which meets the requirements, indicates 40% losses in the cusp regions and 60% losses in the anode.

Table C.4: Thermal losses distributions: initial, modified and final configurations. Regarding the locations: A is the downstream cusp, B is the middle-downstream cusp, C is the middle-upstream cusp and D is the anode.

Losses [% of total losses] → **Case ↓**	**A**	**B**	**C**	**D**
Initial Loss Distribution	8	32	12	48
Modified Loss Distribution	5	30	10	55
Final Loss Distribution	2	28	10	60

Table C.5: Temperature values at the measurement points for different thermal losses distributions (initial, modified and final configurations), as well as the test data for the thruster at 100 W

Case	**TC1 [°C]**	**TC2 [°C]**	**TC3 [°C]**	**TC4 [°C]**	**TC5 [°C]**
Test	73.73	64.59	62.50	64.59	68.77
Initial Loss Distribution	73.20	64.59	65.62	68.00	68.17
Modified Loss Distribution	73.17	64.01	65.52	67.92	68.55
Final Loss Distribution	71.85	63.71	65.11	67.44	68.76

Table C.5 shows the temperatures obtained with the aforementioned losses distributions. The value of thermal losses used to compute these numbers was 14.2 W. Finally, table C.6 shows the deviations with respect to the test results. Notice that the requirements limited the maximum deviation to 3ºC, the mean deviation to 2.5ºC and the standard deviation to 3ºC. The final loss distribution may not be the only one that meets the requirements. It was selected by performing variations of 2% or less in the different locations, which means that and error of 2% should be considered. The values should be used carefully when drawing conclusions. What can be deduced is that the anode of the mN-µHEMPT accounts for around 60% of the thermal losses, while in the HEMPT3050 it was less than 50%. This is a significant change, caused by the difference in size and magnet stack configuration between the two thrusters.

Table C.6: Temperature deviations (maximum, mean and standard) between model and test (thruster at 100 W) for different thermal losses distributions (initial, modified and final configurations). The temperature measurement point for which the maximum deviation takes place is also indicated.

Case	Max. Dev. [°C]	Mean Dev. [°C]	Standard Dev. [°C]
Initial Loss Distribution	3.41 (TC4)	1.64	2.11
Modified Loss Distribution	3.33 (TC4)	1.54	2.05
Final Loss Distribution	2.85 (TC4)	1.65	1.96

Thruster Transient Correlation via Variation of Total Thermal Losses

The final correlation is done for the transient test data. In this case, the only uncertainty left is the value of the total thermal losses. The correlation is done by fitting the model to the last three measurement points of the thruster testing (t=3.73, t=3.98 and t=4.23 hours).

Starting with 14.2 W (the value used for the previous correlation), the thermal loss power is increased in steps of 0.1 W until reaching the ”best fit”, at 14.5 W. Increasing the value of the thermal losses directly increases the temperatures at all thruster locations, as if applying an offset. The final result of 14.5 W is selected because it fits better the test data than 14.4 W and 14.6 W. A step of less than 0.1 W represents 0.1% of the input power to the thruster, and produces temperature outputs with sufficient accuracy so as to meet the requirements in deviations. It represents a 0.1% of the input power to the thruster (100 W) and a 0.7% of the total thermal losses.

Table C.7: Temperature values at the measurement points for different thermal losses distributions (initial, modified and final configurations), as well as the test data for the thruster at 100 W

Case	Time [hours]	TC1 [°C]	TC2 [°C]	TC3 [°C]	TC4 [°C]	TC5 [°C]
Test	t = 3.73	73.21	63.81	62.24	64.07	68.51
	t = 3.98	73.73	64.33	62.50	64.59	68.77
	t = 4.23	73.73	64.59	62.50	64.59	68.77
Model 14.4 W	t = 3.73	71.05	62.91	64.28	66.66	68.04
	t = 3.98	71.28	63.20	64.59	66.94	68.25
	t = 4.23	71.48	63.43	64.82	67.16	68.43
Model 14.5 W	t = 3.73	71.38	63.18	64.56	66.96	68.35
	t = 3.98	71.61	63.48	64.87	67.24	68.56
	t = 4.23	71.80	63.70	65.10	67.46	68.74
Model 14.6 W	t = 3.73	71.71	63.45	64.85	67.25	68.65
	t = 3.98	71.94	63.75	65.15	67.53	68.87
	t = 4.23	72.13	63.97	65.39	67.76	69.05

Table C.7 shows the values of the temperatures for all three thermal losses as well as the test data, and table C.8 shows the deviations (maximum, mean and standard). The case of

14.6 W does not meet the requirement in maximum deviation. Between 14.4 W and 14.5 W, the decision is not as straight-forward, as both input powers meet the requirements, the former having lower maximum and standard deviations than the latter. In the end, however, 14.5 W is chosen, because it is a more conservative case, in the sense that the losses are higher, and thus the thruster has a worse thermal performance.

Table C.8: Temperature deviations (maximum, mean and standard) between model and test (thruster at 100 W) for different values of thermal losses (14.4, 14.5 and 14.6 W) for the three last data measurements. The temperature measurement point for which the maximum deviation takes place is also indicated. Mean values of each case are calculated with the average of the three data measurements.

Case	**Time [hours]**	**Max. Dev. [°C]**	**Mean Dev. [°C]**	**Standard Dev. [°C]**
Model 14.4 W	t = 3.73	2.59 (TC4)	1.63	1.82
	t = 3.98	2.35 (TC4)	1.71	1.87
	t = 4.23	2.57 (TC4)	1.73	1.93
Model 14.5 W	t = 3.73	2.89 (TC4)	1.57	1.87
	t = 3.98	2.65 (TC4)	1.64	1.89
	t = 4.23	2.87 (TC4)	1.66	1.98
Model 14.6 W	t = 3.73	3.19 (TC4)	1.56	1.97
	t = 3.98	2.94 (TC4)	1.61	1.96
	t = 4.23	3.17 (TC4)	1.71	2.07
Model 14.4 W	mean values	2.50	1.69	1.87
Model 14.5 W	mean values	2.80	1.62	1.91
Model 14.6 W	mean values	3.10	1.63	2.00

D

Testing of the Boron Nitride Coating Optical Properties

In order to characterize the optical properties of the boron nitride coating, a test was performed in which ten aluminium plates of 10x10 cm were applied a different coating. Tables D.1 and D.2 show the values of the measurements taken with an IR Emissivity Measurement Device (TIR 100-2 from INGLAS) and a Solar Absorptivity Measurement Device (Optosol Alphameter), respectively. The tests were performed in a clean room. Coatings were not applied following a standard or reproducible procedure, which is why these results only provide an order of magnitude, and should not be seen as definitive. The results obtained, however, as similar to the ones found in the literature: 0.9 emissivity, 0.1 absorptivity. In order to obtain more accurate and reliable results, a qualification campaign should be carried out.

Table D.1: Normal emissivity measurements for different boron nitride coatings. (*) The average value is for hemispherical emissivity, and not normal emissivity like the measurements.

Case	**ε Measurements**					**Average***	σ
Aluminium (no coating)	2.3	2.2	2.3	2.1	2.0	2.8	0.13
Black paint	88.7	88.7	88.8	88.5	88.5	84.2	0.13
HEBO coating (thin)	65.5	65.1	64.9	64.4	64.5	64.9	0.45
HEBO coating (medium)	85.7	85.6	85.3	84.9	84.5	81.4	0.50
HEBO coating (thick)	82.4	82.0	82.5	82.2	82.1	79.0	0.21
Paint brush (thin)	55.7	54.6	57.2	56.4	57.4	57.0	1.15
Paint brush (medium)	88.5	86.1	86.0	86.3	85.8	82.4	1.11
Paint brush (thick)	87.8	87.2	86.9	86.7	86.6	82.9	0.48
Rolled	88.8	88.6	88.1	87.8	87.4	83.8	0.57
Second Surface Mirror	89.3	88.7	88.3	88.1	87.7	84.0	0.61

Figure D.1 shows the emissivity and absorptivity values for each coating. Finally, table D.3 shows the absorptivity to emissivity ratios. A low ratio is convenient for radiator coatings.

Table D.2: Absorptivity measurements for different boron nitride coatings

Case	α **Measurements**					**Average**	σ
Aluminium (no coating)	31.9	30.2	31.6	33.7	32.3	31.9	1.26
Black paint	94.9	94.7	95.1	94.3	94.7	94.7	0.30
HEBO coating (thin)	31.2	25.8	36.0	36.2	28.0	31.4	4.67
HEBO coating (medium)	13.7	15.0	16.4	14.5	15.2	15.0	0.99
HEBO coating (thick)	12.9	15.6	12.6	11.5	12.0	12.9	1.59
Paint brush (thin)	33.1	34.4	31.9	28.1	36.0	32.7	2.99
Paint brush (medium)	14.5	20.9	19.0	18.0	22.7	19.0	3.10
Paint brush (thick)	7.9	9.6	10.7	9.1	9.9	9.4	1.04
Rolled	12.2	12.0	12.8	12.2	13.0	12.4	0.43
Second Surface Mirror	12.3	15.5	13.3	11.2	10.2	12.6	2.04

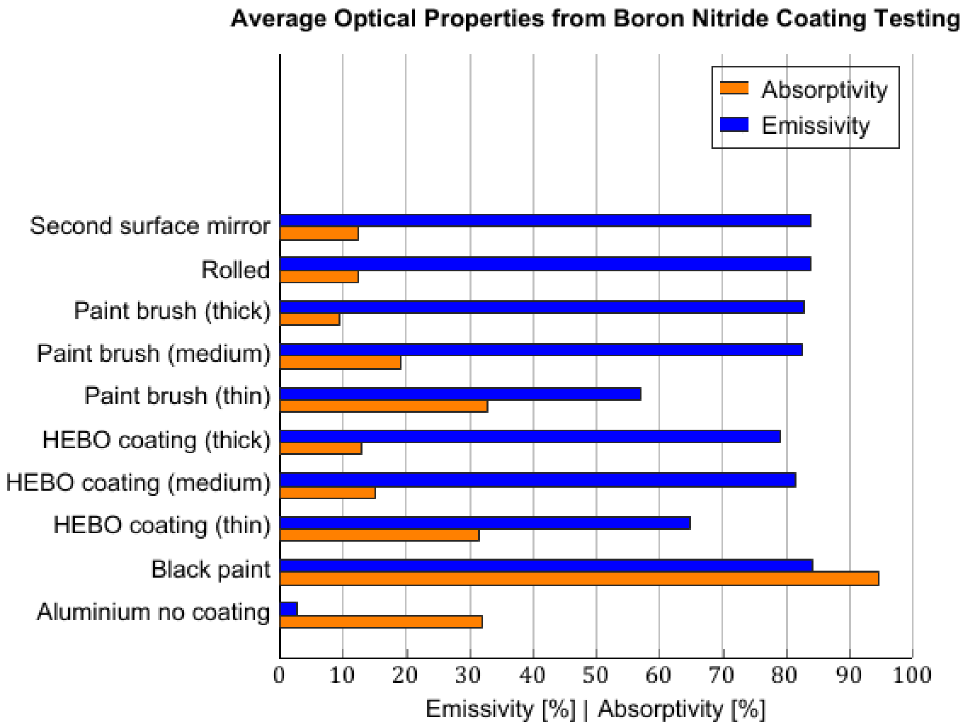

Figure D.1: Absorptivity and emissivity average values obtained from boron nitride testing

Table D.3: α/ε ratio for different boron nitride coatings

Case	α/ε	**Case**	α/ε
HEBO coating (thin)	0.49	Paint brush (thin)	0.57
HEBO coating (medium)	0.18	Paint brush (medium)	0.23
HEBO coating (thick)	0.16	Paint brush (thick)	0.11
Rolled	0.15	Second Surface Mirror	0.15

E

Iterative Process behind the Design Cases

The purpose of this appendix is to shed light into the iterative process followed to obtain the Design Cases.

Design Case 1: No Radiator

The Design Case 1 has as objective to remove the vertical radiator, replacing it by a body-mounted one, which is simply the housing of the thruster with a suitable coating. Due to the important decrease in radiative area, the temperatures of the thruster are expected to increase. However, the compact design has advantages in terms of volume envelope and mass. The heat pipes were removed.

An improvement with respect to simply removing the radiator was to apply an frontward inclination to the housing. This effect was beneficial for the magnet stack temperature, as shown in figure E.1, so the higher the inclination, the better the performance. The inclination limit was given by the mass requirement. An inclination of 15º was already close to the requirement, reaching 1.43 kg (the requirement being 1.55 kg).

Another improvement was given by the addition of an extra part. The mount could be modified in such a way that it provided a conductive coupling between anode and magnet press. This part became an extension of the body-mounted radiator and dissipated the thermal losses at the anode. This part added extra mass, which is why 15º inclination was not possible anymore. The design was then updated with 10º inclination (amounting to 1.41 kg in total). Figure E.2 shows the effect of this improvement on the magnet stack temperature, by comparing the model with and without the conductive coupling between anode and radiator. Both cases already considered 10º inclination.

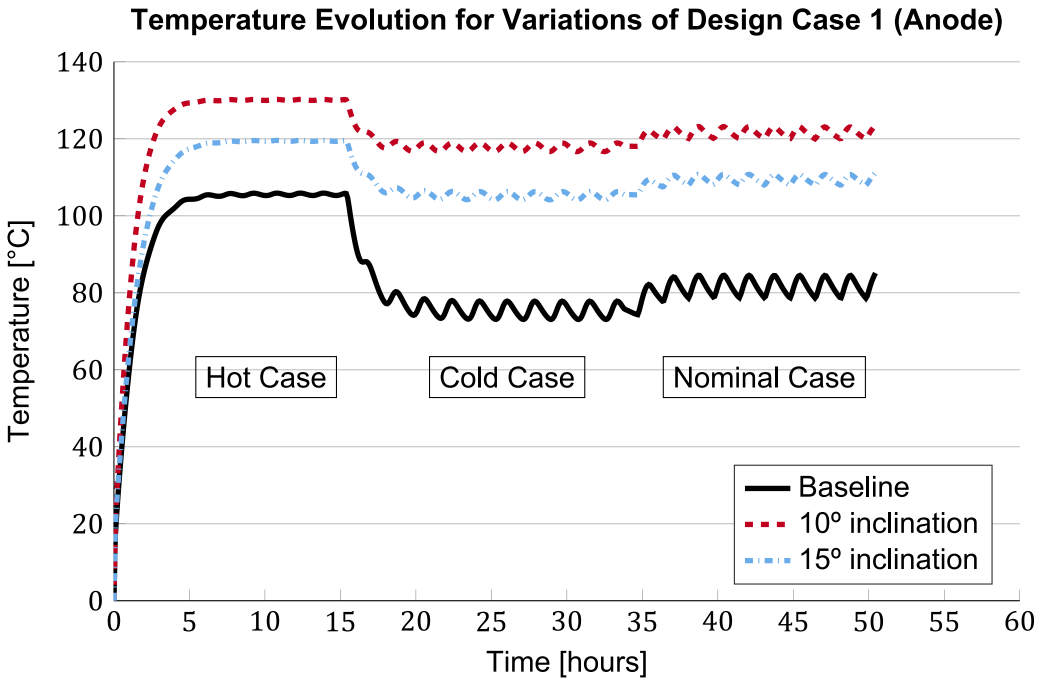

Figure E.1: Effect of body-mounted radiator inclination (10º vs. 15º) on the magnet stack temperature of the Design Case 1

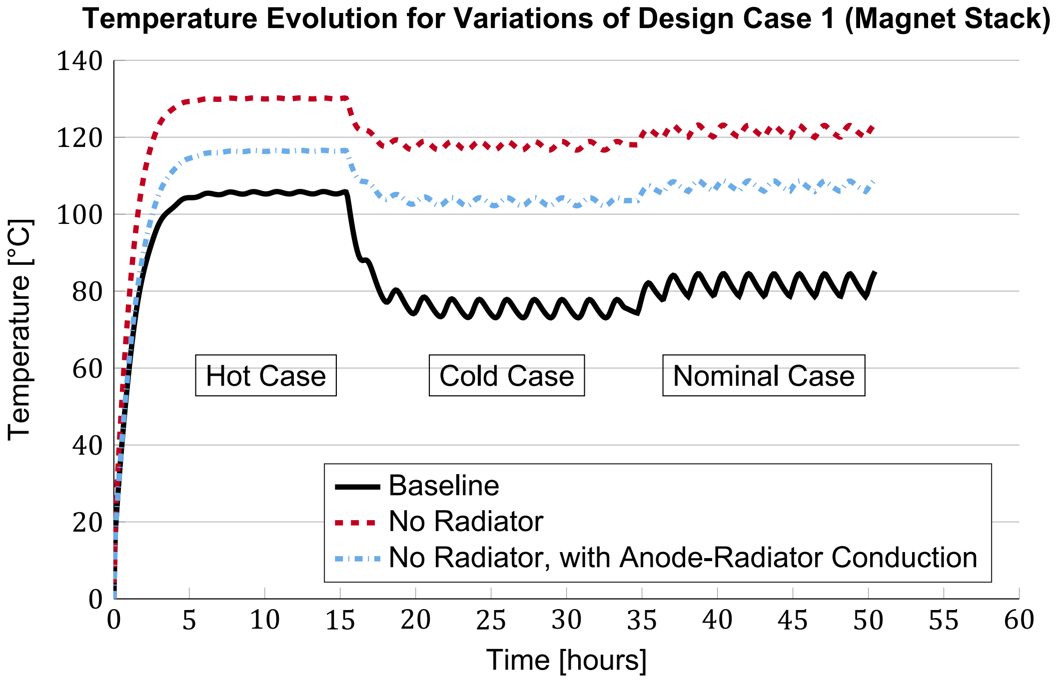

Figure E.2: Effect of anode-radiator conductive coupling (modified mount) on the magnet stack temperature of the Design Case 1

In the end, the Design Case 1 had a body-mounted radiator with 10º inclination and conductive coupling between anode and radiator. The design variables selection was ruled by the requirement on mass.

Design Case 2: Modified Radiator

Figure E.4 shows the three design modifications of the radiator tried: frontward inclination, backward inclination and no inclination (vertical). In all cases, heat pipes are replaced by a mount (yellow in the image) that conduces the heat from the anode into the magnet press and radiator, as in the Design Case 1.

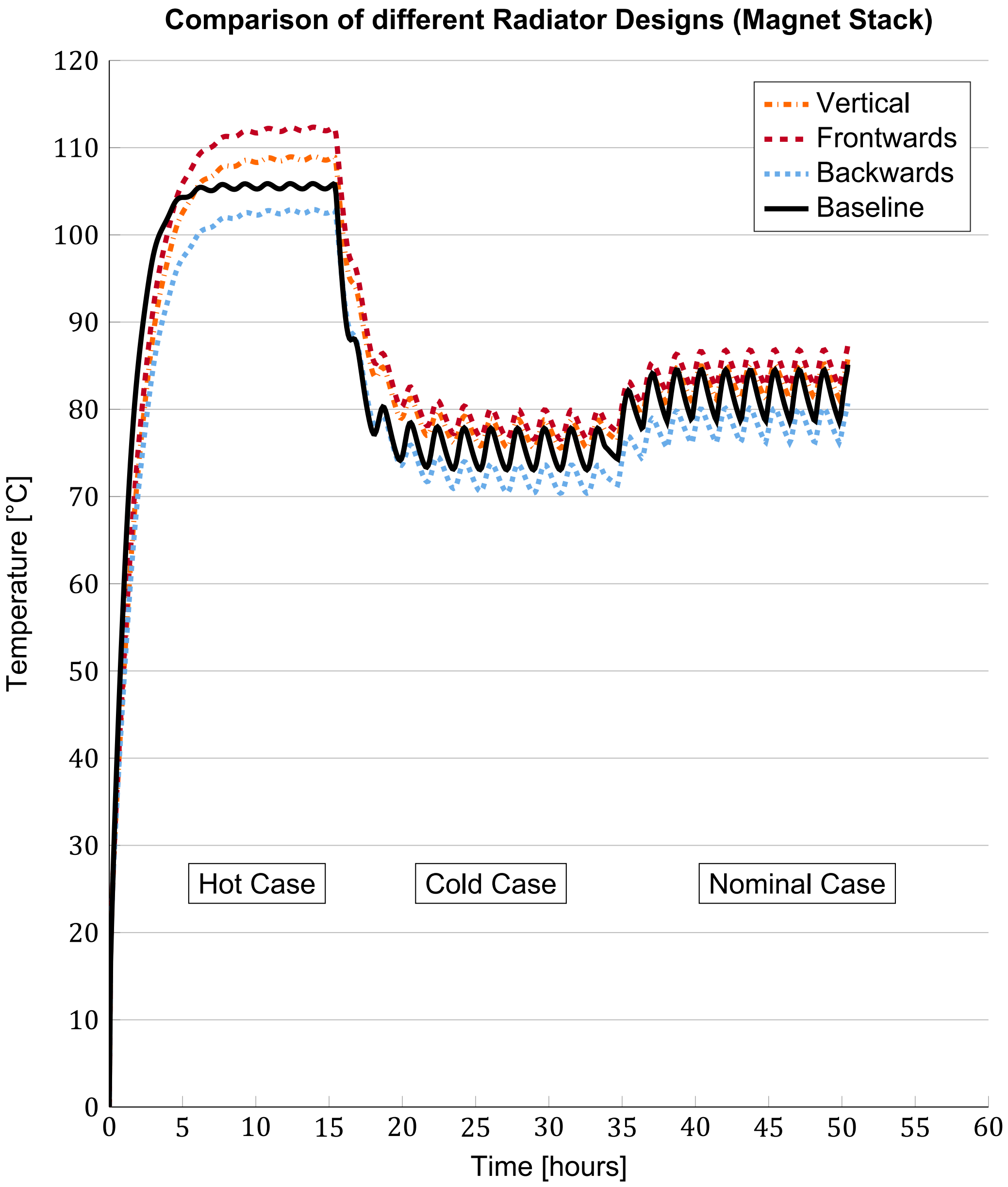

Figure E.3: Evolution of the maximum temperature at the magnet stack for different radiator designs during the load cases, with the thruster on

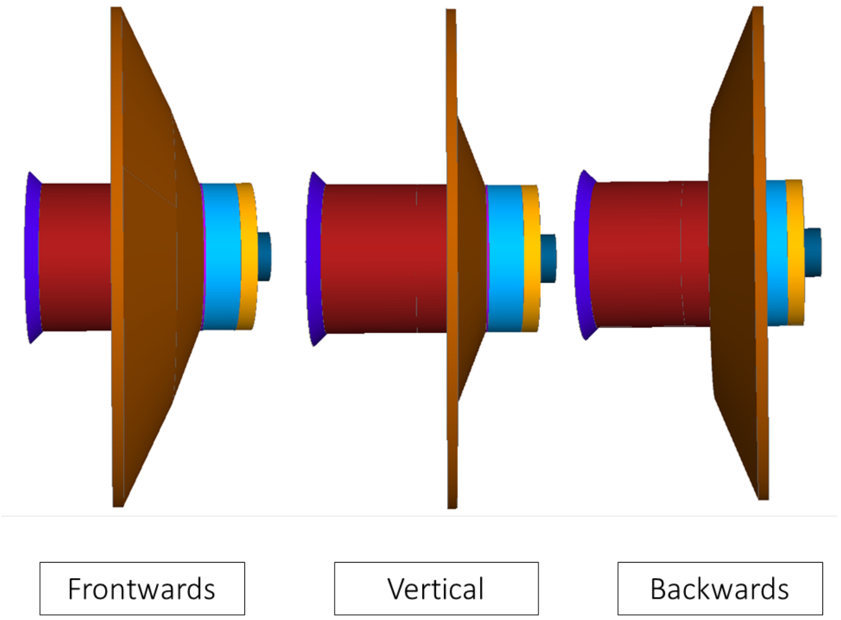

Figure E.4: Different radiator designs: inclined forward, vertical and inclined backward

On the frontwards and backwards inclined radiators, the angle used was 30º. No optimisation was performed to find out the best angle. The idea was to merely assess the impact of the shape. In the case that this design modification is considered for implementation, an optimisation process should be carried out in order to find the optimal inclination angle from both the thermal and structural points of view. Figure E.3 shows the temperature evolution for each case and the baseline, with the thruster on.

It is concluded that only the backwards inclination is an advantage with respect to the baseline design (which apart from a vertical inclination includes heat pipes). From the comparison between the vertical modified radiator and the baseline, it is concluded that the performance of the conductive coupling anode-radiator (modified mount) is less effective than the heat pipes, because it provides a worse thermal performance.

Design Case 3: Two Radiators

The final design case (DC3) analyses the effect of including a second radiator that dissipates the heat from the anode (back radiator). This radiator substitutes the mount, and is attached to the anode holder. The macor ring is maintained in order to decouple the losses at the anode from the losses at the magnet stack. In order to come up with the Design Case 3, a series of design iterations took place. Firstly, a set of 6 design concepts is elaborated (figure E.5) and their performance is assessed (table E.2), for which the orientation of the inner and back radiators are modified. After the best concept is selected, its shape is further modified in variations A to E (figure E.6) and the best design is selected based on the impact on the temperature of the magnet stack (figure E.7).

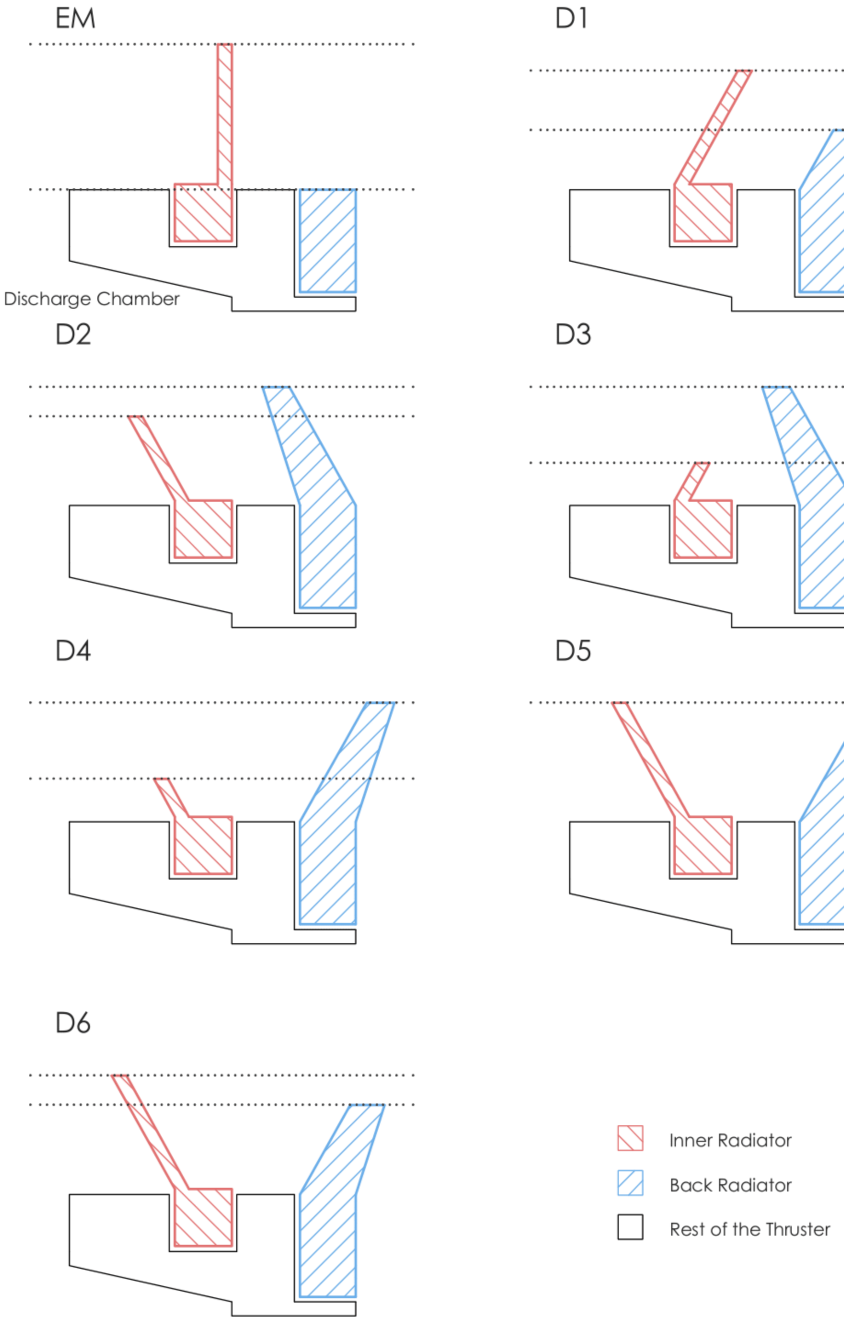

Figure E.5: Different concepts for the Design Case 3 (two radiators). The figure includes the Engineering Model (EM) and concepts D1 to D6. Sizes are not to scale, the shapes only intend to show the relative sizes of the two radiators on each concept.

The way of generating the six design concepts is by analysing the different combinations of radiator orientations. It is important that the radiative surfaces point towards space as much as possible. If they point towards the thruster components, their performance decreases, as the thruster has a high temperature. Another point to bear in mind is the fact that in the hot case (where the highest and limiting temperatures are reached) the thruster discharge chamber points towards the Sun. The more radiative surface that points in this direction, the more external heat flux enters the radiators. All design cases respect the mass and volume envelope restrictions.

D1 has both radiators tilted backwards, with the inner one covering the back radiator during the hot case from the solar flux, achieving a good output to input heat flux ratio (1.52). D2 and D3 have a worse ratio, caused by the forward inclination of the back radiator (it radiates less into space), which also receives solar heat flux in the hot case, as it is not covered by the inner radiator. D4 is again an improvement, as the back radiator manages to better dissipate the heat that it receives from the external fluxes and anode thermal losses. Changing the sizes of the radiators but maintaining the inclinations from D4, the concepts D5 and D6 are obtained. In these ones, the inner radiator covers the back radiator, improving the overall performance (2.57 and 2.8 ratios, respectively). In the end, the best configuration is D6, with an inner radiator inclined frontward and a back radiator inclined backwards.

Table E.1: Dimensions of the radiators of the different concepts of Design Case 3 (two radiators). The outer radius of the radiator, the angle that the radiator is inclined from the vertical and the inclination direction are indicated.

Case	Outer Radius [m]	Angle [º]	Inclination
EM			
Inner Radiator	0.1	0	Vertical
Back Radiator	-	-	-
D1			
Inner Radiator	0.085	20	Back
Back Radiator	0.075	25	Back
D2			
Inner Radiator	0.06	10	Front
Back Radiator	0.09	10	Front
D3			
Inner Radiator	0.05	10	Back
Back Radiator	0.1	10	Front
D4			
Inner Radiator	0.06	10	Front
Back Radiator	0.09	10	Back
D5			
Inner Radiator	0.08	10	Front
Back Radiator	0.08	10	Back
D6			
Inner Radiator	0.085	10	Front
Back Radiator	0.078	10	Back

Comparing the numbers from table E.2 has to be done with care, because not only the shapes of the radiators play a role, but also their sizes. Table E.1 shows the dimensions of each concept to support the interpretation of the heat flux values presented. In view of the dimensions, the data is consistent. Regarding the external heat fluxes, the higher the outer radius, the higher the input power. For the inner radiator, the order from smaller radius to higher radius is as follows: D3 (5.7 W), D2 and D4 (11.0 W), D5 (12.3 W), D6 (13.9 W) and D1 (19.7 W), and finally EM (33.0 W). Even if D6 and D1 have the same outer radius for the inner radiator (0.085 m), their inclination is different: the high inclination of D1 (20°) results in more input power coming from albedo and Earth IR, which is avoided by the low inclination of D6 (10°). A similar analysis can be done for the back radiator, as well as for the heat radiation into space and into the wall. Notice that, once again, the inclination plays a role when analysing the results. For the heat exchange between back radiator and s/c wall, D1 and D6 are different (5.5 W and 2.7 W respectively) not because of the outer radius, but because of the inclination angle, higher in D1, which results in a higher view factor between the radiator and the wall.

Table E.2: Heat fluxes in and out of the radiators for the different concepts (D1 to D6, see figure E.5) of Design Case 3 (two radiators). The radiators receive power from the environment and emit radiation into space and the spacecraft wall. A ratio between heat emitted and heat received is also shown. All heat fluxes correspond to the hot case in steady state.

Heat Flux [W] →	**Environment**	**Space**	**S/C Wall**	**Ratio Out/In**
Case ↓	Q_{env}	Q_s	Q_w	$(Q_s + Q_w)/Q_{env}$
EM				1.39
Inner Radiator	33.0	42.0	4.0	
Back Radiator	-	-	-	
D1				2.00
Inner Radiator	19.7	27.3	1.4	
Back Radiator	3.1	11.6	5.5	
D2				1.45
Inner Radiator	11.0	13.5	0.4	
Back Radiator	21.8	29.7	3.9	
D3				1.48
Inner Radiator	5.7	8.1	0.3	
Back Radiator	25.2	33.5	4.0	
D4				1.63
Inner Radiator	11.0	10.9	0.3	
Back Radiator	12.0	22.5	3.8	
D5				2.57
Inner Radiator	12.3	21.0	1.0	
Back Radiator	4.0	16.0	4.0	
D6				2.80
Inner Radiator	13.9	26.0	1.2	
Back Radiator	1.2	12.2	2.7	

After selecting D6 as the best performing concept, further variations were elaborated: variations A to E (see figure E.6). Variations A, B and C modify the inclination of the inner radiator (0º, 10º and 20º, respectively). Variation D reduces the size of the inner radiator, resulting in a configuration similar to the D5 previously analysed. Finally, variation E changes the inclination of the back radiator to 20º. Notice that D6 is taken as baseline, so the rest of the dimensions stay the same as in that case.

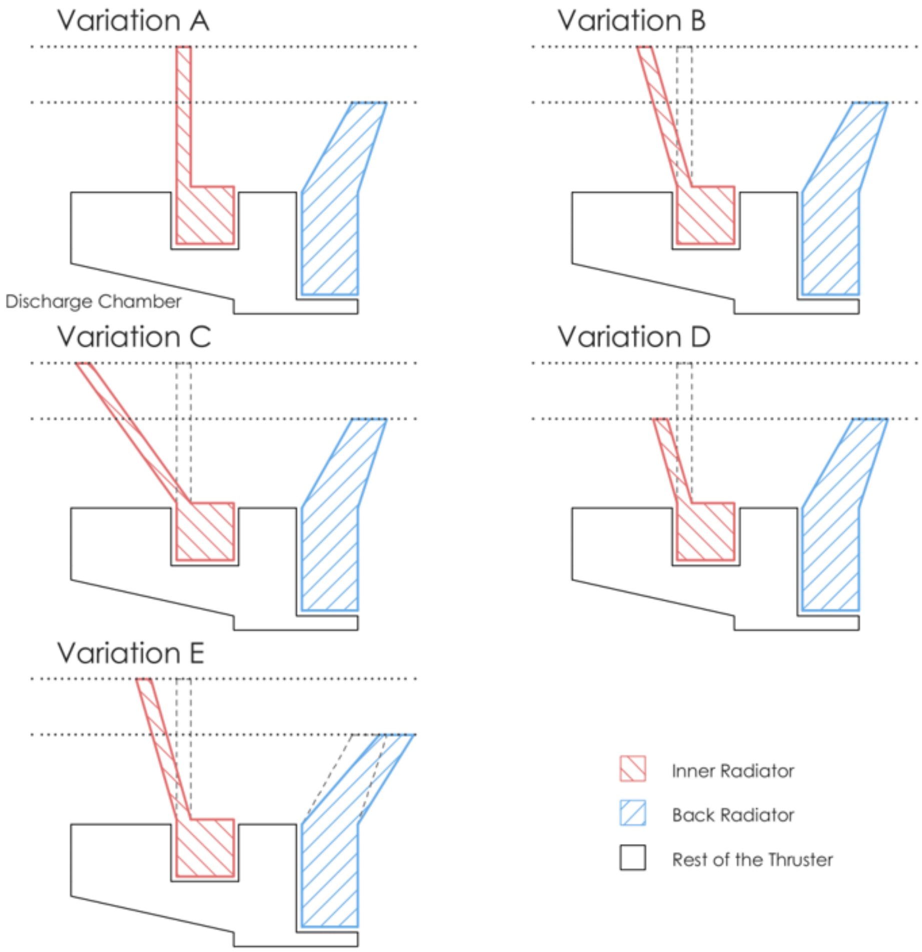

Figure E.6: Variations A to E of the D6 concept (inner radiator inclined forward, back radiator inclined backwards) for the Design Case 3 (two radiators)

Figure E.7 shows the temperature difference between the five D6 variations and the baseline, at the magnet stack. As it was expected, the variation D is the worst performing, because it is not a D6 concept, but rather the D5. The inner radiator does not fully protect the back radiator from the heat flux coming from the Sun and this reduces its performance.

From the results of variations A, B and C, it can be deduced that the performance is improved by pushing the inner radiator forward. However, the best performing solution is variation E, where the back radiator was pushed even more backwards. This is the selected solution, and will represent the Design Case 3. It is clear that a further optimisation of the inclinations and outer radii will be necessary if this design modification is to be implemented. However, for the purpose of these design cases (which is to merely illustrate the effect of the design modifications), no further optimisation is required. At this point, it is clear that the Design Case 3 can reduce the temperature of the magnet stack in 20ºC, which represents an important advantage that will be further assessed in section 4.3.

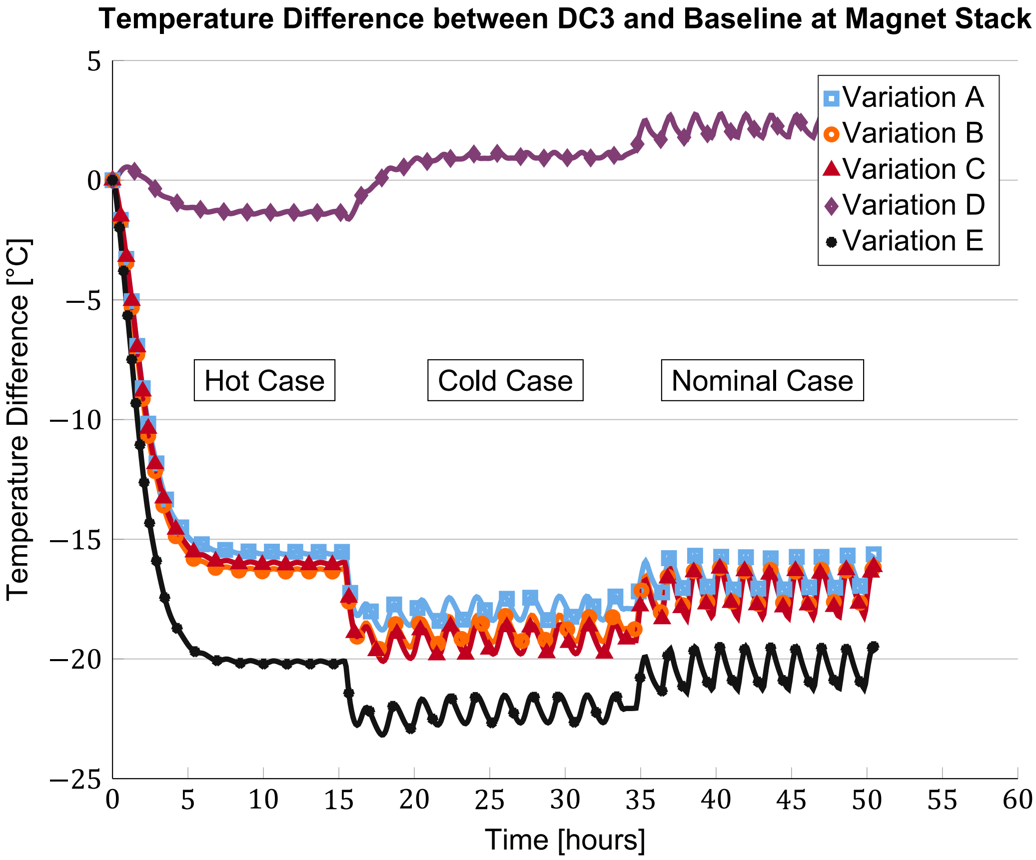

Figure E.7: Temperature difference between the different variations of the D6 concept and the baseline. All variations (A to E) can be seen in figure E.6.

F

Thermal Control Requirements Verification

Table F.1 shows all thermal control requirements. Table F.2 shows the verification status of the thermal control requirements, in which it can be seen that only 5 requirements cannot be verified at the moment, either because the requirement is not met or it will be verified at a later stage of the thruster development.

Table F.1: Thermal control requirements

ID	Requirement
THR-TC-100	The thermal control of the mN-μHEMPT shall enable the nominal operation of the thruster during all mission scenarios in LEO.
THR-TC-101	The thermal control of the mN-μHEMPT shall enable the nominal operation of the thruster on a 400km 06:00h sun-syncrhonous orbit with the thruster always pointing the Sun (hottest mission scenario).
THR-TC-102	The thermal control of the mN-μHEMPT shall enable the nominal operation of the thruster on a 1200km 12:00h sun-syncrhonous orbit with the thruster always pointing away from the Sun (coldest mission scenario).
THR-TC-200	The maximum temperature reached by each component of the thruster shall remain inside the allowable temperature range.
THR-TC-201	The thermal control of the mN-μHEMPT shall be able to dissipate at least 35 [W] of thermal losses generated by the thruster operation in hot case without exceeding the allowable temperatures of the components.
THR-TC-300	The mass of the thermal control hardware shall be less than 1.55 kg.
THR-TC-301	The envelope of the thermal control hardware shall be smaller than R0.1x0.865 m.
THR-TC-400	All materials used for the thermal control of the thruster shall be suitable for space applications.
THR-TC-401	The thermal performance of the system shall be ensured after material degradation at EOL properties.
THR-TC-500	The thermal control of the thruster shall allow a maximum heat flow of 1 W into the other s/c subsystems through conduction.
THR-TC-501	The thermal control of the thruster shall allow a maximum heat flow of 1 W into the other s/c subsystems through radiation.
THR-TC-502	The thermal control of the thruster shall not interfere with the performance of the propulsion system.
THR-TC-600	The thermal control hardware shall be possible to assemble onto the thruster and the rest of the propulsion system.
THR-TC-610	The thermal testing of the thruster shall be done in a vacuum environment of at least 10^{-5} mbar.
THR-TC-611	The thermal testing of the thruster shall be done in a controlled enviroment of less than 3 K temperature variation.
THR-TC-700	The thermal performance of the thruster shall be assessed by thermal analysis only when representative testing is not possible.
THR-TC-701	The thermal analysis shall be performed on space-verified software.
THR-TC-702	The thermal analysis shall be carried out on a representative thermal model (GMM and TMM) of the thruster.
THR-TC-710	The model used for thermal analysis shall be validated via testing.
THR-TC-711	The thermal model shall be correlated to testing with a maximum deviation of less than 3°C on the temperatures at the reference points.
THR-TC-712	The thermal model shall be correlated to testing with a mean deviation of less than 2.5°C on the temperatures at the reference points.
THR-TC-713	The thermal model shall be correlated to testing with a standard deviation of less than 3°C on the temperatures at the reference points.

Table F.2: Thermal control requirements verification status

Requirement	Status	Comments
THR-TC-100	Verified	All components are under their allowable temperature during the load cases
THR-TC-101	Verified	
THR-TC-102	Verified	
THR-TC-200	Verified	
THR-TC-201	Verified	The allowable temperature of the magnet stack is first reached at 45 W losses
THR-TC-300	Verified	The mass of the EM and all design cases is under 1.55 kg
THR-TC-301	Verified	The volume envelope of the EM and all design cases is under R0.1x0.865 m
THR-TC-400	Not Verified (Yet)	The boron nitride coating is not space-qualified, as it is only used for testing. A qualification campaign should be done, or another coating should be used. If black Kapton is used (as in baseline), the requirement is verified.
THR-TC-401	Not Verified (Yet)	No EOL properties have been simulated yet (important for thermo-optical properties)
THR-TC-500	Not Verified	The heat load introduced by the baseline thruster into the s/c wall through radiation is 8.4 W. The one for the two radiator design case is 4.4 W. Techniques such as a heat shield or covering the thruster with MLI should be investigated.
THR-TC-501	Not Verified	The heat load introduced by the baseline thruster into the s/c wall through conduction is 2.5 W.
THR-TC-502	Verified	None of the design modifications affect the anode/magnet stack/plasma flow
THR-TC-600	Not Verified (Yet)	Mechanical joints should be analysed for the two radiators concept. For the baseline design, this requirement is verified, as the integration has already been performed.
THR-TC-610	Verified	The vacuum chamber used had a pressure in the range of 10^{-6} mbar
THR-TC-611	Verified	
THR-TC-700	Verified	
THR-TC-701	Verified	Systema Thermica is a space-verified software [45]
THR-TC-702	Verified	
THR-TC-710	Verified	
THR-TC-711	Verified	Maximum deviation of 2.85ºC
THR-TC-712	Verified	Mean deviation of 1.65ºC
THR-TC-713	Verified	Standard deviation of 1.96ºC

Bibliography

[1] R. Sandau. Status and trends of small satellite missions for earth observation. *Acta Astronautica*, 66(1):1–12, 2010.

[2] G. Richardson, K. Schmitt, M. Covert, and C. Rogers. Small satellite trends 2009-2013. In *29th Annual AIAA/USU Conference on Small Satellites*, 2015.

[3] R. Sandau, H.P. Roeser, A. Valenzuela, et al. *Small satellite missions for earth observation*. Springer, 2014.

[4] R.A. Deepak and R.J. Twiggs. Thinking out of the box: Space science beyond the cubesat. *Journal of Small Satellites*, 1(1):3–7, 2012.

[5] W.A. Hanson. In their own words: Oneweb's internet constellation as described in their fcc form 312 application. *New Space*, 4(3):153–167, 2016.

[6] A.A. Proshin, E.P. Goryacheva, N.V. Goryachev, and N.K. Yurkov. Cubesat miniature satellites of the planet earth. In *XI International scientific and practical conference,«Scientific horizons»,-Sheffield. Science and education LTD. UK*, volume 11, pages 82–85, 2015.

[7] B. Lal et al. Trends in small satellite technology and role of the nasa small spacecraft technology program. `https://www.nasa.gov/sites/default/files/atoms/files/nac_march2017_blal_ida_sstp_tagged.pdf`, 2017. Accessed: 24-7-2017.

[8] B.J. Kim, S. Park, E.E. Kim, H.S. Chang, W. Park, J. Seon, et al. Macsat-a mini-satellite approach to high resolution space imaging. 2003.

[9] W.J. Larson and J.R. Wertz. *Space Mission Analysis and Design*. Microcosm, 1992.

[10] V. Zakirov and L. Li. Propulsion challenges for small spacecraft: 2005. *Tsinghua Science & Technology*, 11(5):507–514, 2006.

[11] K.I. Parker. State-of-the-art for small satellite propulsion systems. 2016.

[12] J.C. Lyke. Plug-and-play satellites. *IEEE SpEctrum*, 49(8), 2012.

[13] J. Miller, J. Guerrero, D. Goldstein, and T. Robinson. Spaceframe: Modular spacecraft building blocks for plug and play spacecraft. In *Small Satellite Conference, AIAA/USU*, 2002.

[14] J. Lyke, S. Cannon, D. Fronterhouse, D. Lanza, and T. Byers. A plug-and-play system for spacecraft components based on the usb standard. 2005.

[15] T. Kuwahara et al. Satellite system integration based on space plug and play avionics. In *System Integration (SII), 2011 IEEE/SICE International Symposium on*, pages 896–901. IEEE, 2011.

[16] D. Gibbon, M. Paul, and L. Cowie. Cots (commercial off the shelf) propulsion equipment for low cost small spacecraft. In *Proceedings of the 38th Aiaa/Asme/Sae/Asee Joint Propulsion Conference and Exhibit, Indianapolis, IN, Aiaa Paper*, volume 3994, pages 7–10, 2002.

[17] R.G. Jahn. *Physics of Electric Propulsion*. McGraw-Hill, 1968.

[18] G.P. Sutton and O. Biblarz. *Rocket Propulsion Elements*. John Wiley and Sons, 2016.

[19] D.M. Goebel and I. Katz. *Fundamentals of Electric Propulsion: Ion and Hall Thrusters*. Wiley, 2008.

[20] M. Vaupel. Development and test of a first generation mn-microhempt engineering model. Master's thesis, Philipps Universiteit Marburg, Germany, 2017.

[21] A. Keller, P. Köhler, F.G. Hey, M. Berger, C. Braxmaier, D. Feili, D. Weise, and U. Johann. Parametric study of hemp-thruster downscaling to micron thrust levels. *IEEE Transactions on Plasma Science*, 43(1):45–53, 2015.

[22] G. Kornfeld, J. Wegener, and H. Seidel. Plasma accelerator for space vehicles, increasing ion thruster motor efficiency, 1999. URL `https://www.google.com/patents/DE19828704A1?cl=en`. DE Patent App. DE1,998,128,704.

[23] G. Kornfeld, N. Koch, and G. Coustou. The Highly Efficient Multistage Plasma (HEMP) thruster, a new electric propulsion concept derived from tube technology. In *4th IEEE International Vacuum Electronics Conference, IVEC 2003 - Proceedings*, pages 3–4, 2003. ISBN 0780376994. doi: 10.1109/IVEC.2003.1285973.

[24] N. Koch, H. Harmann, and G. Kornfeld. Status of the thales high efficiency multi stage plasma thruster development for hemp-t 3050 and hemp-t 30250. In *Proceedings of the 30th International Electric Propulsion Conference*, pages 17–20, 2007.

[25] F.G. Hey. *Development and Test of a Micro-Newton Thruster Test Facility and Micro-Newton HEMPTs*. PhD thesis, TU Dresden, Germany, 2016.

[26] G. Kornfeld, N. Koch, and H.P. Harmann. Physics and evolution of hemp-thrusters. In *Proceedings of the 30th International Electric Propulsion Conference*, pages 17–20, 2007.

[27] W.A. Hoskins et al. 30 years of electric propulsion flight experience at Aerojet Rocketdyne. In *33rd International Electric Propulsion Conference, Washington, DC*, 2013.

[28] J.E. Polk et al. Demonstration of the NSTAR ion propulsion system on the Deep Space One mission. In *27th International Electric Propulsion Conference, Pasadena, CA*, 2001.

[29] E. Pencil, H. Kamhawi, and L. Arrington. Overview of NASA's Pulsed Plasma Thruster development program. In *40th AIAA/ASME/SAE/ASEE Joint Propulsion Conference and Exhibit, Fort Lauderdale, FL*, 2004.

[30] S. Weis, A. Lazurenko, B. van Reijen, J. Haderspeck, A. Genovese, et al. Overview, Qualification and Delivery Status of the HEMPT based Ion Propulsion System for SmallGEO. *34th International Electric Propulsion Conference*, (299):1–10, 2015.

[31] R. Schneider, K. Matyash, O. Kalentev, F. Taccogna, N. Koch, and M. Schirra. Particle-in-Cell Simulations for Ion Thrusters. *Contributions to Plasma Physics*, 49(9):655–661, 2009. ISSN 08631042. doi: 10.1002/ctpp.200910070.

[32] A. Keller. *Feasibility of a down-scaled HEMP Thruster*. PhD thesis, Justus-Liebig-Universiteit Giessen, Germany, 2013.

[33] K.S. Jefferies. Solar simulator for solar dynamic space power system testing. 1993.

[34] J. Meseguer, I. Pérez-Grande, and A. Sanz-Andrés. *Spacecraft Thermal Control*. Woodhead Publishing, 2012.

[35] R. Ibtiouen et al. Application of lumped parameters and finite element methods to the thermal modeling of an induction motor. In *IEMDC - IEEE International Electric Machines and Drives Conference*, 2001.

[36] B. Shabani and M. Biju. Theoretical modelling methods for thermal management of batteries. *Energies*, 2015.

[37] ECSS-E-HB-31-03A. Thermal Analysis Handbook. Standard, European Cooperation for Space Standardization (ECSS), Noordwijk, The Netherlands, 2016.

[38] J. Kim and N.M. Teti. Thermal testing and model correlation of the magnetospheric multi-scale (mms) observatories. In *45th International Conference on Environmental Systems*, 2015.

[39] S. Kang and H. Oh. On-orbit thermal design and validation of 1 u standardized cubesat of step cube lab. *International Journal of Aerospace Engineering*, 2016, 2016.

[40] J.R. Anderson, J.S. Snyder, J.L. Van Noord, and G.C. Soulas. Thermal development test of the NEXT PM1 ion engine. *43rd AIAA/ASME/SAE/ASEE Joint Propulsion Conference*, 3(July):2093–2115, 2007.

[41] S.R. Parker. Thermal Modeling and Validation Testing of a Miniature Xenon Ion Thruster. Master's thesis, California Polytechnic State University San Luis Obispo, 2013.

[42] J. Bouwmeester and J. Guo. Survey of worldwide pico-and nanosatellite missions, distributions and subsystem technology. *Acta Astronautica*, 67(7):854–862, 2010.

[43] H. Riebeek. Catalog of earth satellite orbits. `https://earthobservatory.nasa.gov/Features/OrbitsCatalog/`, 2009. Accessed: 20-7-2017.

[44] J. Liou and N.L. Johnson. Earth satellite population instability: Underscoring the need for debris mitigation. 2006.

[45] ECSS-E-ST-31C. Thermal Control General Requirements. Standard, European Cooperation for Space Standardization (ECSS), Noordwijk, The Netherlands, 2008.

[46] Eclipse Magnetics. Smco magnets datasheet, n.d. Product Datasheet.

[47] CRP Meccanica. Aluminium 7075 t6, n.d. Product Datasheet.

[48] Hydra. Material datasheets. `http://www.witzenmann.cz/cs/media/Manual_of_metal_bellows_0441e_S_174_199_2_04_10_20_download.pdf`, n.d. Accessed: 20-7-2017.

[49] Corning. Macor, n.d. Product Datasheet.

[50] P. Beiss et al. *Group VIII Advanced Materials and Technologies: Powder Metallurgy Data. Refractory, Hard and Intermetallic Materials*. Springer, 2002.

[51] SGL Group. Sigraflex, n.d. Product Datasheet.

[52] Teadit. Metallic materials, 2008. Product Datasheet.

[53] Engineering Toolbox. Metals - melting temperatures. http://www.engineeringtoolbox.com/melting-temperature-metals-d_860.html, n.d.. Accessed: 20-7-2017.

[54] ECSS-Q-ST-70-71C. Space product assurance: Materials, processes and their selection. Standard, European Cooperation for Space Standardization (ECSS), Noordwijk, The Netherlands, 2014.

[55] ECSS-Q-ST-70-01C. Space product assurance: Cleanliness and contamination control. Standard, European Cooperation for Space Standardization (ECSS), Noordwijk, The Netherlands, 2008.

[56] Engineering Toolbox. Emissivity coefficients of some common materials. http://www.engineeringtoolbox.com/emissivity-coefficients-d_447.html, n.d.. Accessed: 20-7-2017.

[57] D.G. Gilmore, W.K. Stuckey, and M. Fong. Thermal surface finishes. *Spacecraft Thermal Control Handbook*, 1:139–159, 1994.

[58] Solar Mirror. Absorptivity and emissivity table. http://www.solarmirror.com/fom/fom-serve/cache/43.html, n.d. Accessed: 20-7-2017.

[59] T. Misuri et al. Telemicroscopy and thermography diagnostic systems for monitoring hall effect thrusters. In *IEPC - International Electric Propulsion Conference*, 2011.

[60] A. Zunger, A. Katzir, and A. Halperin. Optical properties of hexagonal boron nitride. *Physical Review B*, 13(12):5560, 1976.

[61] L. Kauder. Spacecraft Thermal Control Coatings References. Technical publication, National Aeronautics and Space Administration, US, 2005.

[62] I. Martinez. Thermo-optical properties. http://webserver.dmt.upm.es/~isidoro/dat1/Thermooptical.pdf, n.d. Accessed: 20-7-2017.

[63] J.R. Lowery. Solar absorption characteristics of several coatings and surface finishes. Technical report, National Aeronautics and Space Administration, Huntsville, AL (USA). George C. Marshall Space Flight Center, 1977.

[64] H. Langer, A. Steinbicker, H. Meister, and C. Zauner. Integrated thermal fe analyses and testing of prototype components for the iter bolometer diagnostic. *Fusion Engineering and Design*, 96:821–825, 2015.

[65] K.N. Babu. Thermal contact resistance:experiments and simulation. Master's thesis, Chalmers University of Technology, Sweden, 2015.

[66] A. Hasselstrom and U. Nilsson. Thermal contact conductance in bolted joints. Master's thesis, Chalmers University of Technology, Sweden, 2015.

[67] M.M. Yovanovich. Thermal interface (joint) conductance and resistance. ECE 309, University Lecture, 2000.

[68] Inc. ASM Aerospace Specification Metals. Aluminum 7075-t6. `http://asm.matweb.com/search/SpecificMaterial.asp?bassnum=MA7075T6`, n.d. Accessed: 20-7-2017.

[69] C.P. Kothandaraman. *Heat and mass transfer data book*. New Age International, 2004.

[70] Accuratus. Boron nitride ceramic properties. `http://accuratus.com/boron.html`, n.d. Accessed: 20-7-2017.

[71] Steelss. Data table for carbon steel: St37-3u. `http://www.steelss.com/Carbon-steel/st37-3u.html`, n.d. Accessed: 20-7-2017.

[72] E. Ahedo. Plasmas for space propulsion. *Plasma Physics and Controlled Fusion*, 53(12): 124037, 2011.

[73] QuickOhm Kuepper and Co. GmbH. Datenblatt heatpipe, n.d. Product Datasheet.

[74] Ziehl. Pt100-temperature-sensors type tf101, 2016. Product Datasheet.

[75] H.H. Ku. Notes on the use of propagation of error formulas. *Journal of Research of the National Bureau of Standards*, 70(4), 1966.

[76] G.T. Linteris, R.E. Lyon, and S.I. Stoliarov. Prediction of the gasification rate of thermoplastic polymers in fire-like environments. *Fire safety journal*, 60:14–24, 2013.

[77] A summary of error propagation. Physical Sciences, University Lecture, 2007.

[78] G. Kornfeld, N. Koch, and H. Harmann. New performance and reliability results of the thales hemp thruster. In *4th International Spacecraft Propulsion Conference*, volume 555, 2004.

[79] G. Kornfeld, N. Koch, and G. Coustou. First test results of the hemp thruster concept. In *Proceedings of the 28th International Electric Propulsion Conference*, 2003.

[80] H.W. Loeb. Plasma-based ion beam sources. *Plasma physics and controlled fusion*, 47 (12B):B565, 2005.

[81] N. Teti. La-ii thermal coating validation report. Technical report, National Aeronautics and Space Administration, US, 2002.

[82] E. Brodu and M. Balat-Pichelin. Emissivity of boron nitride and metals for the solar probe plus mission. *Journal of Spacecraft and Rockets*, 53, 2016.